TECHNISCHE UNIVERSITÄT WIEN

CDL SE

Dissertation

New insights on fracture tolerant and superhard hexagonal TMB_2 thin films

carried out for the purpose of obtaining the degree of Doctor technicae (Dr. techn.),
submitted at TU Wien, Faculty of Mechanical and Industrial Engineering,

submitted by

Christoph Fuger

Matr.Nr.: 01246021

[redacted]

under the supervision of

Ass. Prof. Dipl.-Ing. Dr. Helmut Riedl-Tragenreif

Institute of Material Science and Technology, E308-01-2
Applied Surface and Coating Technology

Wien, May 2022

reviewed by

Prof. Dr. Christian Mitterer
Department Werkstoffwissenschaften
Montanuniversität Leoben
A-8700 Leoben, Austria

Prof. Dr. Petr Vašina
Department of Physical Electronics
Masaryk University
Kotlářská 267/2, Veveří, Brno

The financial support by the Austrian Federal Ministry for Digital and Economic Affairs, the National Foundation for Research, Technology and Development and the Christian Doppler Research Association is gratefully acknowledged (Christian Doppler Laboratory "Surface Engineering of high-performance Components"). We also thank for the financial support of Plansee SE, Plansee Composite Materials GmbH, and Oerlikon Balzers, Oerlikon Surface Solutions AG.

Affidavit:

I declare in lieu of oath, that I wrote this thesis and performed the associated research myself, using only literature cited in this volume. If text passages from sources are used literally, they are marked as such. I confirm that this work is original and has not been submitted elsewhere for any examination, nor is it currently under consideration for a thesis elsewhere. I acknowledge that the submitted work will be checked electronically-technically using suitable and state-of-the-art means (plagiarism detection software). On the one hand, this ensures that the submitted work was prepared according to the high-quality standards within the applicable rules to ensure good scientific practice "Code of Conduct" at the TU Wien. On the other hand, a comparison with other student theses avoids violations of my personal copyright.

Date *Signature*

Acknowledgements

... will be included in final printed version.

Contents

List of Figures

Abstract

In the progression of novel protective thin film materials, the attention for transition metal diborides (TMB_2) substantially increased during the last years. The unique strength of their hybridized covalent bonds combined with their hexagonal close-packed (hcp) structures is a big advantage and a limiting factor. The related brittleness, variety of crystal structures, and stoichiometries depict significant challenges for a broad usage of physical vapor deposited TMB_2 coatings in diverse applications. This study focuses on a deeper understanding of elasto-plastic properties, including fracture mechanics and synthesis-structure-property relationships of various binary and ternary TMB_2-based thin films.

The thermodynamic stability of AlB_2 (α) and W_2B_5 type (ω) structured $WB_{2\pm z}$ is investigated by ab-initio density functional theory calculations. While ω-WB_2 reveals the energetic minimum near the stoichiometric composition (hence, a perfectly arranged crystal structure), the α-phase is preferentially stable in the sub-stoichiometric regime stabilized by Boron vacancies. Theoretical calculations prove α-$WB_{1.5}$ as the most energetically (energy of formation) and mechanically (C_{44}) stable stoichiometry. Nanoindentation experiments revealed a pronounced anisotropy for super-hard 0001 WB_{2-z} textured films. Increasing $10\bar{1}1$ orientation fraction significantly reduces the film hardness, attributed to easier to activate basal slip planes. Still, no texture-related fracture behavior is observed by micro-cantilever bending.

Interestingly, the addition of Ta, forming α-$W_{1-x}Ta_xB_{2-z}$ with x = 0, 0.07, 0.14, 0.26, 0.43, 0.70, and 1, maintains a single-phase structure up to x = 0.26 Ta on the metal sublattice. Solid solution and grain refinement strengthening are the main effects of increasing hardness from 40.8 ± 1.5 GPa to 45.0 ± 2.0 GPa. In contrast, the intrinsic fracture toughness (K_{IC}) generally decreases with rising Ta but reveals a maximum of $K_{IC} = 3.8 \pm 0.5$ MPa$\sqrt{m}$ for α-$W_{0.93}Ta_{0.07}B_{1.76}$, being in good correlation to theoretical predictions. In addition to the enhanced mechanical properties, low amounts of Ta also improve the oxidation resistance. The scale thickness decreases from 8.0 μm for pure WB_{2-z} to 1.6 μm for TaB_{2-z} after oxidizing in ambient air at 600°C for 1000 min. Moreover, the growth mode changes from a paralinear for W-rich to a linear – but retarded – mode for Ta-rich films. Hence, an optimum composition for α-$W_{1-x}Ta_xB_{2-z}$ coatings in the range of x = 0.2 to 0.3, combining fracture resistance,

super-hardness, and decelerated oxidation kinetics owing to the formation of denser scales.

The second part of the thesis investigates the sputter growth conditions (DC-mode) and related elasto-plastic properties of TiB_{2+z} based thin films. The focus is on the influence of structural mannerisms – such as the anisotropic behavior of hexagonal crystals or the formation of nano-columnar tissue phases – on the mechanical properties of TiB_{2+z}. By systematically varying the target-substrate distance and the deposition pressure, a broad compositional variation from nearly stoichiometric α-$TiB_{2.07}$ up to super-stoichiometric α-$TiB_{4.42}$ is achieved. A significant deviation in the angular distribution of sputtered B and Ti species is evident, where B atoms are preferentially emitted along the target normal. Thorough structure-mechanical analysis revealed a deposition pressure related to 0001 film texture, which is essential to achieve super-hardness. Higher pressure (> 1.2 Pa) arising $10\bar{1}1$ and 1000 orientations contribute to a hardness drop of more than 10 GPa. A similar slope of H with varying 0001 fraction is observed for WB_{2-z}, suggesting a relation in anisotropic behavior for hexagonal structured TMB_2 films. HR-TEM analysis gains insights into the formation of the B-rich tissue phases and the related morphology, based on the broad stoichiometric variation. B to Ti ratios above 2.5 force the formation of smaller nano-columns (i.e., decreased column size from 10 to 2 nm) to distribute excess B on the surplus of tissue phase fraction. Consequently, this reduces fracture toughness from about 3.0 to 2.5 MPa$\sqrt{m}$, related to the increased B-rich tissue phase fraction, providing the weakest pathways for crack propagation. The small nano-columns also promote grain boundary sliding events leading to a declining hardness of about 5 GPa for 0001 textured TiB_{2+z} films.

Chapter 1

Introduction

Many industrial sectors like aviation, transportation, and energy production aim for longer lifetimes of their deployed high-precision components (turbines, turbine blades, gears, etc.). Especially in saving resources, sustainability, and thus, a responsible environmental interaction, longer component lifetimes are essential. Protecting blades or drive train systems in jet engines or steam turbines [1] requires the applied coating materials to withstand harsh, abrasive and corrosive environments. Consequently, protective thin film development aims for significant mechanical material properties [2], beneficial for elevated erosion resistance [3, 4], as well as the investigation of new material systems with pronounced thermal stability and high-temperature oxidation resistance [5].

The presently dominating industrially applied protective coating materials are compounds, predominantly based on nitrides, carbides, and oxides. Transition metal ceramics, particularly transition metal nitrides such as TiN and CrN have been explored in-depth over decades [6, 7]. By forming NaCl-prototype structured ternary CrAlN and TiAlN, the Al alloying strategy improves the binary material system's limited thermo-mechanical properties and oxidation resistance [8]. Spinodal decomposition at around 1000°C constitutes the separation of supersaturated, metastable c-TiAlN into TiN- and AlN-rich domains, promoting precipitation strengthening effects [9]. Moreover, Si alloying is beneficial for enhanced oxidation behavior of TiN based material systems (e.g. TiSiN) [10], obtaining limited yet mostly sufficient oxidation resistance up to 1000°C. The characteristics mentioned above, combined with the possibility for synthetization by industrially preferred deposition techniques (e.g., arc evaporation), facilitate the popularity of transition metal nitride-based ceramic thin films.

Nevertheless, new alternatives to state-of-the-art applied thin film solutions with improved material properties are still highly desired. One of these novel material classes are transition metal diborides (TMB_2) [11]. With superior mechanical properties, enhanced wear resistance, and electrical conductivity to even super-conductivity, the material system offers attractive characteristics for prospective coating applications [12–16].

The development of bulk transition metal borides goes back to the early 19th century, when Moissan investigated the reaction of Cr and B using an electric furnace [17]. His work was extended by Tucker and Moody using Zr, Cr, W, and Mo, concluding to have found crystalline and hard reaction products [18]. Years later (1936), Hoffmann and Jäniche firstly addressed the AlB_2 structure type (α) underlined by the investigations of AlB_2 type TiB_2 and ZrB_2 of Ehrlich and Kiessling [19, 20]. In 1950 the TM_2B_5 type structure (ω) was developed for MoB_2 and WB_2 [21].
The competition of the α- and ω-structure in terms of thermodynamic stability was investigated by Moraes et al. using ab-initio density functional theory calculations [22]. They observed the strong preference of early TMB_2 (group 4-5) to crystalize in the α-phase, whereas late TMB_2 (group 6 and above) prefer forming the ω-structure. Nevertheless, the calculations revealed the possibility of stabilizing the group 6 WB_2 material system in its AlB_2 structure by introducing vacancies to the crystal lattice. In Publication I, the calculations are extended to find the optimum stoichiometry of thermodynamically stable α-WB_{2-z}, correlating with experimental results. In addition to defected structures, alloying elements can decrease the formation energy, stabilizing AlB_2 structured WB_2 (evinced for Ta alloying [23]). Still, by applying semi-empirical ductility criterions (Cauchy pressure, Pugh criterion, Frantsevic criterion) Ta alloying was predicted to deteriorate the ductility of the α-WB_2 structure. This theoretical prediction was experimentally verified within Publication II by DC magnetron sputter deposition of α-$W_{1-x}Ta_xB_{2-z}$ films and further extended by Publication III (high temperature properties).

In the 1980s, the upcoming PVD techniques and improvements of the target materials enabled the development of sputter deposited TMB_2. During the last three decades, various authors focused their investigations on the TiB_2 material system due to its favorable characteristics, including the low density of 4.5 g/cm^3, the high melting temperature of 3225°C, the low electrical resistivity of 7 $\mu\Omega$cm, and especially the very high hardness ($>$ 40 GPa) [12, 24–27]. Since the early 2000s, the formation of a B-rich tissue phase on the grain boundaries is supposed to facilitate the enhanced hardness of TiB_{2+z} thin films [13]. Moreover, the preferred super-stoichiometry of TiB_{2+z} films is related to the different angular distribution of B and Ti atoms during sputtering [28, 29]. Here, Publication IV is assessed to re-investigate the origins of the significant elasto-plastic material properties of TiB_{2+z} applying the deposition pathway proposed by Neidhardt et al. [28].

Unfortunately, high hardness often correlates with low toughness and a pronounced brittle behavior constituting a major limiting factor of transition metal ceramic thin films. The lack of metallic bonding character, forming predominantly ionic and strong directional covalently bonded structures, and the distinct fine-columnar morphology contribute to the enhanced brittleness [30]. The ductile or brittle behavior is often assessed via determining the material's resistance to crack propagation, projected by the fracture toughness (K_{IC}). Recent advances

in micro-cantilever bending make an accurate evaluation of K_{IC} possible, precluding potential sources of error (e.g., residual stresses) [31–33]. In Publication I, II, IV, and V, this approach helped assess the brittle/ductile character of binary WB_{2-z}, TiB_{2+z}, and ternary $W_{1-x}Ta_xB_{2-z}$ coating materials, reaching for an enhanced understanding of prevalent crack mechanisms.

In summary, this study aims for a better understanding of magnetron sputtered, and arc evaporated TMB_2 coatings by investigating structure and morphology related phenomena and elasto-plastic material properties of various TMB_2 thin films.

Chapter 2

Fundamentals and Mechanical Properties

2.1 Deformation of cristalline materials

In order to deform a solid body, an external force has to be applied, which consequently leads to deformation. If the applied force does not exceed a certain threshold value, elastic deformation takes place, which is entirely reversible to its initial state once the force is removed. Plastic deformation occurs when a distinct threshold has been exceeded until exclusively elastic deformation took place. In ductile materials (e.g. steel, metals) the elastic limit or yield strength σ_y indicates the transition between elastic and plastic material behavior.

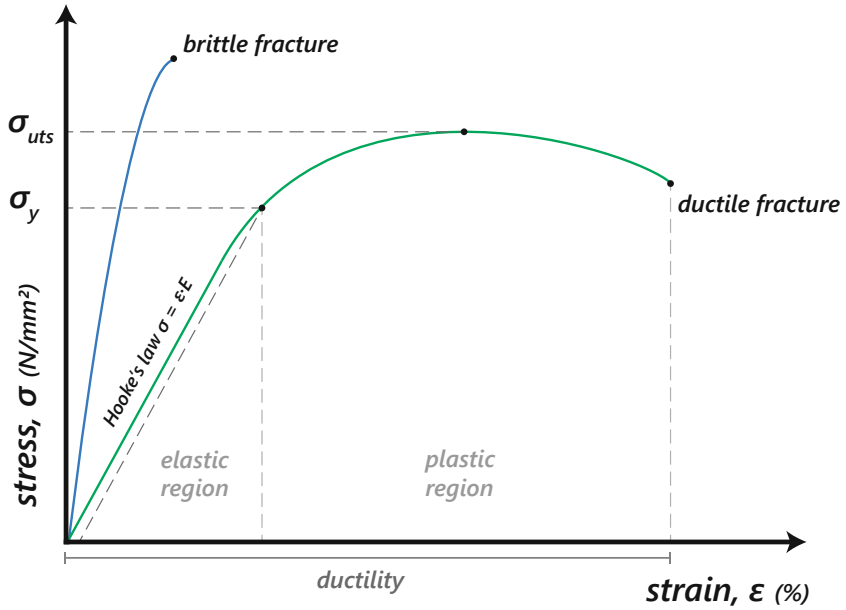

Fig. 2.1: Typical stress-strain curves, obtaining brittle (blue) and ductile (green) material behavior.

Since it is challenging to determine the transition point precisely, σ_y is defined as the stress at 0.2% parallel offset to the linear elastic line. Plastic deformation is irreversible and leads to failure/fracture of the material if the force is further increased. A typical experimental attempt to investigate the deformation behavior of solids is the tensile test, leading to the well-established stress-strain diagram depicted in Figure 2.1.

2.1.1 Elasticity

On a microscopic length scale, elasticity is caused by inter-atomic bonding, often illustrated by springs holding the atoms together. When a force is applied, the atoms move from their equilibrium position. Consequently, the applied force increases proportionally to the rising inter-atomic distance. The second derivative of the binding potential energy well (see Figure 2.2), which represents the atomic bond strength, leads to the elastic modulus:

$$E = \frac{1}{r_0}\frac{\partial^2 U}{\partial r^2} \tag{2.1}$$

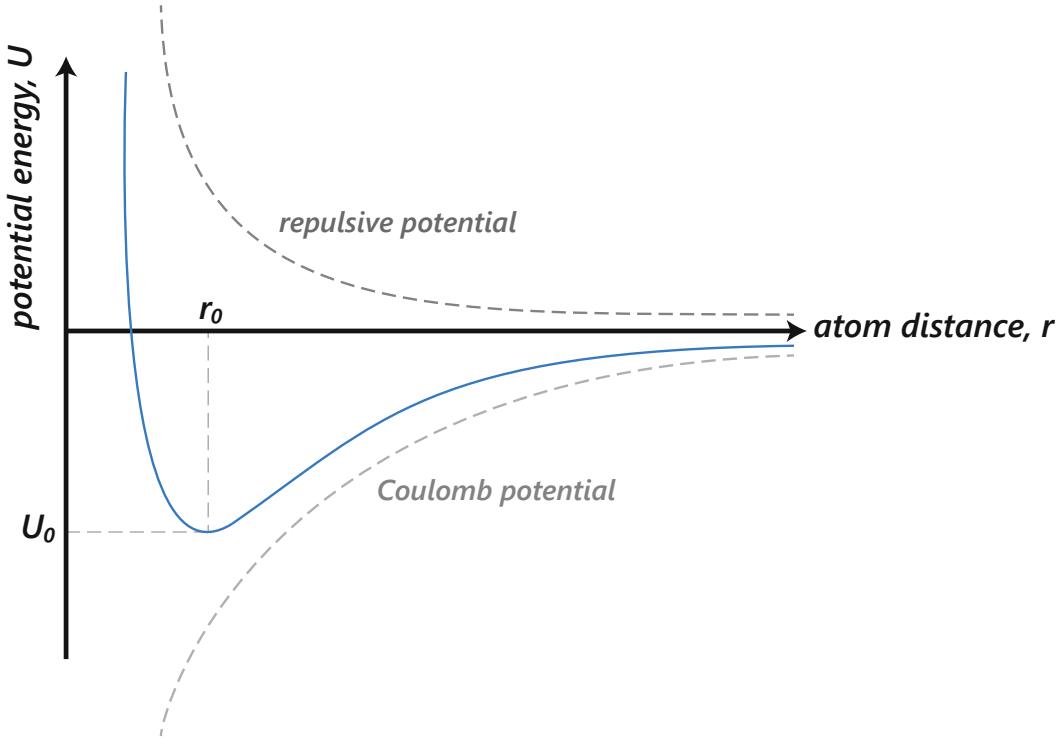

Fig. 2.2: Binding potential well (blue curve), composed of repulsive and attractive Coulomb potential.

However, considering the example of springs connecting the atoms, the representation of the elastic behavior is evident by Hook's law, which is defined for vertically (tension, compression) and parallel (shear) applied forces as follows:

$$\frac{F_{\perp}}{A} = E \cdot \frac{\Delta l}{l_0}, \sigma = E \cdot \epsilon \tag{2.2}$$

$$\frac{F_{\parallel}}{A} = G \cdot \frac{\Delta x}{d}, \tau = G \cdot \gamma \tag{2.3}$$

Here, the constants of proportionality for tensile and shear stresses are the elastic modulus E and the shear modulus G, respectively. Together with the bulk modulus B defined for compressive stresses, the three parameters (E, G, B) symbolize the elastic resistance against deformation. In addition to E, G, and B, Poisson's ratio ν is defined as the negative ratio of transverse strain to axial strain. In three dimensions, the considerations mentioned above become more complex. Hook's law of linear elasticity for the most general anisotropic solid is then expressed as:

$$\sigma_{ij} = C_{ijkl} \cdot \epsilon_{kl} \tag{2.4}$$

with second rank stress tensor σ_{ij}, second rank strain tensor ϵ_{kl}, and fourth rank stiffness tensor C_{ijkl} with $34 = 81$ elements.

Due to symmetrical deliberations, C_{ijkl} is simplified to a 6 x 6 matrix C_{ij} with 36 elements describing all the elastic constants. In hexagonal crystals, C_{ijkl} further simplifies to the following stiffness matrix:

$$C_{ij} = \begin{pmatrix} C_{11} & C_{12} & C_{13} & 0 & 0 & 0 \\ 0 & C_{11} & C_{13} & 0 & 0 & 0 \\ 0 & 0 & C_{33} & 0 & 0 & 0 \\ 0 & 0 & 0 & C_{44} & 0 & 0 \\ 0 & 0 & 0 & 0 & C_{44} & 0 \\ 0 & 0 & 0 & 0 & 0 & C_{66} \end{pmatrix} \tag{2.5}$$

with $C_{66} = \frac{C_{11}-C_{12}}{2}$ leading to only five independent elastic constants [34].

2.1.2 Plasticity

Irreversible deformation of a crystalline material is achieved by shifting crystal areas along crystallographic planes. Hereby, the crystal areas are moved by an integral multiple of the interatomic distance within this plane, simultaneously preserving the crystal structure. Hence, a critical shear stress must be overcome, which is defined as follows:

$$\tau_{max} = \frac{G}{2\pi}\frac{a}{d} \tag{2.6}$$

with atomic distance a and planar spacing d.

The approach for τ_{max} simplifies to the theoretical shear strength τ_{th}:

$$\tau_{th} \approx \frac{G}{10} \approx \frac{E}{25} \tag{2.7}$$

By comparing the theoretical shear strength and experimental determined critical shear stresses, a conspicuous deviation up to 10^4 Nm^{-2} is noticeable. As an example, Al shows a τ_{th} of $0.2 \cdot 10^9$ Nm^{-2} but τ_{exp} of only $0.79 \cdot 10^6$ Nm^{-2}. The investigated discrepancy is explained by dislocation movement, which enables a small stepwise gliding of lattice planes leading to a tremendous reduction of the necessary shear stress.

In general, a maximum in active shear stress is active at an angle of 45° with resprect to the normal stress loading direction, described by Schmid's law:

$$\tau = \sigma \cdot \cos\lambda \cdot \cos\phi \tag{2.8}$$

with angle between loading direction and slip direction λ, and angle between loading direction and slip plane normal ϕ.

2.1.3 Dislocations and twinning

Edge and screw are the two main types of dislocations with Burgers-vector $\vec{b}$ perpendicular to the dislocation line and $\vec{b}$ parallel to the dislocation line, respectively. The movement is always perpendicular to the dislocation line, and it is rarely the case that dislocations are pure edge or screw dislocations. A combination of both extremes is observed in experiments.

Dislocations prefer gliding on densest packed crystal planes, where a minimum in Peierls-stress is required for the movement:

$$\tau_p = \frac{2G}{k} e^{-\frac{2\pi}{k}\frac{d}{b}} \tag{2.9}$$

with k = 1 for screw dislocations and k = 1-ν for edge dislocations.

In face-centered cubic (fcc) crystals, four equivalent {111} planes are the closest packed ones and, therefore, preferred for dislocation gliding. With three different ⟨110⟩ glide-directions on four {111} planes, respectively, the fcc crystal provides 12 independent glide-systems. For comparison, hexagonal (hex) crystals exhibit only three independent glide systems, with the closest packed 0001 glide planes and three $\langle 11\bar{2}0 \rangle$ glide-directions. However, for c/a $<$ 1.63, prismatic and pyramidal slip are also observed.

In addition to dislocation movement, which is the most important and most frequent mechanism for plastic deformation in crystals, also mechanical twinning contributes to the irreversible deformation of materials. Twinning preferentially occurs at low temperatures and high deformation rates and is characterized by a 180° rotation around the twin plane of twin and remaining matrix. The mirror plane (twin plane) is the coherent twin boundary. To deform a polycrystalline material at least five independent glide systems are required. Therefore, twinning is essential to ensure plastic deformation in hexagonal materials with c/a $>$ 1.63, where only three independent glide systems are present.

2.1.4 Fracture

In ductile materials, necking and pore formation starts when the stresses exceed the ultimate tensile strength σ_{uts}, which leads to ductile fracture of the material during tensile testing. In contrast, no necking takes place in brittle materials. Here, the fracture behavior is dominated by crack initiation (breaking of bonds) and propagation due to exceeding a critical stress σ_{crit}. The propagation of cracks in materials is described by fracture mechanics, calculating the driving forces on a crack tip and characterizing the material's resistance to fracture. One fundamental relation was found by A. A. Griffith, who discovered that the product of the square root of crack length a and the fracture stress σ_f is constant. Moreover, he defined the energy release rate term G, which mainly depends on the surface energy γ required to grow a crack. Irwin et al. extended G by a dissipative term. He found that a plastic zone forms at the crack tip in ductile materials, which leads to energy dissipation as heat.

These considerations lead to the well-known Griffith criterion:

$$\sigma_f \sqrt{a} = \sqrt{\frac{EG}{\pi}} \tag{2.10}$$

with energy release rate G.

Furthermore, Irwin introduced the stress intensity factor K_I, which then replaced the energy release rate term as follows:

$$K_I = Y\sigma\sqrt{\pi a} \tag{2.11}$$

with geometric shape factor $Y(\frac{a}{w})$, dependent on crack length a, and width w.

Fracture occurs if $K_I > K_C$ (critical stress intensity factor). For tensile crack loading mode I (opening mode) the critical stress intensity factor is indicated as K_{IC} and widely used for characterizing the material's fracture toughness.

It is also worth mentioning the expression for the idealized radius of the plastic zone at the crack tip:

$$r_p = \frac{K_c^2}{2\pi\sigma_y^2} \tag{2.12}$$

2.2 Elasto-plastic response and fracture of thin films

A common and relatively easily accessible parameter representing the strength of thin films is the hardness value H, typically obtained by surface indentations. Experiments revealed that the mean contact pressure p_m, at which there is no increase with increasing indenter load, is related to H. Moreover, it shows that p_m is directly proportional to the materials yield strength σ_y. Due to indentation stress field related causes, p_m, required for initiating yield is always more significant than the stress required at uniaxial compression. A frequently used relation is set up by Tabor [35]:

$$H_v = 3\sigma_y \tag{2.13}$$

Zhang et al. [36] replaced the yield strength σ_y with the ultimate tensile strength σ_{uts} of a material. They concluded that the relation is only valid for materials with low work-hardening ability and low tendency to normal cracking. Their assumptions are based on evaluating three main types of indentation morphologies: "sink-in", "pile-up" and "crack". Due to decreased shear ability and increased fracture strength, brittle materials typically reveal $H_V/\sigma_{uts} >> 3$ [36].

2.2.1 Contact mechanics

The theory of elasticity, describing the interactions of elastic solids, is building the fundament for understanding indentation experiments. One very essential relation is set up by Hertz [37]:

$$a^3 = \frac{3}{4}\frac{PR}{E^*} \tag{2.14}$$

This relation explains the elastic interaction of a rigid indenter with radius R and a flat specimen with modulus E. He found that the circle of contact a is related to the indenter load P and the elastic properties of the contacting materials, leading to the quantification of E* by Timoshenko [38]:

$$\frac{1}{E^*} = \frac{1-\nu^2}{E} + \frac{1-\nu'^2}{E'} \tag{2.15}$$

Therefore, E* represents the "combined" or "reduced" modulus of the materials modulus E with Poisson's ratio ν and the indenter modulus E' with Poisson's ratio ν'. For conical indenters E* is found to be:

$$E^* = \frac{1}{2}\frac{\sqrt{\pi}}{\sqrt{A}}\frac{dP}{dh} \tag{2.16}$$

The quantity dP/dh is referred to as contact stiffness S and defined as the derivative of the applied force with respect to the indentation depth. It is shown that Equation 2.16 can be applied to any axis-symmetric indenter. In nanoindentation tests, the contact stiffness is derived at the beginning of the unloading curve.

2.2.2 Nanoindentation

Typical geometries for nanoindentation experiments are either spherical, conical or pyramidal (Vickers, Berkovich). Due to the higher manufacturing precision of the three-sided pyramid compared to the four-sided Vickers geometry, the Berkovich indenter is preferentially used in small-scale indentation experiments (depicted in Figure 2.3). Hence, this tip geometry is also applied in the current study for determining the mechanical properties of our synthesized thin films. Nevertheless, the projected area A_p to depth ratio equals Vickers indenter [39].

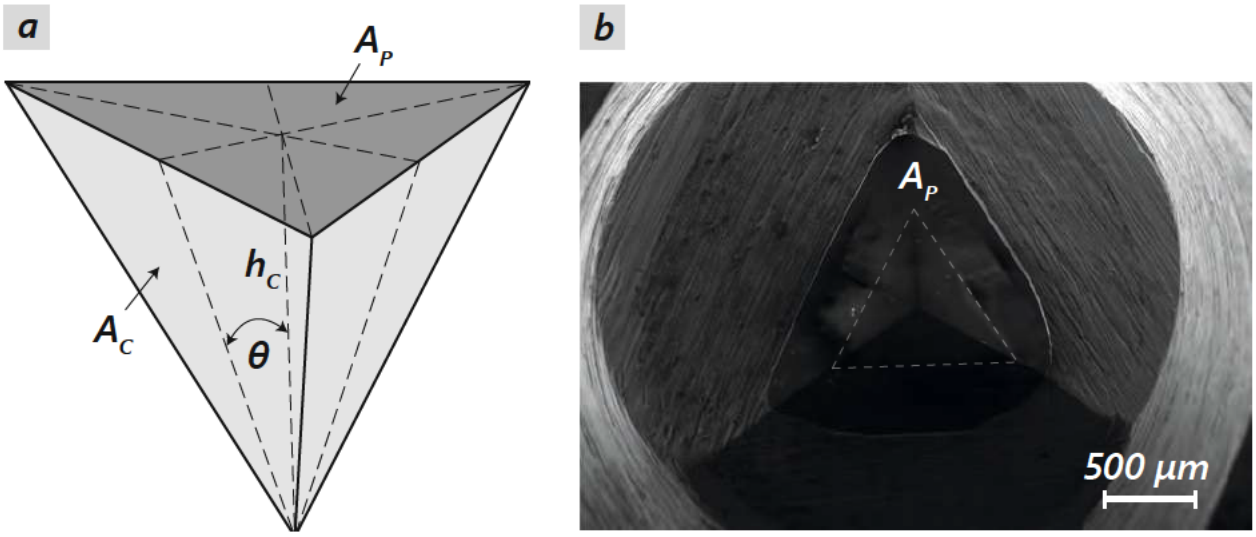

Fig. 2.3: Illustration of a three-sided Berkovich indenter geometry with projected area A_p, contact area A_c, contact depth h_c, and face angle Θ (a). A top view SEM of a Berkovich tip is depicted in b.

The contact area of a Berkovich contact is given by:

$$A_c = 3\sqrt{3}h_c^2 \tan^2 \Theta \tag{2.17}$$

For a face angle of $\Theta = 65.27°$ Equation 2.17 evaluates to:

$$A_c = 24.5h_c^2 \tag{2.18}$$

where h_c is the contact depth.

The result of an indentation experiment is a load-displacement curve , which is separated into two parts: loading and unloading (Figure 2.4). The loading portion shows the elasto-plastic behavior of the material, whereas exclusively the elastic behavior is reflected by the unloading part. H is determined as the ratio of penetration force and residual contact area and, hence, defined as the resistance to penetration or plastic/permanent deformation.

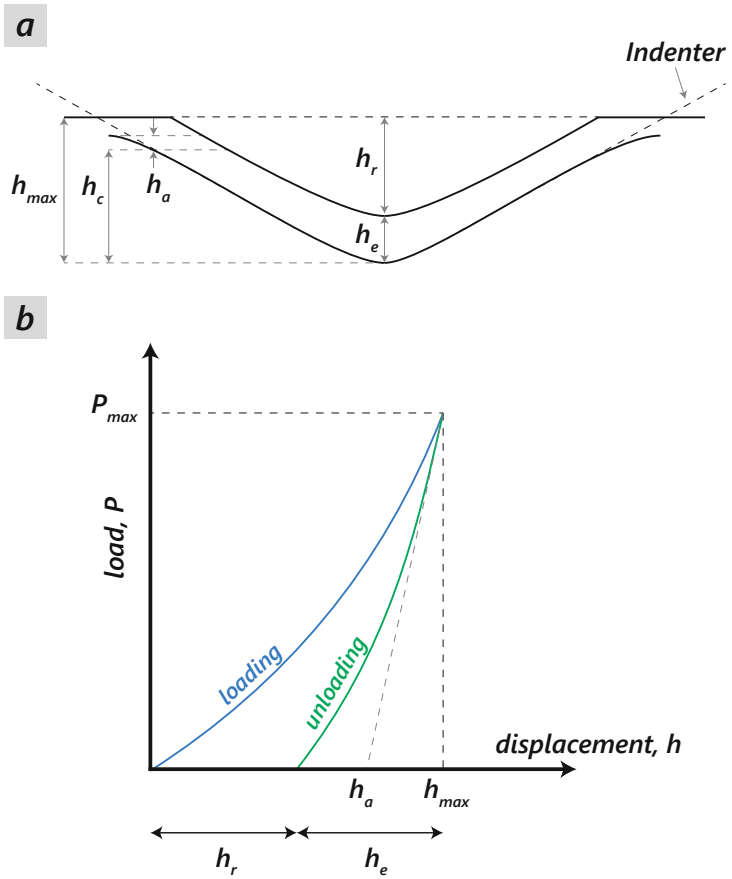

Fig. 2.4: Schematic of a residual indent (a) and the resulting load-displacement curve (b).

The maximum load is used for evaluating the mean contact pressure or materials hardness as follows (for a Berkovich indenter):

$$H = \frac{P_{max}}{24.5 h_c^2} \tag{2.19}$$

Based on Oliver, Pharr, and Sneddon [40, 41] h_c is determined from the unloading part of a load-displacement curve (Figure 2.4). The intersection of the slope of the unloading part at P_{max} gives h_a, needed for calculating h_c as follows [42]:

$$h_c = h_{max} - \epsilon(h_{max} - h_a) \tag{2.20}$$

With geometrical correction factor $\epsilon = 0.75$ for a Berkovich indenter shape.

Consequently, E* is calculated by Equation 2.16 and E of the penetrated film by rearranging Equation 2.15. Typical elastic properties of a Berkovich diamond tip are E' = 1050 GPa and ν' = 0.07. Nowadays, ν of the measured material is often taken from theoretical calculations, where its possible to extract elastic properties (e.g. DFT). Additional to the mechanical properties, the load-displacement curves provide the elastic and plastic energy given by the area beneath the curve. A standard for instrumented indentation tests is provided in DIN EN ISO 14577-1 [43].

There are several factors affecting nanoindentation test data, discussed in the following paragraphs.

Penetration depth It has to be noted that the penetration depth, when measuring a thin film, should not exceed 10% of the coating thickness. Otherwise, the results tend to be influenced by the underneath substrate material. This rule is in general valid for hard coatings on soft substrate materials. Since there is always an elastic displacement of the substrate during indentation, one typical approach to access the purely elastic modulus of the thin film, is the extrapolation by the best fitting mathematic function to the ordinate of the E vs. h_c plot. To evaluate accurate H values, a fully developed plastic zone is required within the film material. Therefore, certain load or penetration depth is necessary, leading to an increase in H for low h_c (visible for sharp tips). After reaching a plateau representing the actual hardness value, a decrease or increase – dependent on the substrate hardness – should be visible.

Thermal drift In the current study's test setting, thin films deposited on various substrate materials are fixed on a steel substrate holder by a thin resin layer. To liquefy the resin, the sample holder is heated to a temperature > 100°C, leading to the measured sample's temperature and volume increase due to the thermal expansion. Hence, the thermal drift deriving

from the cooling film's contraction would affect the measurement's precision. Therefore, a constant temperature of tip and thin film is essential.

Initial penetration At the beginning of an indentation test the indenter tip makes contact with the thin film, creating an initial penetration on the surface before increasing the indenter force for recording the load-displacement curve. This minimal initial penetration depth h_i is described by:

$$h_i = kP_i^m \tag{2.21}$$

with the initial contact load P_i. k and m are dependent on the shape of the indenter and can be determined by:

$$\log h = \log k + A \log(P^m - P_i^m) \tag{2.22}$$

The slope of this linear function should be A = 1 if k and m are chosen correctly. All the obtained load-displacement curves are corrected with h_i.

Instrument compliance The contribution from the instrument compliance C_f includes the displacement of the loading frame, the indenter shaft, and the specimen mount. The compliance of the indenter material is given by 1/S and is included in the "combined" modulus E*. Hence, the total compliance is given by:

$$\frac{dh}{dP} = \frac{1}{S} + C_f \tag{2.23}$$

Consequently, it has the magnitude of displacement per indenter load (nm/mN). It is regularly determined during area function analysis.

Area function correction As it is impossible to fabricate a perfectly sharp indenter tip geometry, an area correction has to be applied considering the tip rounding. Typical tip radii for Berkovich indenter range from 50 - 200 nm, increasing with usage. The area function is determined by measuring a reference material with known E and H in various force ranges. In the current study, a fused silica sample with E = 72.5 GPa and H $\approx$ 10 GPa is measured in a force range from 0.1 mN to 500 mN. The ratio of the actual area of contact A and the ideal area of contact A_i is plotted as a function of the contact depth h_C (see Figure 2.5).

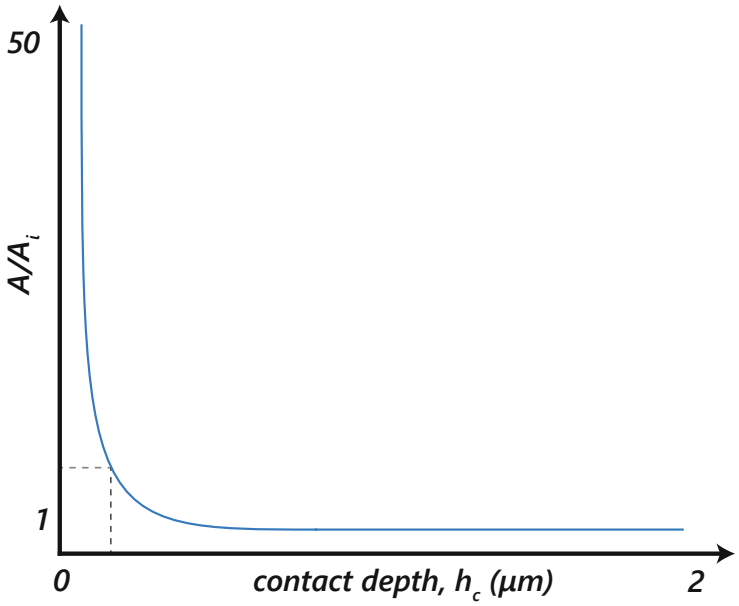

Fig. 2.5: Typical shape of an area correction function.

A is found from rearranging Equation 2.16 and A_i for a Berkovich tip is given by Equation 2.18. The A/A_i ratio for a distinct h_c is applied to H and E as follows:

$$H = \frac{P}{A}\frac{A_i}{A} \tag{2.24}$$

$$E^* = \frac{1}{2}\frac{\sqrt{\pi}}{\sqrt{A}}\frac{dP}{dh}\sqrt{\frac{A_i}{A}} \tag{2.25}$$

where $\beta = 1.034$ (in the current study) is a geometric correction factor.

The area function can also be expressed as the following polynomial function:

$$A = C_1 h_c^2 + C_2 h_c + C_3 h_c^{1/2} + C_4 h^{1/4} c + ... \tag{2.26}$$

By using particular tip geometries (e.g. cube corner), indentation experiments also allow evaluating the material's fracture toughness K_C. Radial cracks which occur during indentation at high force ranges are required for the calculations. A widely used approach is given by Lawn and Anstis [43, 44]:

$$K_C = \alpha\sqrt{\frac{E}{H}}\frac{P}{c^{3/2}} \tag{2.27}$$

where α is an indenter geometry based constant, and c the crack length measured from the center of the indent.

2.2.3 Cantilever bending

However, the intrinsic fracture toughness of a thin film, excluding potential sources of error, like the substrate influence and residual film stresses, is determined by micromechanical cantilever bending tests. The micro-cantilever deflection method was introduced by Di Maio and Roberts [45] and requires the fabrication of microscopic cantilevers by focused ion beam milling (FIB). A spherical diamond tip then penetrates the pre-notched cantilever until fracture. A SEM image of a fabricated cantilever is provided in Figure 2.6. The maximum force recorded by load-displacement data and geometry-based parameters of the cantilever is used for evaluating K_{IC}:

$$K_{IC} = \frac{F_{max} l}{b w^{3/2}} f(\frac{a}{w}) \tag{2.28}$$

where F_{max} is the maximum applied load, l the distance between notch and position of loading, b the cantilever's width, w the thickness of the cantilever and the shape factor f, which is dependent on the depth of the pre-notch a and w.

Linear-elastic bending theory provides the bending stress:

$$\sigma = 6(\frac{Fl}{bw^2}) \tag{2.29}$$

which leads to the fracture stress σ_F when inserting the maximum load at fracture. Consequently, combining σ_F with Equation 2.11 leads to Equation 2.28.

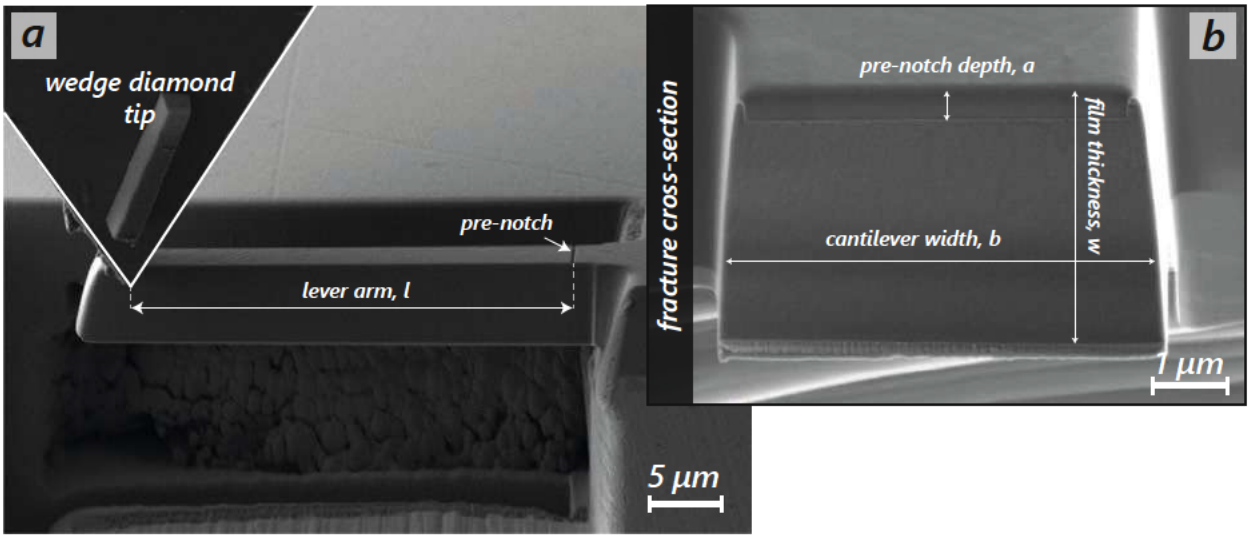

Fig. 2.6: Micrograph of an in-situ SEM cantilever bending experiment (a). A fracture cross section is depicted in b, extracting most relevant dimensions.

A well-established estimation of the shape factor f is provided by Matoy et al. [31] for micro-cantilevers by FEM simulations:

$$f(\frac{a}{w}) = 1.46 + 24.36(\frac{a}{w}) + 47.21(\frac{a}{w})^2 + 75.18(\frac{a}{w})^2 \tag{2.30}$$

Influences of the pre-crack geometry [33] and the material's anisotropy [32] on the micro-cantilever fracture toughness are carefully discussed in the literature. Moreover, an optimum length-to-height ratio l/h $\geq$ 4 is suggested to achieve accurate K_{IC} values with the approach from Matoy.

There are various other micro-scale mechanical testing methods including the tension test, axisymmetric bend test, bulge test, M test and wafer curvature test, to name just a view. An interesting overview also employing mechanical properties that can be measured is given in [46].

2.2.4 Alternative mechanical descriptors

For determining the performance of a coating, one widely established parameter is the H/E ratio representing the "elastic strain to failure". It provides a quantity for a materials ability to deform elastically before irreversible plastic deformation occurs. Especially in tribology, the H/E ratio is vital in classifying the material's wear properties [47]. Leyland and Matthews pointed out that the H/E ratio is more representative of indicating the wear resistance than the individual H and E parameters [48].

In addition, the H^3/E^2 ratio, which indicates the coating's "resistance to plastic deformation" is often used in literature. The parameter derives from the yield pressure P_y defined for a rigid ball on elastic/plastic plate contact [49]:

$$P_y = 0.78r^2\frac{H^3}{E^2} \tag{2.31}$$

with contacting ball radius r.

Hassani et al. showed a correlation of the particle erosion rate on the H^3/E^2 parameter using finite elements modeling [50]. Moreover, experimental observations underlined a coincidence of H^3/E^2 with the erosion resistance of nitride-based coating materials [51].

2.2.5 Intrinsic and extrinsic strenghening

As already mentioned above, the elastic modulus of a material is represented by its interatomic bond strength. How strong atoms are connected depends on the prevalent chemical bondings, which are divided into three main types:

- ionic
- covalent
- metallic

In most materials, a combination of the three types is present, giving them their individual physical properties. An ionic bonding forms if the difference in electronegativity of the adjacent atoms is high. Therefore, the electrons of less electronegative atom are attracted by the higher electronegative one to obtain a more stable electronic configuration.
A covalent bonding is present if atoms share the same valance electrons, forming electron pairs. This bonding type has a strong directionality, giving the material pronounced mechanical strength (e.g. Diamond, c-BN).
Metallic bonding is characterized by delocalized valance electrons, forming an electronic band structure. Due to the non-local character with no directionality, this bonding type represents a lower macroscopic stiffness and a pronounced ductile behavior compared to the covalent bonding.
In addition to the elastic contribution to the film's mechanical strength, the hardness is substantially influenced by dislocation motion through the crystal lattice. Therefore, it is evident that obstacles hindering dislocation motion conduce to an increase in coating hardness. Thin films synthesized by physical vapor deposition techniques usually exhibit a significant fraction of defects (e.g. vacancies, dislocations) arising from high cooling rates from vapor to solid state condensation. Hence, PVD coatings often obtain increased hardness compared to bulk materials.

Solid solution strenghening This strengthening mechanism is based on alloying of additional elements to an existing matrix or lattice and incorporating residual elements (e.g. O, C) from the deposition process. The solute atoms are either included as interstitial or substitutional, creating tensile stresses when smaller and compressive stresses when larger than atoms of the existing lattice. The originated strain field act as an obstacle for moving dislocations, increasing the material's strength, described by the Fleischer relation:

$$\tau = \tau_0 + const \cdot G\sqrt{c} \tag{2.32}$$

with the Peierls-barrier τ_0, shear modulus G and the concentration of the solute atoms c.

Grain boundary/Hall-Petch strengthening Grain –, column- or phase-boundaries act as a barrier to dislocation movement. Neighboring grains often have different orientations. Hence glide planes are not passing through the grain boundary. The critical shear stress has to be overcome for the respective grain to initiate dislocation movement, leading to a pile-up of dislocations on the boundary. As a consequence, smaller grain sizes (higher grain boundary fraction [52]) result in increased strength of the material (Figure 2.7), described by the Hall-Petch relation:

$$\tau = \tau_0 + const \cdot \frac{1}{\sqrt{d}} \tag{2.33}$$

with grain size d.

After reaching a critical grain size d_c, which is in the range of tens of nanometers, a decrease in strength/hardness develops due to the gliding of grain boundaries (reverse/inverse Hall-Petch effect [53]). This critical grain size is dependent on the bonding strength and the cohesive energy of the grain boundaries.

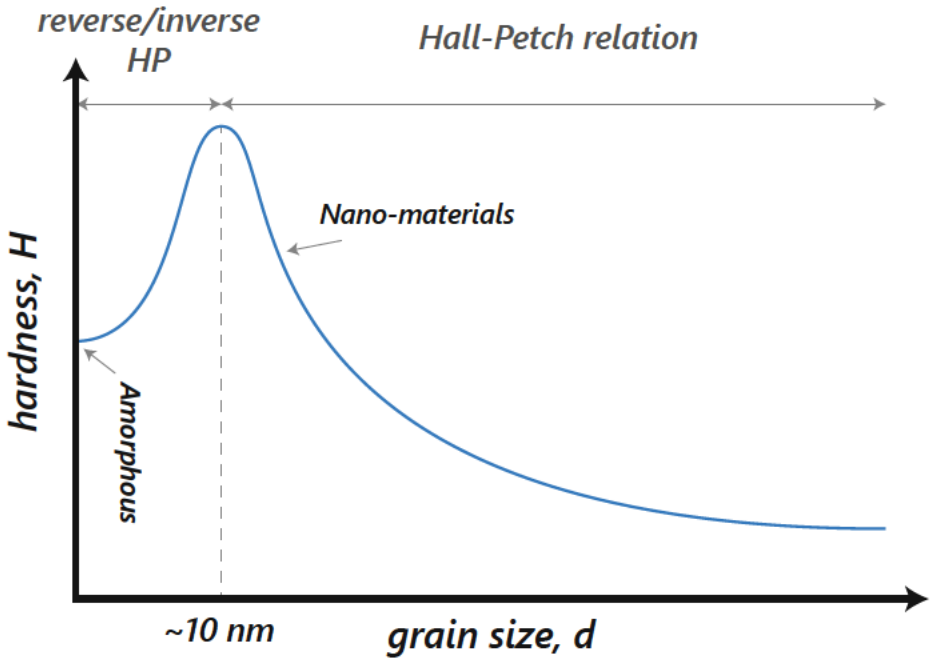

Fig. 2.7: Hardness as a function of grain size, illustrating the conventional and reverse/inverse Hall-Petch effect.

Precipitation strenghening The separation of insoluble materials within a matrix enables increasing materials strength. Incoherent precipitations or particles are bypassed, while coherent precipitates are cut by moving dislocations. Based on the two considerations, the effects are described by the so-called Orowan and Kelly Fine mechanism, respectively:

$$\tau = \tau_0 + const \cdot \sqrt{f_p} \frac{1}{r_p} \tag{2.34}$$

$$\tau = \tau_0 + const \cdot \sqrt{r_p f_p} \tag{2.35}$$

with particle radius r_p and volume fraction of particle f_p.

Chapter 3

Transition Metal Diborides

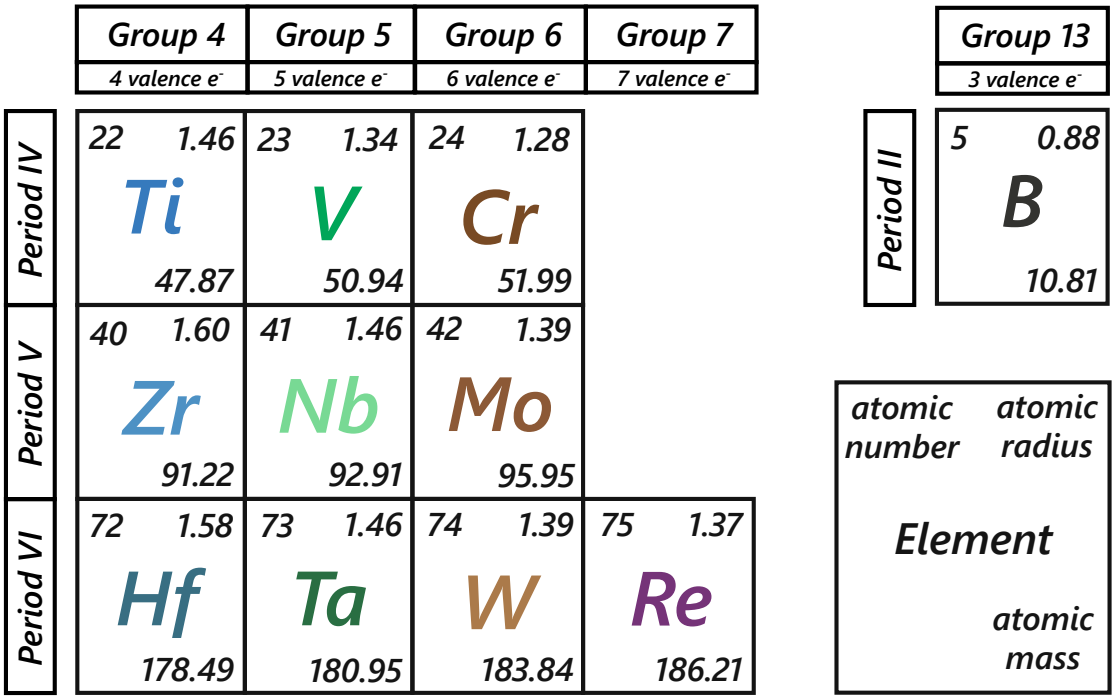

Fig. 3.1: Section of the periodic table of elements, highlighting group 3-7 and period IV-VI transition metals and group 13 period II Boron.

3.1 Crystal structure

In combination with the second row p-block element Boron (metalloid), the transition metals of groups 4 to 7 and period IV to VI (see Figure 3.1) exhibit a huge stoichiometric variation, forming plenty of crystal structures. One good example of structural and stoichiometric diversity is the Mo-B system, which reveals at least six stable or metastable intermetallic phases, represented by its binary phase diagram. There we can find the Mo_2B_5 phase, α-MoB

with MoB type structure, a possible Mo_3B_2 phase with U_3Si_2 type structure [54], M-rich Mo_2B phase with $CuAl_2$ type structure [55], B-rich MoB_4 with CrB_4-type structure [56], high temperature (> 1800°C) β-MoB phase with CrB-type structure [57] and MoB_2 with AlB_2 type structure.

Firstly determined by Hofmann and Jäniche in 1936 [58], the AlB_2 structure is also referred by the Strukturbericht designation C32 or α-type. Moreover, it is symmetrically described with space group 191 (SG191, P6/mmm) and the most prominent crystal structure for TMB_2. In 1950, Kiessling [21] showed that, except CrB_2, late transition metals from group 6, Mo and W, prefer the formation of the TM_2B_5 stoichiometry with Mo_2B_5 and W_2B_5 structure. The W_2B_5 structure is also known as ω-type and is described by space group 194 ($P6_3/mmc$). Later, Frotscher et al. demonstrated that Mo_2B_5 and W_2B_5 are not representing stoichiometry, which would be MoB_2 and WB_2. Only non-stoichiometric TMB_{2-z} prefer to crystalize in the AlB_2 phase (Frotscher showed it for MoB_{2-z}) [59]. Employing high-throughput density functional theory calculations, Moraes et al. pointed out that early TMB_2 (Group 4-5) favor the AlB_2 structure, whereas late TMB_2 (from group 6 and higher) prefer crystallizing in the W_2B_5 structure [22]. Figure 3.2 depicts these two competing hexagonal crystal structures, where the AlB_2 is characterized by alternating flat TM and B planes. In contrast, the W_2B_5 exhibits alternating flat and puckered B planes.

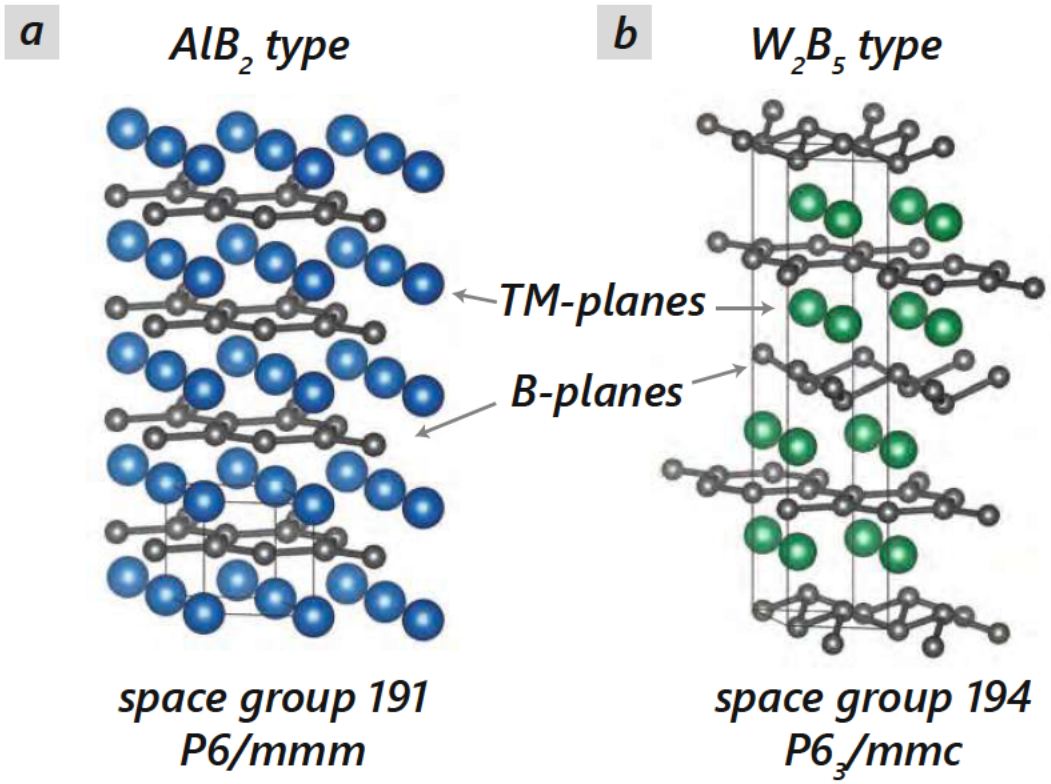

Fig. 3.2: Visualization of the AlB_2 type (a) and W_2B_5 type (b) crystal structure.

Furthermore, Moraes showed an α-phase stabilization by introducing vacancies to the crystal lattice. But also distinct alloying elements help decrease the formation energy of the AlB_2 structured TMB_2. Alloying Ta to the binary WB_2 material system is predicted to form a stable α-phase by simultaneously preserving ductile characteristics, which was also experimentally proved in Publication I [23, 60] [23], [61].

The TMB_2 belong to the Hägg phases (developed by Gunnar Hägg in 1930), describing the composition of TM and elements with smaller radius (B, N, C, etc.) occupying the interstitial sites. In the case of the AlB_2 structure, the B atoms occupy the trigonal prismatic interstitials, which size is dependent on the atomic radius of the prevalent TM. When comparing group 4-6 TMB_2 to TM-carbides (TMC) and -nitrides (TMN), the TMB_2 reveal a more metallic character. In contrast, TMC exhibit a higher covalent bonding type, while the TMN shows the most prominent ionic contribution [30].

3.2 Thin film synthesis

Synthesized as thin films, the AlB_2 structure is predominantly observed for TMB_2 material systems. In the particular case of WB_2, which is, from a thermodynamic point of view, stable in the ω-structure, defects are suggested for stabilization of the experimentally obtained α-phase. During condensation from vapor to solid phase, high cooling rates on the substrate material force significant amounts of defects (vacancies, dislocations) due to limited adatom kinetics. PVD techniques operate far from the thermodynamic equilibrium, as seen by AlB_2 structured MoB_2 material system, which is thermodynamically stable above 1500°C (apparent from its binary B-TM phase diagram). Still, it was deposited by Malinovskis et al. under UHV conditions at 300°C [61]. In the present study the two main techniques for depositing TMB_2 were direct current magnetron sputtering (DCMS) and arc-evaporation.

3.2.1 DC magnetron sputtering

In contrast to thermal evaporation, the main principle of sputtering is solely based on the momentum transfer of ions and neutrals. A negative voltage is applied to a solid target material (cathode) located within a deposition chamber (anode). Due to the applied electric field, an Ar working gas is ionized, leading to the ignition of a plasma. Ar^+ ions are accelerated towards the negative potential of the target, ejecting atoms and clusters and hence "sputter" them towards the substrate material. A negative potential (BIAS) is often applied to the substrate material, which can help adjust the film morphology by re-sputtering phenomena. To increase the efficiency of the sputter process (sputter yield), a magnet is placed behind the target material. The circular magnetic field lines perpendicular to the target trap electrons from the plasma at the surface near regions. Electrons move in a helix trajectory around

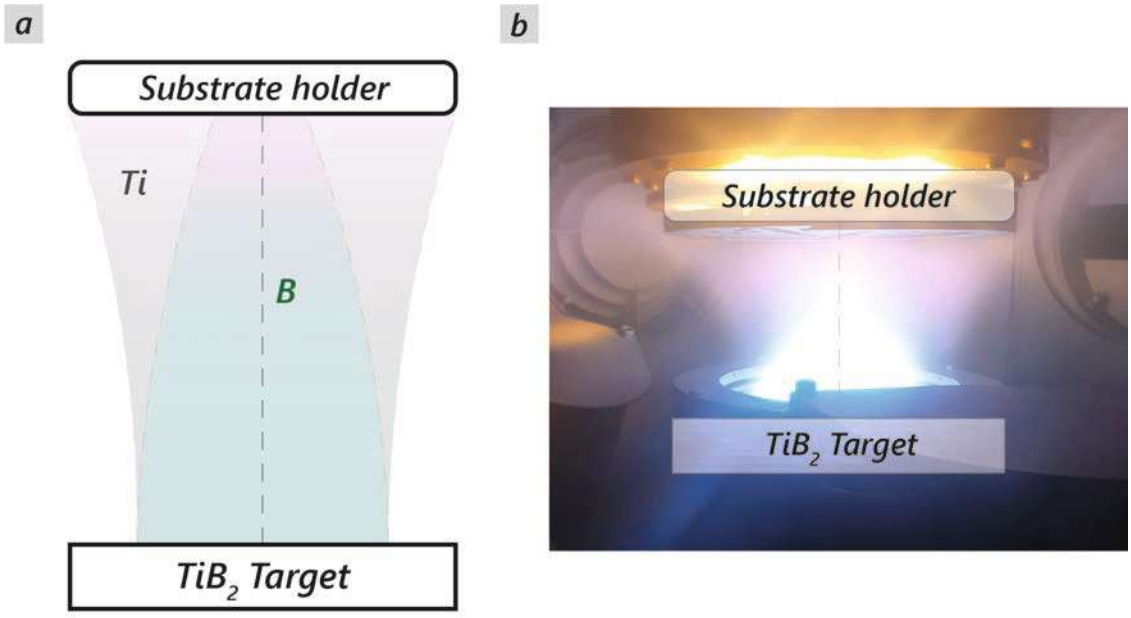

Fig. 3.3: Schematic of B and Ti distribution in the plasma upon sputter deposition of a TiB_2 compound target (a). A snapshot of a sputter plasma during deposition from a 6-inch TiB_2 compound target is depicted in b.

the magnetic field lines according to the Lorenz force. This leads to pronounced ionization, forcing an increased sputter yield even at lower voltages.

When sputtering TMB_2 from a compound target, one has to consider the atomic mass mismatches of Ar^+ ions (m_{Ar} = 39.95 u), B (m_B = 10.81 u) and sputtered TM atoms (e.g. m_{Ti} = 47.87 u, m_W = 183.84 u). Olsen et al. found that lighter elements are preferentially emitted along the target normal at low energy sputtering. Thus, off-stoichiometric film compositions concerning the target stoichiometry [62] are obtained. In a comprising study from 2008, Neidhardt et al. investigated the sputtering processes of Ti_xB (x = 0.5, 1, 1.6) compound targets experimentally and theoretically by TRIM and TRIDYN simulations [28]. The results reveal the different angular distributions of sputtered B and Ti atoms, whereas B is emitted along the target normal, while Ti follows a shallower distribution (see Figure 3.3). This effect leads to the pronounced excess B within sputtered Ti_xB thin films but can be altered by varying the deposition pressure, target substrate distance, and target substrate angle. The changing growth conditions impact on the gas-phase transport of the sputtered species, determining the mean free path (MFP) of B and Ti atoms. The difference in MFP of B (r_B = 0.88 Å) and Ti (r_{Ti} = 1.46 Å) of 24.9 cm and 13.4 cm, respectively, at 0.4 Pa and 800 K, resulting in different scattering of the atoms, affecting the B/Ti film ratio.

The used formula for determining the MFP is given as follows:

$$MFP = \frac{1}{\sqrt{2}} \frac{k_B T}{p} \frac{1}{\pi (r_{Ar} + r_{B,TM})^2} \tag{3.1}$$

with Boltzmann constant k_B, temperature T, pressure p, and radii of the involved atoms (r_{Ar} = 0.71 Å, r_B, r_{TM}).

3.2.2 Arc evaporation

For the ignition of a highly energetic emitting area, called arc spot (cathode spot), forced by a short contact of anode and cathode (target), extremely high currents (> 100 A) and low voltages (> 10 V) are applied. With a localized temperature up to 15000 K and a current density of 10^4 – 10^6 Acm^{-2}, the arc spot erodes the target material and expands the cathode plasma into the low-pressure atmosphere. What appears as a moving arc spot for the human eye is a sequence of ignition and extinction of electron and plasma emission centers [63]. Thus, the arc spot is only active for a short period (tens of nanoseconds) before moving to a new, less resistive area, close to the previous crater, forming a new emission center. Due to the high power density of the arc spot, the material is leaving the cathode surface region as ions, neutral vapor, and macro-particles (droplets). If incorporated into the thin film, the ejected macro-particles often cause undesired growth defects and weak spots. The arc spot can be trapped by magnetic field lines, arising from permanent – or electromagnets, placed behind the cathode to achieve a constant target erosion. This method forces the arc to run over the entire target surface.

The field of TMB_2 arc evaporation is weakly investigated, and only a few authors have contributed. Knotek is one of the authors who studied the DC arc deposition of high-pressure sintered TiB_2 cathode material, with additions of Al and Ni (< 1 wt. %) including C and B in the Ar and Ar/N_2 plasma [64]. He obtained local overheating of the target due to a not moving arc spot and the emission of glowing solid macro-particles. Still, resulting in the deposition of crystalline TiB_2 thin films with pronounced hardness, but with no provided composition.
In a further publication from Treglio et al. in 1993, the influence of pulsed arc and bias on the arc spot behavior was studied [65]. Minor ejection of glowing macro-particles was observed, but no information about stoichiometry or structure provided.
The influence of an external magnetic field on the arc spot movement was investigated by Zhirkov et al. in 2015 [66]. The absence of a magnetic field improved the arc deposition of a TiB_2 cathode. Moreover, a B/Ti ratio of 1 was observed for the deposited films.

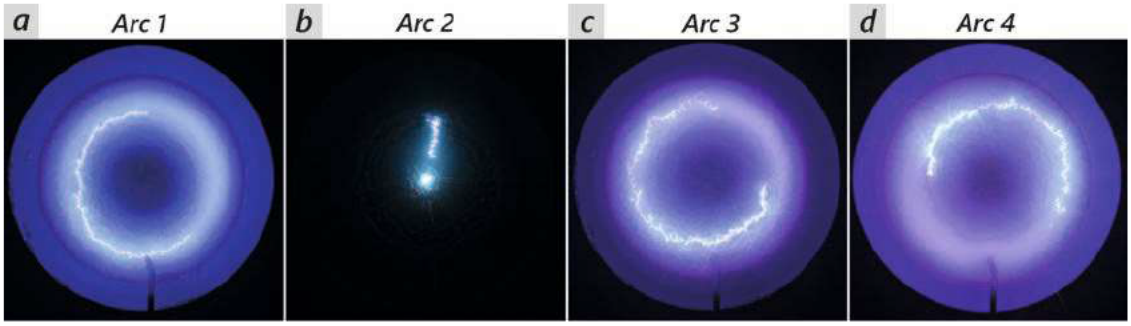

Fig. 3.4: Influence of various magnetic systems on the arc spot behavior of a TiB_2 cathode.

During the present study the influence of magnetic field strength, working gases (Ar, N), arc current modes, and bias voltage on the behavior of the arc spot formation and resulting coating materials was investigated. Figure 3.4 depicts snapshots of arc spot movements affected by magnetic field strength. A stable movement is observed for all variations, whereas the arc in Figure 3.4a, c, and d revealed a circular movement, whereas in Figure 3.4b a more random spot motion was recognizable. The experiments exhibit elevated ejection of glowing macro-particles for the magnetic configuration preferring a more accidental movement.

To ensure an arc ignition as well as a proper stability of the moving arc, high Ar flow rates have been used. Our investigations exhibit the necessity of using working gas, as no stable arc spot movement could be achieved in pure vacuum. Nevertheless, the arc evaporated TiB_2 compound target revealed an erosive mass loss of > 60 g/h leading to pronounced surface erosion spots, even clearly visible after the deposition process. In extreme cases, the target material evinced drastic erosive sinkholes, indicating seizing arcs.

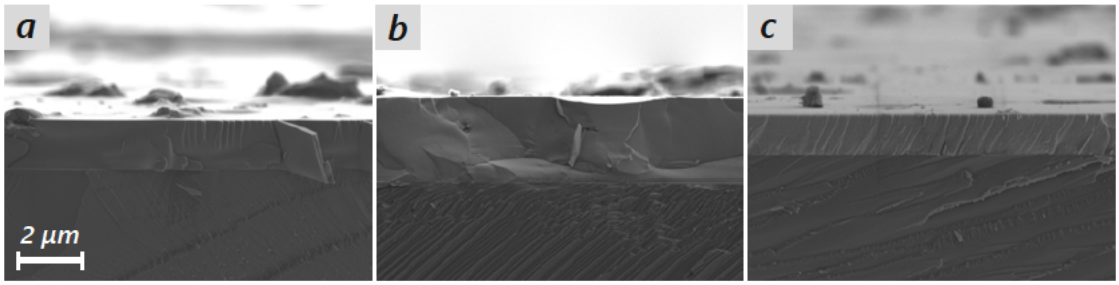

Fig. 3.5: SEM cross-sections of arc evaporated TiB_2 thin films from magnetic field strenght variation (a)-(c).

Still, thin films of up to 3 μm thickness have been synthesized on diverse substrate materials (the most promising are depicted in Figure 3.5), revealing proper deposition rates. Sub-stoichiometric compositions of the amorphous thin films are determined by LICP-OES technique. Substrate bias potential showed only a marginal impact on any coating characteristics.

3.3 Microstructure and texture

A comprising study from Mitterer in 1997 [12] on sputter-deposited TM, including TiB_2 and ZrB_2, revealed extremely fine-grained to amorphous structures at low substrate temperatures. Mitterer attributed this microstructure to the strong directionality of the covalent B-B bonds. In 2004, Mayrhofer et al. observed a nano-columnar structure of non-stoichiometric $TiB_{2.4}$, where excess B was segregated on the grain boundaries, forming B-rich tissue phases [13]. The film exhibited column diameters of ~20 nm with predominant 0001 crystal orientation further separated into ~5 nm sub-columns, surrounded by ultra-thin tissue phases. Mayrhofer correlated this microstructural characteristic to the pronounced hardness values of > 40 GPa, as the tissue phases prohibit grain boundary sliding and dislocation gliding. A similar microstructure was observed for stoichiometric ZrB_2 and $ZrB_{2.5}$, with nanoindentation hardness up to 45 GPa [67, 68]. Even for sub-stoichiometric NB_{2-x} with H≈42 GPa, Nedfors et al. could prove an existing B-rich tissue [69].

In 1986, Holleck firstly addressed the significant anisotropic hardness of hexagonal TiB_2. He postulated a deviation of about 30% depending on the film orientation [26]. A firm texture-dependent hardness for TiB_2 thin films was also observed by [70].

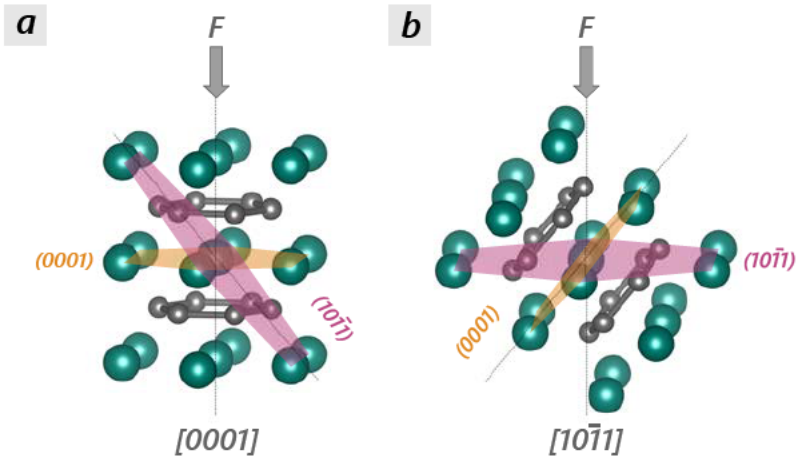

Fig. 3.6: Illustration of the preferred slip plane in AlB_2 structured TMB_2 with 0001 (a) and $10\bar{1}1$ (b) texture from [71].

The pronounced anisotropy of the hexagonal AlB_2 structure is ascribed to aggravated dislocation movement on energetically unpreferred slip systems. Hunter et al. [72] provide DFT calculations by considering various active slip systems in hexagonal ZrB_2. They investigated the generalized stacking fault energies and found energetically most accessible ⟨a⟩ type basal slip, followed by pyramidal $\langle 1\bar{2}10\rangle 10\bar{1}\bar{1}$ and both prismatic $\langle 1120\rangle 10\bar{1}0$ slip systems. Consequently, dislocation movement along the easiest 0001 slip plane is unlikely, when

applying a force perpendicular to this plane, as depicted in Figure 3.6 (e.g. at indentation experiments).

3.4 Theoretical approach on TMB_2

The drastic increase in computational power enabled the field of computational materials science to become one of the fastest-growing fields in science. Many powerful theoretical approaches strive to access particular material properties or physical movements of atoms and molecules and allow for simulation of distinct material loading and deformation scenarios. In-depth developed and well-accepted techniques are for example Molecular Dynamics (based on numerically solving Newton's equations of motion), Monte Carlo simulations (probability theory and random sampling) and Finite Elements Methods (numerical approach to solve partial differential equations from linear elasticity or fluid dynamics). In contrast, Density Functional Theory, as part of ab-initio methods, is based on quantum mechanics. It provides an algorithmic approach, for analytically solving the time-independent Schrödinger equation for quantum many-body problems:

$$\hat{H}\psi = E\psi \tag{3.2}$$

with Hamilton operator $\hat{H}$, energy of the system E, and wave function ψ.

3.4.1 Density functional theory

The final breakthrough of DFT was Kohn and Sham's theorems, providing the Kohn-Sham equation as a simplification of the Schrödinger equation, replacing probabilistic wave functions by electron densities. One major part of the Kohn-Sham Hamiltonian is the exchange-correlation potential (LDA, GGA [73]). To solve the KS equation, different packages like VASP [74] (providing plane wave pseudo-potentials [PW-PP] [75] using the projector augmented wave [PAW]) or WIEN2k (using full-potential linear augmented plane waves [FP-LAPW]) are offered. This study has used the Vienna Ab initio Simulation Package (VASP), operated at the Vienna Scientific Cluster (VSC), for the screening of group 4-6 (including ReB_2) TMB_2, utilizing structural properties (Energy of formation, elastic constant).

Energy of formation of shear deformed TMB_2 supercells AlB_2 structured 2x2x2 supercells of various TMB_2 from group 4-6, including ReB_2, have been shear deformed in $[10\bar{1}0]$ direction by altering the c-lattice vector within the POSCAR file. The resulting shear deformation was further increased, so that TM-atoms are shifted for one entire atom position in $[10\bar{1}0]$ direction, with respect to the underneath TM-plane. The progress in deformation is depicted in Figure 3.7, ranging from 0% to 50% and 100% shear deformation.

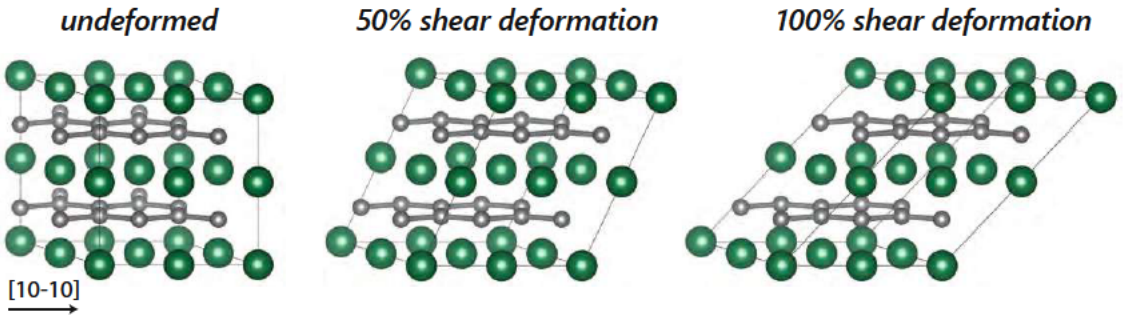

Fig. 3.7: Visualization of a 2x2x2 α-type TMB_2 supercell in undeformed state and after shear deformation (50%, 100%) in $[10\bar{1}0]$ direction.

Energy of formation (E_f) of the fully converged, shear deformed supercells are evaluated for the individual TMB_2. Figure 3.8 illustrates the relative change in E_f as a function increasing shear deformation progress (in %), indicating the highest energy demandingness for shearing TiB_2 followed by VB_2, NB_2, TaB_2, MoB_2, WB_2 and ReB_2. When assuming that shear resistance in $[10\bar{1}0]$ direction is mainly related to the inter-layer TM-B bonds, we can conclude that these bonds are strongest for group 4 TMB_2, decreasing for higher groups. The observed data can be interpreted as the structure's resistance to shear deformation in $[10\bar{1}0]$ direction, representing the shear modulus of the individual TMB_2. Moreover, a correlating trend with the materials melting points is not surprising (the highest melting point of 3200°C for TiB_2 decreasing to 2300°C for WB_2) due to the bond strength aspect.

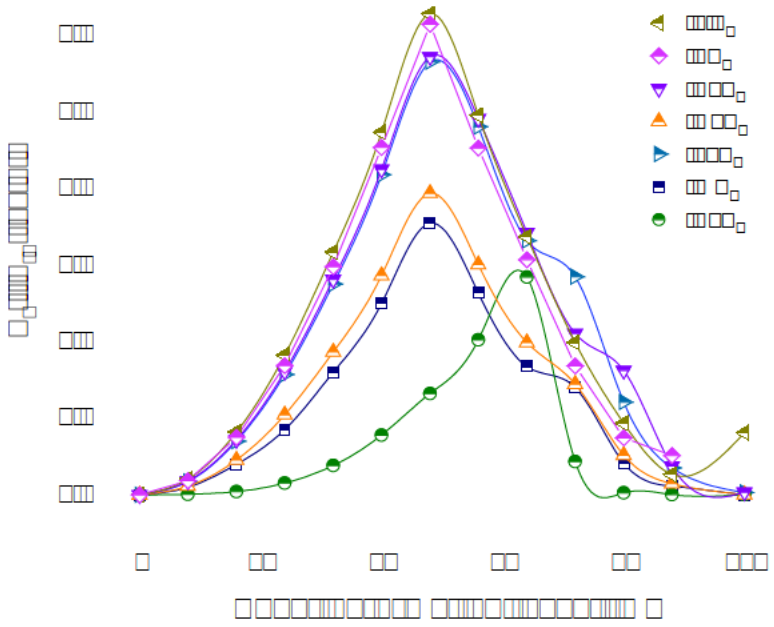

Fig. 3.8: Relative energy of formation E_f-E_{f0} (E_{f0} from undeformed cell) as a function of shear deformation in $[10\bar{1}0]$ direction for various AlB_2 structured group 4-8 TMB_2.

Elastic constants Using theoretical calculations, accessing the elastic material properties is a valuable approach for pre-selecting promising material systems. Hence, all the elastic constants of α-structured group 4-6 TMB_2, including ReB_2 from group 7, are determined by applying the stress/strain method [76]. The calculated stiffness tensor C is projected to hexagonal symmetry, following Moakher et al. [77]. Elastic constants are calculated from the hexagonal stiffness matrix, applying the Voigt-Reuss-Hill homogenization, as implemented in the online tool SC-EMA [78, 79]. Furthermore, the investigated TMB_2 has been screened by means of shear modulus G, bulk modulus B and Poisson's ratio ν, which allows the material systems to be classified into brittle and ductile regions after the criteria of Pugh and Frantsevic [80–82]. TiB_2 reveals the highest G/B ratio (G = 257 GPa, B = 255 GPa) and lowest $\nu = 0.12$; hence, classified as most brittle of the investigated TMB_2 by satisfying the criteria of Pugh and Frantsevic. In contrast, ReB_2 is classified as most ductile, revealing lowest G/B (G = 76 Ga, B = 330 GPa) and highest $\nu = 0.39$. Here, we have to mention that ReB_2 was calculated by using the α-structure whereas the ReB_2-type structure would be the most stable one for this material system. In summary, group 4 TMB_2 are classified as most brittle followed by group 5, 6 and α-ReB_2. The ordering from brittle to ductile regions of the investigated TMB_2 is similar to the ordering from highest to lowest energy demandingness during shear deformation. For comparison, elastic constant values of TiAlN [83] and CrAlN [84], extracted from literature, have been added to Figure 3.9.

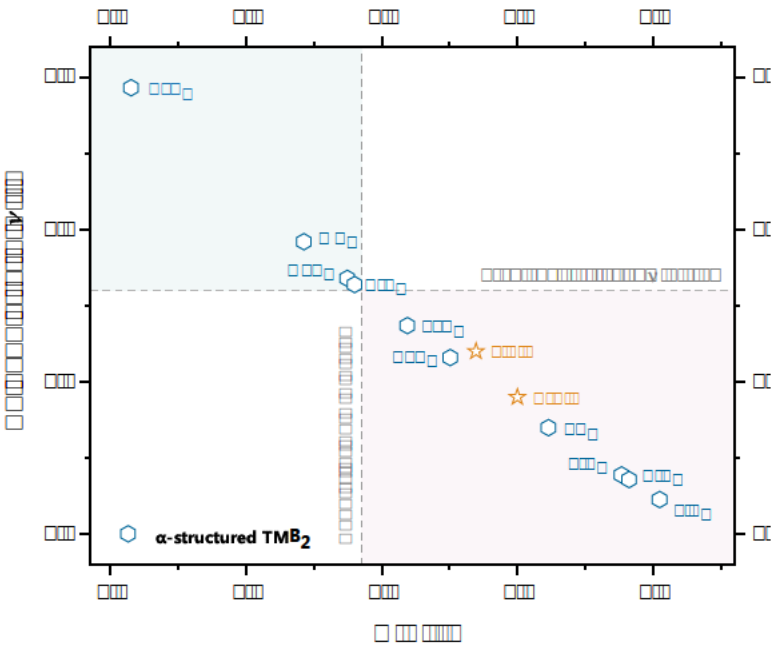

Fig. 3.9: Poisson's ratio ν as a function of G/B ratio, classifying group 4-8 TMB_2 into brittle and ductile regions.

3.4.2 Bonding characterization using LOBSTER

Usually, density of states (DOS) function provides directionless averaged information about the electronic structure, giving insights into prevalent bonding types. Nevertheless, the DOS approach states no information about a definite bonding (TM-TM, TM-B, B-B) within a crystal lattice. The crystal orbital overlap population (COOP) is a technique that provides information about electrons participating in the bond formation. As apparent from its name, this technique considers electron overlaps of chosen orbitals positioned on different atoms, partitioning atom interactions into bonding (positive COOP), antibonding (negative COOP) and nonbonding (COOP is zero) [85, 86]. Another technique for determining energies of bond interactions instead of orbital overlaps, is the crystal orbital Hamilton population (COHP) function [87]. Stabilizing interactions (bonding) are stated by negative COHP and destabilizing (antibonding) by a positive COHP function. Moreover, the bonding strength is given by the integrated COHP (ICOHP). The local-orbital basis suite towards electronic-structure reconstruction (LOBSTER) was developed to access this bonding characterization functions as an extension compatible with DFT and PAW codes [88].

A comprising study about inter-atomic interactions in group 4-8 TMB_2 is realized by Janovec [89]. Based on ab-initio calculations using VASP, he comprehensively characterized prevalent bonding types within AlB_2 structured diborides. Hence, COHP, COOP and DOS functions are determined, accessible through the LOBSTER package. He states that large charge transfer to B atoms supports strong B-B interaction due to additional π bonding. In contrast, the TM-B bond gets strengthened accompanied by only low charge transfer to the B atoms. The interaction of atomic bonds during shear deformation (using the VASP output files from the shear deformation experiments from the present study), compression, and tension is investigated. Shear deformation weakens the B-B interaction and supports TM-B bond stability due to lowered electron transfer from TM atoms in sheared crystals. In general, TiB_2 is most difficult to shear, while group 4 & 5 TMB_2 are the most difficult to compress. Most difficult to deform in tension are ReB_2 and TcB_2.

Bibliography

[1] J. H. Perepezko, The hotter the engine, the better, Science 326 (2009) 1068–1069.

[2] S. Vepřek, The search for novel, superhard materials, J. Vac. Sci. Technol. A 17 (1999) 2401–2420.

[3] A. A. Hamed, W. Tabakoff, R. B. Rivir, K. Das, P. Arora, Turbine blade surface deterioration by erosion (2005).

[4] E. Bousser, M. Benkahoul, L. Martinu, J. E. Klemberg-Sapieha, Effect of microstructure on the erosion resistance of Cr–Si–N coatings, Surf. Coat. Technol. 203 (2008) 776–780.

[5] W. G. Fahrenholtz, E. J. Wuchina, W. E. Lee, Y. Zhou, Ultra-high temperature ceramics: materials for extreme environment applications, John Wiley & Sons, 2014.

[6] I. Petrov, L. Hultman, U. Helmersson, J.-E. Sundgren, J. E. Greene, Microstructure modification of TiN by ion bombardment during reactive sputter deposition, Thin Solid Films 169 (1989) 299–314.

[7] O. Knotek, F. Löffler, H. J. Scholl, C. Barimani, The multisource arc process for depositing ternary cr- and ti-based coatings, Surf. Coat. Technol. 68-69 (1994) 309–313.

[8] W.-D. Münz, Titanium aluminum nitride films: A new alternative to TiN coatings, J. Vac. Sci. Technol. A 4 (1986) 2717.

[9] R. Rachbauer, S. Massl, E. Stergar, D. Holec, D. Kiener, J. Keckes, J. Patscheider, M. Stiefel, H. Leitner, P. H. Mayrhofer, Decomposition pathways in age hardening of Ti-Al-N films, J. Appl. Phys. 110 (2011) 023515.

[10] Y. Moritz, C. Saringer, M. Tkadletz, A. Stark, N. Schell, I. Letofsky-Papst, C. Czettl, M. Pohler, N. Schalk, Oxidation behavior of arc evaporated TiSiN coatings investigated by in-situ synchrotron x-ray diffraction and HR-STEM, Surf. Coat. Technol. 404 (2020) 126632.

[11] M. Magnuson, L. Hultman, H. Högberg, Review of transition-metal diboride thin films, Vacuum (2021) 110567.

[12] C. Mitterer, Borides in thin film technology, J. Solid State Chem. 133 (1997) 279–291.

[13] P. H. Mayrhofer, C. Mitterer, J. G. Wen, J. E. Greene, I. Petrov, Self-organized nanocolumnar structure in superhard TiB2 thin films, Appl. Phys. Lett. 86 (2005) 1–3.

[14] R. W. Cumberland, M. B. Weinberger, J. J. Gilman, S. M. Clark, S. H. Tolbert, R. B. Kaner, Osmium diboride, an Ultra-Incompressible, hard material, J. Am. Chem. Soc. 127 (2005) 7264–7265.

[15] J. Nagamatsu, N. Nakagawa, T. Muranaka, Y. Zenitani, J. Akimitsu, Superconductivity at 39 K in magnesium diboride, Nature 410 (2001) 63.

[16] G. V.a., S. N.s., Z. I.i., K. M.p., Electron transport in diborides: Observation of superconductivity in ZrB2, JETP Lett. 73 (2001) 532– 535.

[17] J. A. Mathews, Review and bibliography of the metallic carbides, Smithsonian Miscellaneous Collections (1898).

[18] T. S.a., M. H.r., The preparation of a new metal boride, Proc Chem Soc Lond 17 (1901).

[19] P. Ehrlich, Beitraege zur chemie des titans, in: Angewandte Chemie, volume 59, VCH Publishers Inc 303 NW 12TH AVE, Deerfield Beach, FL 33442-1788, 1947, p. 163.

[20] R. Kessling, The binary system zirconiumboron, Acta Chem. Scand. 3 (1949) 90.

[21] R. Kiessling, The borides of some transition elements : 4 (1950).

[22] V. Moraes, H. Riedl, C. Fuger, P. Polcik, H. Bolvardi, D. Holec, P. H. Mayrhofer, Ab initio inspired design of ternary boride thin films, Sci. Rep. 8 (2018) 9288.

[23] V. Moraes, C. Fuger, V. Paneta, D. Primetzhofer, P. Polcik, H. Bolvardi, M. Arndt, H. Riedl, P. H. Mayrhofer, Substoichiometry and tantalum dependent thermal stability of α-structured W-Ta-B thin films, Scr. Mater. 155 (2018) 5–10.

[24] J. G. Ryan, S. Roberts, G. J. Slusser, E. D. Adams, The preparation and characterization of titanium boride films, Thin Solid Films 153 (1987) 329–339.

[25] T. Larsson, H. O. Blom, S. Berg, M. Östling, Reactive sputtering of titanium boride, Thin Solid Films 172 (1989) 133–140.

[26] H. Holleck, Material selection for hard coatings, J. Vac. Sci. Technol. A 4 (1986) 2661–2669.

[27] M. Berger, L. Karlsson, M. Larsson, S. Hogmark, Low stress TiB2 coatings with improved tribological properties, Thin Solid Films 401 (2001) 179–186.

[28] J. Neidhardt, S. Mráz, J. M. Schneider, E. Strub, W. Bohne, B. Liedke, W. Möller, C. Mitterer, Experiment and simulation of the compositional evolution of Ti–B thin films deposited by sputtering of a compound target, J. Appl. Phys. 104 (2008) 063304.

[29] I. Petrov, A. Hall, A. B. Mei, N. Nedfors, I. Zhirkov, J. Rosen, A. Reed, B. Howe, G. Greczynski, J. Birch, L. Hultman, J. E. Greene, Controlling the boron-to-titanium ratio in magnetron-sputter-deposited TiB x thin films, J. Vac. Sci. Technol. A 35 (2017) 050601.

[30] G. W. Rayner-Canham, G. Rayner-Canham, T. Overton, Descriptive inorganic chemistry, Macmillan, 2003.

[31] K. Matoy, H. Schönherr, T. Detzel, T. Schöberl, R. Pippan, C. Motz, G. Dehm, A comparative micro-cantilever study of the mechanical behavior of silicon based passivation films, Thin Solid Films 518 (2009) 247–256.

[32] S. Brinckmann, C. Kirchlechner, G. Dehm, Stress intensity factor dependence on anisotropy and geometry during micro-fracture experiments, Scr. Mater. 127 (2017) 76–78.

[33] S. Brinckmann, K. Matoy, C. Kirchlechner, G. Dehm, On the influence of microcantilever pre-crack geometries on the apparent fracture toughness of brittle materials, Acta Mater. 136 (2017) 281–287.

[34] F. Mouhat, F. X. Coudert, Necessary and sufficient elastic stability conditions in various crystal systems, Phys. Rev. B 90 (2014) 0–3.

[35] TABOR, D., The hardness and strength of metals, J. Inst. Met. 79 (1951) 1.

[36] P. Zhang, S. X. Li, Z. F. Zhang, General relationship between strength and hardness, Materials Science and Engineering: A 529 (2011) 62–73.

[37] H. Hertz, On the contact of elastic solids, Z. Reine Angew. Mathematik 92 (1881) 156–171.

[38] S. Timoshenko, J. N. Goodier, Stresses in a circular disk, Theory of Elasticity, Second Edition, McGraw-Hill, New York, NY (1951) 107–111.

[39] A. C. Fischer-Cripps, Nanoindentation, Mechanical engineering series, 2. ed.. ed., Springer, New York, NY [u.a.], 2004.

[40] W. C. Oliver, G. M. Pharr, An improved technique for determining hardness and elastic modulus using load and displacement sensing indentation experiments, J. Mater. Res. 7 (1992) 1564–1583.

[41] I. N. Sneddon, Boussinesq's problem for a rigid cone, Math. Proc. Cambridge Philos. Soc. 44 (1948) 492–507.

[42] V. DIN Deutsches Institut für Normung e, D. I. N. G. I. F. Standardization, Metallische Werkstoffe—Instrumentierte eindringprüfung zur bestimmung der härte und anderer Werkstoffparameter—Teil 1: Prüfverfahren (ISO 14577-1: 2015), 2015.

[43] B. R. Lawn, A. G. Evans, D. B. Marshall, Elastic/plastic indentation damage in ceramics: The median/radial crack system, J. Am. Ceram. Soc. 63 (1980) 574–581.

[44] G. R. Anstis, P. Chantikul, B. R. Lawn, D. B. Marshall, A critical evaluation of indentation techniques for measuring fracture toughness: I, direct crack measurements, J. Am. Ceram. Soc. 64 (1981) 533–538.

[45] D. Di Maio, S. G. Roberts, Measuring fracture toughness of coatings using focused-ion-beam-machined microbeams, J. Mater. Res. 20 (2005) 299–302.

[46] V. T. Srikar, S. M. Spearing, A critical review of microscale mechanical testing methods used in the design of microelectromechanical systems, Exp. Mech. 43 (2003) 238–247.

[47] J. Halling, The tribology of surface films, Thin Solid Films 108 (1983) 103–115.

[48] A. Leyland, A. Matthews, On the significance of the H/E ratio in wear control: a nanocomposite coating approach to optimised tribological behaviour, Wear 246 (2000) 1–11.

[49] T. Y. Tsui, G. M. Pharr, W. C. Oliver, C. S. Bhatia, R. L. White, S. Anders, A. Anders, I. G. Brown, Nanoindentation and nanoscratching of hard carbon coatings for magnetic disks, MRS Proceedings 383 (1995) 447.

[50] S. Hassani, M. Bielawski, W. Beres, L. Martinu, M. Balazinski, J. E. Klemberg-Sapieha, Predictive tools for the design of erosion resistant coatings, Surf. Coat. Technol. 203 (2008) 204–210.

[51] J. Deng, F. Wu, Y. Lian, Y. Xing, S. Li, Erosion wear of CrN, TiN, CrAlN, and TiAlN PVD nitride coatings, Int. J. Refract. Hard Met. 35 (2012) 10–16.

[52] T. Shimokawa, A. Nakatani, H. Kitagawa, Grain-size dependence of the relationship between intergranular and intragranular deformation of nanocrystalline al by molecular dynamics simulations, Phys. Rev. B 71 (2005) 1–8.

[53] J. Schiøtz, F. D. Di Tolla, K. W. Jacobsen, Softening of nanocrystalline metals at very small grain sizes, Nature 391 (1998) 561–563.

[54] P. Rogl, V. Romaka, J. Bursik, H. Michor, M. Reissner, G. Giester, V. Homolova, Structure and properties of a novel boride (V0.92Fe0.08)2FeB2 with partially ordered U3Si2-type, J. Alloys Compd. 746 (2018) 638–647.

[55] F. de la Rosa, J. R. Romero-Romero, J. L. López-Miranda, A. G. Hernández-Torres, G. Rosas, Phase transformation of the CuAl2 intermetallic alloy during high-energy ball-milling, Intermetallics 61 (2015) 51–55.

[56] A. Knappschneider, C. Litterscheid, J. Kurzman, R. Seshadri, B. Albert, Crystal structure refinement and bonding patterns of CrB4: A Boron-Rich boride with a framework of tetrahedrally coordinated B atoms, Inorg. Chem. 50 (2011) 10540–10542.

[57] T. Lundstrom, Structure, defects and properties of some refractory borides, J. Macromol. Sci. Part A Pure Appl. Chem. 57 (1985) 1383–1390.

[58] W. Hofmann, W. Jäniche, Die struktur von aluminiumborid AlB2, Zeitschrift für Physikalische Chemie 31B (1936) 214–222.

[59] M. Frotscher, W. Klein, J. Bauer, C.-M. Fang, J.-F. Halet, A. Senyshyn, C. Baehtz, B. Albert, M2B5 or M2B4? a reinvestigation of the Mo/B and W/B system, Z. Anorg. Allg. Chem. 633 (2007) 2626–2630.

[60] C. Fuger, V. Moraes, R. Hahn, H. Bolvardi, P. Polcik, H. Riedl, P. H. Mayrhofer, Influence of tantalum on phase stability and mechanical properties of WB2, MRS Communications 9 (2019) 375–380.

[61] P. Malinovskis, J. Palisaitis, P. O. Å. Persson, E. Lewin, U. Jansson, Synthesis and characterization of MoB2x thin films grown by nonreactive DC magnetron sputtering, J. Vac. Sci. Technol. A 34 (2016) 31511.

[62] R. R. Olson, M. E. King, G. K. Wehner, Mass effects on angular distribution of sputtered atoms, J. Appl. Phys. 50 (1979) 3677–3683.

[63] A. Anders, Cathodic arcs : from fractal spots to energetic condensation, Springer series on atomic, optical, and plasma physics, Springer, New York, NY, 2008.

[64] O. Knotek, F. Löffler, M. Böhmer, R. Breidenbach, C. Stößel, Ceramic cathodes for arc-physical vapour deposition: development and application, in: G. E. McGUIRE, D. C. McINTYRE, S. Hofmann (Eds.), Metallurgical Coatings and Thin Films 1991, Elsevier, Oxford, 1991, pp. 263–267.

[65] J. R. Treglio, S. Trujillo, A. J. Perry, Deposition of TiB2 at low temperature with low residual stress by a vacuum arc plasma source, Surface and Coatings Technology 61 (1993) 315–319.

[66] I. Zhirkov, A. Petruhins, L.-A. Naslund, S. Kolozsvári, P. Polcik, J. Rosen, Vacuum arc plasma generation and thin film deposition from a TiB2 cathode, Appl. Phys. Lett. 107 (2015) 184103.

[67] L. Tengdelius, E. Broitman, J. Lu, F. Eriksson, J. Birch, T. Nyberg, L. Hultman, H. Högberg, Hard and elastic epitaxial ZrB2 thin films on Al2O3(0001) substrates deposited by magnetron sputtering from a ZrB2 compound target, Acta Mater. 111 (2016) 166–172.

[68] D. L. J. Engberg, L. Tengdelius, H. Högberg, M. Thuvander, L. Hultman, Atom probe tomography field evaporation characteristics and compositional corrections of ZrB2, Mater. Charact. 156 (2019) 109871.

[69] N. Nedfors, O. Tengstrand, J. Lu, P. Eklund, P. O. Å. Persson, L. Hultman, U. Jansson, Superhard NbB2-x thin films deposited by dc magnetron sputtering, Surf. Coat. Technol. 257 (2014) 295–300.

[70] M. L. Wu, X. W. Lin, V. P. Dravid, Y. W. Chung, M. S. Wong, W. D. Sproul, Conventional and ionized magnetron sputter-deposition of nanocrystalline titanium diboride thin films, Tribol. Lett. 5 (1998) 131–134.

[71] C. Fuger, R. Hahn, L. Zauner, T. Wojcik, M. Weiss, A. Limbeck, O. Hunold, P. Polcik, H. Riedl, Anisotropic super-hardness of hexagonal WB2±z thin films, Materials Research Letters 10 (2022) 70–77.

[72] B. Hunter, X.-X. Yu, N. De Leon, C. Weinberger, W. Fahrenholtz, G. Hilmas, M. L. Weaver, G. B. Thompson, Investigations into the slip behavior of zirconium diboride, J. Mater. Res. 31 (2016) 2749–2756.

[73] J. P. Perdew, K. Burke, M. Ernzerhof, Generalized Gradient Approximation Made Simple, Phys. Rev. Lett. 77 (1996) 3865–3868.

[74] G. Kresse, J. Furthmüller, Efficient iterative schemes for *ab initio* total-energy calculations using a plane-wave basis set, Phys. Rev. B: Condens. Matter Mater. Phys. 54 (1996) 11169–11186.

[75] G. Kresse, D. Joubert, From ultrasoft pseudopotentials to the projector augmented-wave method, Phys. Rev. B Condens. Matter Mater. Phys. 59 (1999) 1758–1775.

[76] R. Yu, J. Zhu, H. Q. Ye, Calculations of single-crystal elastic constants made simple, Comput. Phys. Commun. 181 (2010) 671–675.

[77] M. Moakher, A. N. Norris, The closest elastic tensor of arbitrary symmetry to an elasticity tensor of lower symmetry, J. Elast. 85 (2006) 215–263.

[78] H. Titrian, U. Aydin, M. Friák, D. Ma, D. Raabe, J. Neugebauer, Self-consistent scale-bridging approach to compute the elasticity of multi-phase polycrystalline materials, MRS Proceedings 1524 (2013) mrsf12–1524–rr06–03.

[79] M. Friák, W. A. Counts, D. Ma, B. Sander, D. Holec, D. Raabe, J. Neugebauer, Theory-Guided materials design of Multi-Phase Ti-Nb alloys with Bone-Matching elastic properties, Materials 5 (2012) 1853–1872.

[80] M. A. Ali, M. A. Hadi, M. M. Hossain, S. H. Naqib, others, Theoretical investigation of structural, elastic, and electronic properties of ternary boride MoAlB, Physica Status Solidi A Appl. Res. (2017).

[81] S. H. Mir, P. C. Jha, M. S. Islam, A. Banerjee, W. Luo, S. D. Dabhi, P. K. Jha, R. Ahuja, Static and dynamical properties of heavy actinide monopnictides of lutetium, Sci. Rep. 6 (2016) 29309.

[82] S. F. Pugh, XCII. Relations between the elastic moduli and the plastic properties of polycrystalline pure metals, The London, Edinburgh, and Dublin Philosophical Magazine and Journal of Science 45 (1954) 823–843.

[83] I. A. Abrikosov, A. Knutsson, B. Alling, F. Tasnádi, H. Lind, L. Hultman, M. Odén, Phase stability and elasticity of TiAlN, Materials 4 (2011) 1599–1618.

[84] L. Zhou, D. Holec, P. H. Mayrhofer, First-principles study of elastic properties of cubic cr 1-xAlxN alloys, J. Appl. Phys. 113 (2013).

[85] R. Dronskowski, Computational chemistry of solid state materials: A guide for materials scientists, chemists, physicists and others, John Wiley & Sons, 2008.

[86] S. Steinberg, R. Dronskowski, The crystal orbital hamilton population (COHP) method as a tool to visualize and analyze chemical bonding in intermetallic compounds, Crystals 8 (2018) 225.

[87] R. Dronskowski, P. E. Bloechl, Crystal orbital hamilton populations (COHP): energy-resolved visualization of chemical bonding in solids based on density-functional calculations, J. Phys. Chem. 97 (1993) 8617–8624.

[88] S. Maintz, V. L. Deringer, A. L. Tchougréeff, others, LOBSTER: A tool to extract chemical bonding from plane-wave based DFT, Chemistry (2016).

[89] J. Jozef, Study of inter-atomic interactions in advanced materials with help of ab intio calculations, Ph.D. thesis, Brno University of Technology, 2021.

Chapter 4

Scientific Contributions

4.1 First-Author publications

Publication I

Anisotropic super-hardness of hexagonal WB_{2-z} thin films

C. Fuger, R. Hahn, L. Zauner, T. Wojcik, M. Weiss, A. Limbeck, O. Hunold, P. Polcik, H. Riedl, *Materials Research Letters (2022), 10:2, 70-77*

Based on density functional theory calculations, the stoichiometric WB_2 material system is thermodynamically stable in the W_2B_5 type (ω) structure. Nevertheless, this study reveals a AlB_2 (α) structure stabilization for DC magnetron sputtered WB_{2-z}, using a 6-inch W_2B_5 compound target material. This preferential AlB_2 type stabilization is achieved by pronounced defect crystal structures of PVD film materials. Increasing B vacancy concentration is proven to increase the thermodynamic stability of α-WB_{2-z}, leading to an energetic minimum at sub-stoichiometric α-$WB_{1.5}$. This theoretical result is experimentally underlined by matching lattice parameters, mechanical properties, and chemical compositions. Moreover, a strong anisotropy of the hardness is observed by nanoindentation. Super-hard α-WB_{2-z} thin films exhibit pronounced 0001 orientation compared to $10\bar{1}1$ textured coatings with a drop in hardness of more than 15 GPa. The energetically easiest to activate 0001 basal slip plane is unlikely to trigger when applying a force perpendicular to this plane, resulting in drastically higher hardness values for 0001 textured coatings. In contrast, no orientation influence on the fracture toughness is evident.

Publication II

Influence of Tantalum on the phase stability and mechanical properties of WB_2

C. Fuger, V. Moraes, R. Hahn, H. Bolvardi, P. Polcik, H. Riedl, and P.H. Mayrhofer, *MRS Communications (2019), 9, 375-380*

Adding Ta to binary α-WB_2 by co-sputtering a 6-inch TaB_2 and W_2B_5 compound target exhibits single-phase $W_{1-x}Ta_xB_{2-z}$ up to Ta contents of x = 0.26. Adapting perfect α-structured $W_{1-x}Ta_xB_{2-z}$ supercells with the experimentally obtained chemical compositions decreases the DFT calculated energy of formation, making them energetically preferable to the ω-structure. This is achieved by systematically removing atoms from the crystal lattice, introducing vacancies and Schottky defects. The investigated $W_{1-x}Ta_xB_{2-z}$ thin films with x = 0, 0.07, 0.14 and 0.26 exhibit increasing B contents from 59.3 at.% to 62.3 at.% determined by elastic recoil detection analysis (ERDA). Moreover, an increasing hardness from ≈40 GPa to ≈45 GPa with a slight decreasing tendency of the elastic modulus from ≈650 GPa to ≈620 GPa is measured. Subsequently, increasing H/E and H^3/E^2 ratios from 0.06 to 0.07 and 0.16 to 0.23, respectively, are evaluated. Maximum intrinsic fracture toughness (cantilever bending) is determined for the $W_{0.93}Ta_{0.07}B_{1.76}$ coating with 3.8 ± 0.5 MPa$\sqrt{m}$ (but highest error value), decreasing to 3.0 ± 0.2 MPa$\sqrt{m}$ with increasing Ta. The decreasing K_{IC} values of the $W_{1-x}Ta_xB_{2-z}$ films correlate with increasing G/B and decreasing Poisson's ratio (ductility parameter) received by DFT.

Publication III

Influence of Tantalum on the oxidation resistance of WB_{2-z} coatings

C. Fuger, B. Schwartz, T. Wojcik, V. Moraes, M. Weiss, A. Limbeck, C.A. Macauley, O. Hunold, P. Polcik, D. Primetzhofer, P. Felfer, P.H. Mayrhofer, and H. Riedl, *Journal of Alloys and Compounds (2021), 864, 158121*

The ternary α-$W_{1-x}Ta_xB_{2-z}$ material system is a promising candidate for a protective coating system, owing to high-temperature phase stability (≥ 1400°C), and enhanced fracture toughness (≥ 3 MPa$\sqrt{m}$) as well as super-hardness (evinced by Publication II). To complete the profile of properties, the oxidation behavior of $W_{1-x}Ta_xB_{2-z}$ with x = 0, 0.15, 0.34, 0.58, 0.81, and 1 is comprehensively investigated in Publication II. The oxidation treatments in ambient air reveal a stable oxide growth up to 700°C with decreasing scale thickness for Ta-rich

compositions. After 1000 min at a temperature of 600°C, the oxide scale thickness decreases steadily from 8.0 μm to 1.6 μm from WB_{2-z} to TaB_{2-z}. A para-linear scale growth with a rate constant of $k^*_p = 6.3 \cdot 10_{-4}$ $\mu m^2/s$ for WB_{2-z} changing to a linear scale growth with $k_l = 2.6 \cdot 10^{-5}$ μm/s for TaB_{2-z} is obtained. The addition of Ta to WB_{2-z} based thin films retards the oxide scale kinetics by forming denser, less volatile, and adherent scales underlined by detailed TEM observations. The optimum composition of $W_{1-x}Ta_xB_{2-z}$ based coatings would be x = 0.2-0.3, combining enhanced mechanical properties and thermal stability with decent oxidation resistance.

Publication IV

Revisiting the origins of super-hardness in TiB_{2+z} thin films – Impact of growth conditions and anisotropy

C. Fuger, R. Hahn, A. Hirle, P. Kutrowatz, M. Weiss, A. Limbeck, O. Hunold, P. Polcik and H. Riedl, *submitted at Surface and Coatings Technology*

Based on the comprehensive knowledge about sputter-deposited TiB_2, it was possible to realize a broad stoichiometry variation with B contents ranging from 67 at. % ($TiB_{2.07}$) up to 82 at.% ($TiB_{4.42}$). We highlight the strong angular distribution of sputtered B and Ti atoms by systematically varying the deposition pressure and target-substrate distance. The structural analysis confirms crystalline thin films even for super-stoichiometric compositions with a distinctive surplus B. A pronounced film orientation sensitivity on the deposition pressure is observed, with the preference for 0001 textured coatings to form at low pressures. In correlation to Publication I, the hexagonal TiB_{2+z} material system reveals a pronounced hardness anisotropy. While 0001 oriented films exceed super-hardness, upcoming $10\bar{1}1$ and 1000 orientations lead to a decrease by more than 10 GPa. Moreover, increasing B contents (B/Ti > 2.5) prefer the formation of smaller grains, underlined by decreasing coherently diffracting domain sizes. Consequently, a reverse/inverse Hall-Petch like behavior contributes to descending hardness of ≈5GPa. No predominant effect of a B-rich tissue phase on the elasto-plastic properties is observed. Maximum intrinsic fracture toughness of 3.02 ± 0.13 MPa$\sqrt{m}$ for the $TiB_{2.43}$ coating, slightly decreasing to K_{IC} = 2.51 ± 0.14 MPa$\sqrt{m}$ for $TiB_{4.42}$ is determined by micro-cantilever bending. This decreasing trend is attributed to smaller grain sizes and is further illuminated in Publication V.

Publication V

Tissue phase affected fracture toughness of nano-columnar TiB_{2+z} thin films

C. Fuger, R. Hahn, A. Hirle, T. Wojcik, P. Kutrowatz, L. Zauner, F. Bohrn, M. Weiss, A. Limbeck, O. Hunold, P. Polcik, and H. Riedl *in final preparation for submission at Nano Letters*

Detailed TEM investigations of topview prepared super-stoichiometric TiB_{2+z} thin films present the nano-columnar morphology. Column separating B-rich tissue phases are detected by in-situ EELS analysis, EFTEM and STEM imaging technique. Moreover, HR-TEM exposes insights into the nanocrystals and atomistic length scales of AlB_2 structured $TiB_{4.42}$. The investigated films revealed a pronounced 0001-texture with varying stoichiometry from $TiB_{2.43}$ to $TiB_{4.42}$. The surplus of B enforces smaller column sizes, decreasing from ≈8 nm to ≈2 nm, resulting in an increased tissue phase fraction of ≈10%. This leads to a declining K_{IC} from 3.0 to 2.5 MPa$\sqrt{m}$, suggesting crack propagation along tissue phases, providing the weakest pathways.

4.2 Co-Author publications

V. Moraes, **C. Fuger**, V. Paneta, D. Primetshofer, P. Polcik, H. Bolvardi, M. Arndt, H. Riedl, and P.H. Mayrhofer; **Substoichiometry and tantalum dependent thermal stability of α-structured W-Ta-B thin films**; *Scripta Materialia (2018), 155, 5–10; doi: 10.1016/j.scriptamat.2018.06.005.*

V. Moraes, H. Riedl, **C. Fuger**, P. Polcik, H. Bolvardi, D. Holec, and P.H. Mayrhofer; **Ab initio inspired design of ternary boride thin films**; *Scientific Reports (2018), 8:9288; doi: 10.1038/s41598-018-27426-w.*

4.3 Supervised Students

Bernadette Schwartz
Inuence of Ta on the oxidation resistance of WB_2 based thin films
Master thesis
Finished 07/2019

Bernhard Rath
Influence of deposition parameter on the structure and mechanical properties of TaB_2 thin films
Bachelor thesis
Finished 05/2020

Jozef Janovec
Study of inter-atomic interactions in advanced materials with help of ab-initio calculations
Master thesis in collaboration with the Institute of Materials Science and Engineering at Brno University of Technology
Finished 07/2021

Anna Viktoria Hirle
Influence of Mo on the structure and fracture-mechanical properties of TiB_{2+z} thin films
Master thesis
Finished 05/2022

4.4 Participation at International Conferences

Spring Meeting of the European Materials Research Society 2019
Nice, 27-31.5.2019
Influence of Tantalum on phase stability and mechanical properties of WB_2 thin films
C. Fuger, V. Moraes, R. Hahn, M. Arndt, H. Bolvardi, P. Polcik, P.H. Mayrhofer, and H. Riedl

Special PSE 2020
Erfurt, 07-10.9.2020
Oxidation resistance of Ta doped WB_{2-z} coatings
C. Fuger, B. Schwartz, T. Wojcik, V. Moraes, M. Weiss, A. Limbeck, C.A. Macauley, O. Hunold, P. Polcik, D. Primetzhofer, P. Felfer, P.H. Mayrhofer, and H. Riedl

ICMCTF 2021 Virtual Conference
26-30.4.2021
Thermomechanical Properties and Oxidation Resistance of Ternary $W_{1-x}Ta_xB_{2-z}$ coatings
C. Fuger, V. Moraes, R. Hahn, O. Hunold, M. Arndt, P. Polcik, P. H. Mayrhofer, and H. Riedl

AVS 67 Virtual Symposium
25-28.10.2021
Structure related investigations and fracture resistance of $TiMoB_2$ thin films
C. Fuger, A. Hirle, R. Hahn, M. Arndt, O. Hunold, S. Kolozsvári, P. Polcik, and H. Riedl

Chapter 5

Concluding remarks

This study presents structure- and morphology-related phenomena on the thermo-mechanical properties of binary and ternary AlB_2 type structured TMB_2 thin films, to push the stepwise convergence to application by a more detailed understanding. A special focus was placed on physical vapor deposited $WB_{2\pm z}$ as well as TiB_{2+z} based coating materials.

The intense elasto-plastic anisotropy of super-hard hexagonal α-WB_{2-z} coating materials is illustrated in Publication I. Due to lower generalized stacking fault energy of the <a> type basal slip planes, deviations from the perfect 0001 film texture lead to a drastic decrease in hardness of up to 15 GPa. Furthermore, the study revised the structural uncertainties of the competing α-WB_{2-z} and ω-WB_2. AlB_2-type WB_{2-z} prefers B vacant structures, showing the highest thermodynamic stability at α-$WB_{1.5}$ stoichiometry, whereas the pretended W_2B_5-type (WB_2 or W_2B_4) prefers to crystalize in the (nearly) perfect stoichiometric (uncertainties are related to calculational details).

The DC magnetron sputtered α-WB_{2-z} base system was used for a ternary TMB_2 design survey, applying Ta as an alloying element. The synthesized $W_{1-x}Ta_xB_{2-z}$ material system exhibited single-phased structures up to 26% Ta on the metallic sublattice. Further increasing Ta contents led to a separation into α-WB_{2-z}, α-TaB_{2-z}, and o-TaB with decreasing B contents (highlighted in Publication II and III). At low Ta contents ($< 26\%$), the hardness increased to ≈45 GPa at constant elastic modulus, whereas the intrinsic fracture toughness generally decreased but exhibited a maximum of ≈3.8 MPa$\sqrt{m}$ for α-$W_{0.97}Ta_{0.07}B_{1.76}$.

Moreover, a significant improvement in the oxidation behavior is highlighted in Publication III. As W-rich compositions revealed a para-linear oxide growth mode with substantial porous oxide scales, Ta-rich coatings showed a more linear growth mode with dense and retarded scale growth after 1000 min oxidation at 600°C. Consequently, Ta is proven to promote denser scale growth suppressing the volatile character of B oxides.

Subsequently, the AlB_2-type TiB_{2+z} material system was re-investigated by observing impacting growth conditions on the structure-mechanical properties. The highly differing angular distributions of sputtered B and Ti atoms led to pronounced off-stoichiometric compositions from $TiB_{2.07}$ to $TiB_{4.42}$, with crystalline nano-columnar morphologies. Moreover, the columns were separated by a 1 to 2 nm broad B-rich tissue phase, forming 3-dimensional frameworks. Still, the strong anisotropy was proven to have the highest impact on the hardness, whereas increasing B content forced smaller column sizes, promoting grain boundary sliding events. Both, decreasing 0001 orientation fraction and diminishing column size significantly reduced the hardness of nano-columnar α-TiB_{2+z}, highlighted within Publication IV. When not ideally 0001 oriented ($< 90\%$ 0001 fraction), the mentioned grain size dependent softening is less pronounced, attributed to easier to activate basal (0001) slip plane. Again, the study did not unfold a texture dependency of the fracture toughness. However, cantilever bending tests unveiled degressive fracture resistance with smaller column sizes.

Therefore, Publication V exposed a surplus of tissue phase fraction due to decreased column sizes of super-stoichiometric TiB_{2+z} films, which is the main contributor to fracture toughness as crack propagation is preferred along tissue phases.

Chapter 6

Publications in printed version

Publication I

Anisotropic super-hardness of hexagonal $WB_{2\pm z}$ thin films

C. Fuger, R. Hahn, L. Zauner, T. Wojcik, M. Weiss, A. Limbeck, O. Hunold, P. Polcik, and H. Riedl

Materials Research Letters (2022), 10:2, 70-77
doi: 10.1080/21663831.2021.2021308

citations (Google Scholar, April 19, 2022): 0

MATER. RES. LETT.
2022, VOL. 10, NO. 2, 70–77
https://doi.org/10.1080/21663831.2021.2021308

MATERIALS RESEARCH LETTERS
Taylor & Francis
Taylor & Francis Group

ORIGINAL REPORTS

Anisotropic super-hardness of hexagonal $WB_{2\pm z}$ thin films

C. Fuger [a], R. Hahn [a], L. Zauner [a], T. Wojcik [a], M. Weiss [b], A. Limbeck [b], O. Hunold [c], P. Polcik [d] and H. Riedl [a,e]

[a]Christian Doppler Laboratory for Surface Engineering of high-performance Components, TU Wien, Wien, Austria; [b]Institute of Chemical Technologies and Analytics, TU Wien, Wien, Austria; [c]Oerlikon Balzers, Oerlikon Surface Solutions AG, Balzers, Liechtenstein; [d]Plansee Composite Materials GmbH, Lechbruck am See, Germany; [e]Institute of Materials Science and Technology, TU Wien, Wien, Austria

ABSTRACT

Transition metal diboride-based thin films are promising candidates to replace state-of-the-art protective and functional coating materials due to their unique properties. Here, we focus on hexagonal WB_{2-z}, showing that the AlB_2 structure is stabilized by B vacancies exhibiting its energetic minima at sub-stoichiometric $WB_{1.5}$. Nanoindentation reveals super-hardness of 0001 oriented α-WB_{2-z} coatings, linearly decreasing by more than 15 GPa with predominant $10\bar{1}1$ orientation. This anisotropy is attributed to differences in the generalized stacking fault energy of basal and pyramidal slip systems, highlighting the feasibility of tuning mechanical properties by crystallographic orientation relations.

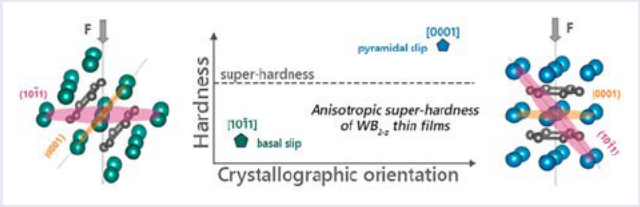

ARTICLE HISTORY
Received 20 September 2021

KEYWORDS
WB_2; physical vapour deposition; DFT; structural defects; anisotropy; super-hardness

IMPACT STATEMENT

First report of an anisotropic elastoplastic behaviour in super-hard PVD AlB_2 structured WB_{2-z}. Theoretical and experimental verification of thermodynamically most stable sub-stoichiometric α-WB_{2-z} coatings by structural and mechanical analysis.

Introduction

Transition metal diborides (TMB_2) exhibit a tremendous potential to be applied in various applications ranging from wear- and corrosion resistant coatings, superconductive thin films, up to extremely stable protective layers [1–4]. Diborides of group 2–5 prefer to crystallize in the hexagonal AlB_2 structure (α, space group 191—P6/mmm), while TMB_2 of group 6 and higher typically reveal the so-called W_2B_5 based structure (ω, space group 194—$P6_3/mmc$) [5,6]– except for CrB_2 [7,8]. Frotscher et al. already pointed out, that the pretended Mo_2B_5 and W_2B_5 are Mo_2B_4 and W_2B_4, whereas only non-stoichiometric compounds $TMB_{2\pm z}$ prefer to crystallize in the α-structure [9]. Nevertheless, due to strongly limited kinetics during physical vapour deposition (PVD), WB_{2-z} is stabilized in its metastable α-phase rather than in the thermodynamically preferred ω structure [10–12]. Structural defects—being predominant in PVD materials—are presumed to stabilize the α-phase. This is confirmed in detail for the TiB_2 material system, where sub-stoichiometric $TiB_{1.9}$ is stabilized by the absence of B between Ti-planes locally relaxing the structure [13].

In general, the enhanced hardness of hexagonal material systems is related to limited slip systems (slip plane and -direction)—compared to cubic systems—impeding dislocation movement and thus, plastic deformation [14]. Furthermore, in hexagonal SiC and GaN the dislocation motion and activated slip systems have been described and anisotropic mechanical properties were shown [15–19]. The experimental observations of SiC single crystal polytypes revealed higher hardness of basal indentations compared to prismatic indentations [15]. Moreover, Huang et al. indicated specific slip planes being

CONTACT C. Fuger christoph.fuger@tuwien.ac.at

Supplemental data for this article can be accessed here. https://doi.org/10.1080/21663831.2021.2021308

active during plastic deformation of GaN, suggesting that anisotropic elastoplastic mechanical properties correlate with plastic deformation [17]. In contrast, no distinct orientation-dependent fracture toughness could be detected so far [15,18].

Moreover, $WB_{2\pm z}$ is known for its enhanced material properties like hardness, Young's modulus as well as fracture toughness, and therefore often consulted as a base system forming ternary $TM_ITM_{II}B_{2\pm z}$ [10,11,20,21]. In previous studies, we successfully showed the positive effect of Ta alloying on the mechanical properties (H, K_{IC}), thermal stability, and oxidation resistance of $WB_{2\pm z}$ thin films [10,21,22].

The focus of this study is to obtain new insights into the elastoplastic behaviour of $WB_{2\pm z}$ thin films concerning their detailed structural constitution using different structural as well as micro-mechanical characterization techniques. Furthermore, theoretical investigations using ab initio methods should clarify structural uncertainties of the AlB_2 type $WB_{2\pm z}$.

Experimental

Computational details

DFT coded VASP [23,24] calculations using the projector augmented waves method within the generalized gradient approximation (PAW-PBE) [25] were applied to investigate the energy of formation (E_f) and elastic constants of α- and ω-structured WB_x cells ($x = 2\pm z$). The perfect, as well as the defected structures, were generated using the SQS special quasirandom structure (SQS) approach. The elastic constants were calculated using the stress/strain method [26], further details are described in the Supplementary Material.

Thin film synthesis

To offer a broad spectrum of deposition parameters beyond temperature, pressure, and bias, we used three different deposition systems. An in-house developed magnetron sputtering system (for details see Supplementary) an AJA International Orion 5 magnetron sputtering system, and an Oerlikon Balzers Innova deposition system providing diverse sputter configurations with different target-substrate distances and angles. The coating facilities have been equipped with six-inch and three-inch powder-metallurgically prepared W_2B_4 targets—manufactured by Plansee Composite Materials GmbH—exhibiting the ω- structure. The deposition processes were carried out in pure argon with a rotating substrate holder. For detailed information to the in-house developed system and on the variated parameter settings on each deposition system, see Table S1–3 in the Supplementary.

Characterization methods

For detailed structural characterization of all coatings deposited, a Philips XPERT diffractometer in Bragg–Brentano configuration, as well as the nanofocus endstation (DESY Petra III), were used (selected samples).

Hardness (H), and Young's modulus (E), of all films, were investigated by an Ultra Micro-Indentation System (UMIS), equipped with a Berkovich diamond tip. The resulted loading and unloading curves were evaluated after Oliver and Pharr [27] to gain H and E, respectively.

The elemental composition of selected films on Si substrates was analyzed by liquid inductively coupled plasma optical emission spectroscopy (ICP-OES). LICP-OES measurements were carried out on an iCAP 6500 RAD (Thermo Fisher Scientific, USA), with an ASX-520 autosampler (CETAC Technologies, USA) using an HF resistant sample introduction kit, consisting of a Miramist nebulizer (Burger Research, USA), a PTFE spray chamber and a ceramic injector tube. The WB_{2-z} coatings were acid digested with the method presented and validated in [28–30] –described in detail in the Supplementary Material.

In addition, one selected sample was surveyed by transmission electron microscopy (TEM FEI TECNAI, F20, acceleration voltage of 200 kV). Detailed structural information was gained by selected area electron diffraction (SAED). The sample preparation was done by focused ion beam (FIB, Quanta 200 3D DualBeam), applying a standard lift-out technique [31].

In situ micromechanical bending tests of substrate-free coating cantilevers are conducted to obtain the fracture toughness of selected coatings. The experiments were performed within an SEM equipped with a Hysitron PI-85 SEM pico-indenter whose spherical diamond tip was pressed onto the top of the pre-notched cantilever (in the growth direction of the coatings) until fracture [32]. The calculation of the fracture toughness was performed after Matoy et al. [33]—see also Supplementary Material.

Results and discussion

DFT calculations revealed the energy of formation, E_f, of perfect and defected α- and ω- structured $WB_{2\pm z}$ cells. In Figure 1(a) the development of E_f with increasing B vacancies (blue filled squares for α, red filled triangles for ω), W vacancies (blue half-filled squares for α, red half-filled triangles for ω) and Schottky defects (blue empty

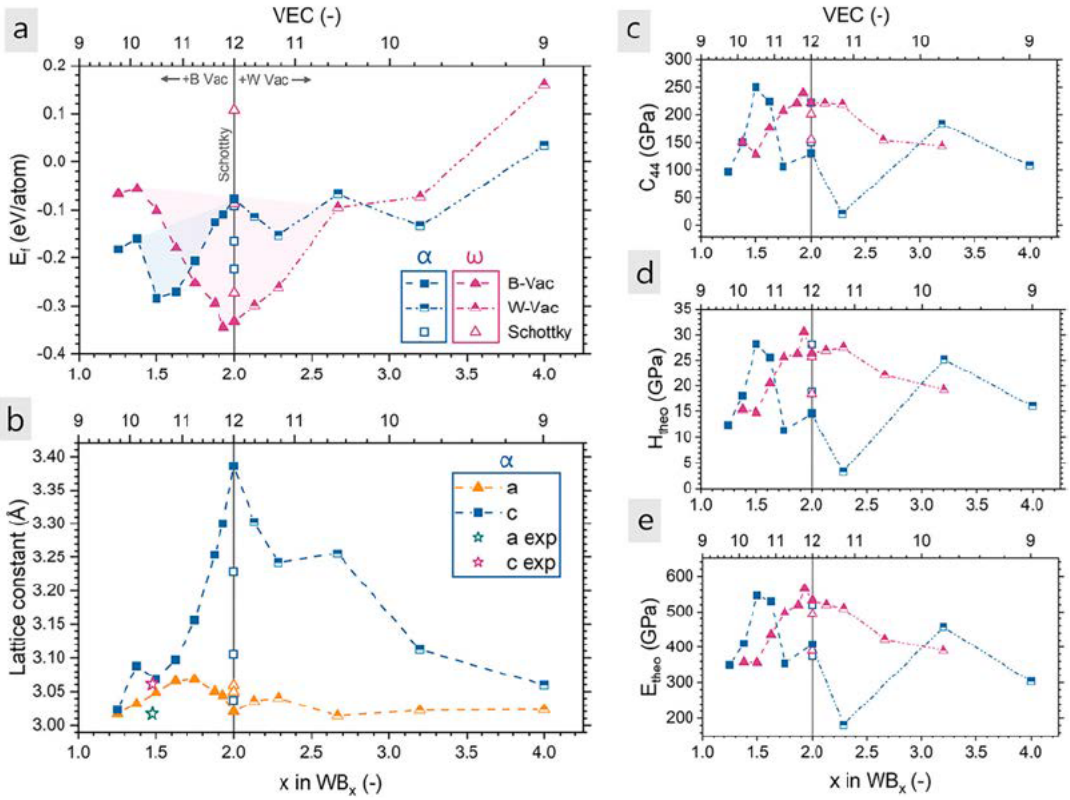

Figure 1. (a) E_f values of fully converged α-WB_x (2×2×4) and ω-WB_x (2×2×1) supercells (x = 1.25–4.0) as a function of chemical composition represented by the value of x = 2±z in WB_x. Figure 1b gives the evolution of lattice constant a (orange triangles), and c (blue squares) of α-WB_x. Additionally, the elastic constant C_{44} (c), the theoretical hardness H_{theo} (d), and the theoretical Young's modulus E_{theo} (e) of all mechanically stable structures are illustrated. The change in valence electron concentration (VEC) of defected WB_x crystals is depicted in the abscissa on top of Figure 1a–e.

squares for α, red empty triangles for ω), is indicated, respectively. The vertical grey line represents stoichiometric WB_2 expressing the value of x = 2.0 in WB_x. With increasing B vacancy population x is decreasing, while an increase of W vacancies leads to an increase of x (indicated on the bottom abscissa of Figure 1(a)). Moreover, an increasing vacancy concentration is decreasing the valence electron concentration (VEC) of the material system, highlighted on the top abscissa of Figure 1(a).

Generally, E_f raises by adding vacancies to the ω-lattice, having its minima around the perfect W_2B_4/WB_2 stoichiometry [9] and lowered with increasing number of vacancies within the α-lattice. The α-structured cell is thermodynamically preferred compared to ω—meaning E_f of α-WB_{2-z} is below ω-WB_{2-z}—at a vacancy concentration > 6%. Boron defected α- and ω-structured cells energetically intersect at $WB_{1.70}$ ($E_f = -0.23$ eV/at) followed by a thermodynamic minimum at $WB_{1.50}$ ($E_f = -0.28$ eV/at) for the α-lattice. The atomic concentration of the α-cell at the E_f minima leads to 40 at.% W and 60 at.% B, hence matching the experimentally measured compositions obtained by ICP-OES for various WB_{2-z} films deposited on the different routes (WB_2_01: W = 40.74 ± 0.91 at.%, B = 59.26 ± 0.91 at.%; WB_2_20: W = 39.14 ± 1.67 at.%, B = 60.86 ± 1.67 at.%; WB_2_21: W = 40.41 ± 2.04 at.%, B = 59.59 ± 2.04 at.%). Moreover, investigations on the evolution of α-$WB_{2\pm z}$ lattice constants revealed convergence of α-$WB_{1.5}$ (a = 3.0488 Å, b = 3.0483 Å, c = 3.0683 Å, V = 24.74 Å^3) during DFT calculations with our experimentally obtained values of $WB_{1.47}$ (a = 3.0168 Å, c = 3.0608 Å) using nanobeam diffraction on powdered coating material (stars in Figure 1(b))—for details see Supplementary. Due to correlating lattice parameters from our α-$WB_{1.47}$ with those reported from Woods et al. (a = b = 3.0200 Å, c = 3.0500 Å, V = 24.09 Å^3) [34], we would suggest a sub-stoichiometric composition also for their structure. In addition, Hayami et al. theoretically determined lattice constants for $WB_{1.625}$ of a = b = 3.072 Å, c = 3.117 Å [35].

All defected lattice configurations (considered in Figure 1(a)) have been consulted for calculating the stiffness tensor C. To ensure validity of the resulted elastic constants C_{ij}, the following criteria have to be fulfilled in hexagonal crystals: $C_{11} > |C_{12}|$; $2C_{13}^2 < C_{33} \cdot (C_{11} + C_{12})$; $C_{44} > 0$; $C_{66} > 0$. All data points presented in Figure 1(b–d) satisfy the above-mentioned stability conditions, thus revealing mechanically stable structures. For the quantification of mechanical stability of perfect and defected structures, the elastic constant C_{44} is highlighted in Figure 1(c). The data points reveal values of $C_{44} = 131$ GPa for stochiometric α as well as $C_{44} = 221$ GPa for ω, indicating enhanced mechanical stability for ω. This trend is inverted by introducing B vacancies to the crystal structures leading to a maximum $C_{44} = 250$ GPa at x = 1.5 and VEC = 10.5 for α structured $WB_{1.5}$. Moreover, the C_{44} maximum of the α-lattice is correlating with the E_f minima (Figure 1(a)), revealing highest thermodynamic stability is also leading to the highest mechanical stability of this crystal. Furthermore, theoretical hardness values, H_{theo}, have been evaluated using a widely established model [36], $H = 0.92 \cdot (G/B)^{1.137} \cdot G^{0.708}$, where G and B are shear- and bulk modulus, respectively. Figure 1(d) illustrates H_{theo}, showing a maximum value of $H_{theo} = 28$ GPa for α structured $WB_{1.5}$ and maximum $H_{theo} = 31$ GPa for ω-$WB_{1.93}$. The same trend was experienced for the theoretical Young's moduli ($E = 9 \cdot B \cdot G/(3B+G)$) with a maximum $E_{theo} = 546$ GPa for α structured $WB_{1.5}$ and $E_{theo} = 565$ GPa for ω-$WB_{1.93}$, as indicated in Figure 1(e).

Although the used target material is of ω-WB_2 structure, the deposition of ω-WB_2 coatings points out to be very challenging, since α-structured WB_{2-z} is preferentially formed within magnetron sputtering techniques (see XRD patterns in the Supplementary Material). The broad parameter variation on 3 different deposition systems revealed always sub-stoichiometric α-WB_{2-z} structured thin films but in various crystal orientations. The reason for the alpha stabilization is the high defect density especially on the non-metal sublattice (dislocations, vacancies) due to the extreme cooling rates during condensation from the vapour phase to the solid state. Furthermore, the difference in mass between light (B) and heavy (W) elements promotes scattering effects during sputtering leading to sub-stoichiometric compositions. A highly 0001 oriented α-WB_{2-z} coating ($WB_{1.45}$) has been investigated using TEM (see Figure 2). The coating exhibits a columnar and defected morphology, see Figure 2(a,b). Section 2a also represents the area for the recorded SAED pattern, depicted in the inset a-i. SAED exhibits highly oriented crystals in $[11\bar{2}0]$ zone axis. Additionally, the inset a-i contains a VESTA model [37] of the α-structured WB_2 unit cell—the W and B atoms are represented in red and blue, respectively—oriented as obtained from SAED. Figure 2(b) shows a high-resolution TEM image of the investigated coating, emphasizing defected zones within the highly-oriented crystal. However, the FFT image, depicted in section c, confirms the same crystal orientation as already revealed from SAED –masking regions for the Inverse Fast Fourier Transform (IFFT) are marked as white dashed circles. The sections d-f show filtered TEM images (for technical details see [38]) from the same region marked in b overlaid with a masked IFFT in the depicted directions ((1000), (0001), and $(10\bar{1}1)$ for d, e, and f respectively). Conducting this procedure, defect/strain-rich domains can be highlighted, confirming the structural stabilization in the α-phase of the chemically sub-stoichiometric $WB_{1.45}$ film. In correspondence to [13], structural defects (i.e. Boron vacancies) seem to compensate for the sub-stoichiometry of the coating.

In Figure 3(a) experimentally determined hardness H (blue open squares) and Young's modulus E (red open triangles) are plotted as a function of increasing fraction of 0001 lattice orientation of the various α-WB_{2-z} coatings. H is increasing from ~25 GPa for coatings without any 0001 orientation up to ~40 GPa for purely 0001 oriented coatings. Thus, the dataset reveals a linear dependency of H with an increasing 0001 ratio (see linear fit with 95% confidence limit in Figure 3(a)). On the other hand, the evaluation of the $10\bar{1}1$ ratio shows a contrary picture. Figure 3(b) depicts the experimentally determined H as a function of increasing $10\bar{1}1$ ratio (blue open squares), revealing a decrease of H with an increasing $10\bar{1}1$ orientation (blue dashed line and blue shaded area). These results point out the anisotropic mechanical property of α-WB_{2-z} coatings, revealing the highest hardness when 0001 oriented by simultaneously showing no $10\bar{1}1$ orientation. In comparison, the stochiometric α-structured WB_2 is predicted to obtain a $H_{theo} = 15$ GPa, whereas the boron defected α-$WB_{1.5}$ reveals $H_{theo} = 28$ GPa coinciding with the experimental data. Here, we need to point out that in H_{theo} neither anisotropic effects nor hardening due to a Hall-Petch effect is considered.

The observed anisotropy in hardness can be related to aggravated dislocation movement due to energetically less preferred slip systems. Through DFT, Hunter et al. [39] showed that various slip systems in hexagonal ZrB_2 (AlB_2 prototype, SG191, α) reveal different generalized stacking fault energies (GSFE). The $<a>$ type basal slip 0001 is the easiest a-type slip system to activate, energetically followed by pyramidal $<1\bar{2}10>10\bar{1}\bar{1}$ and both prismatic $<1120>10\bar{1}0$ slip systems. Additionally, the

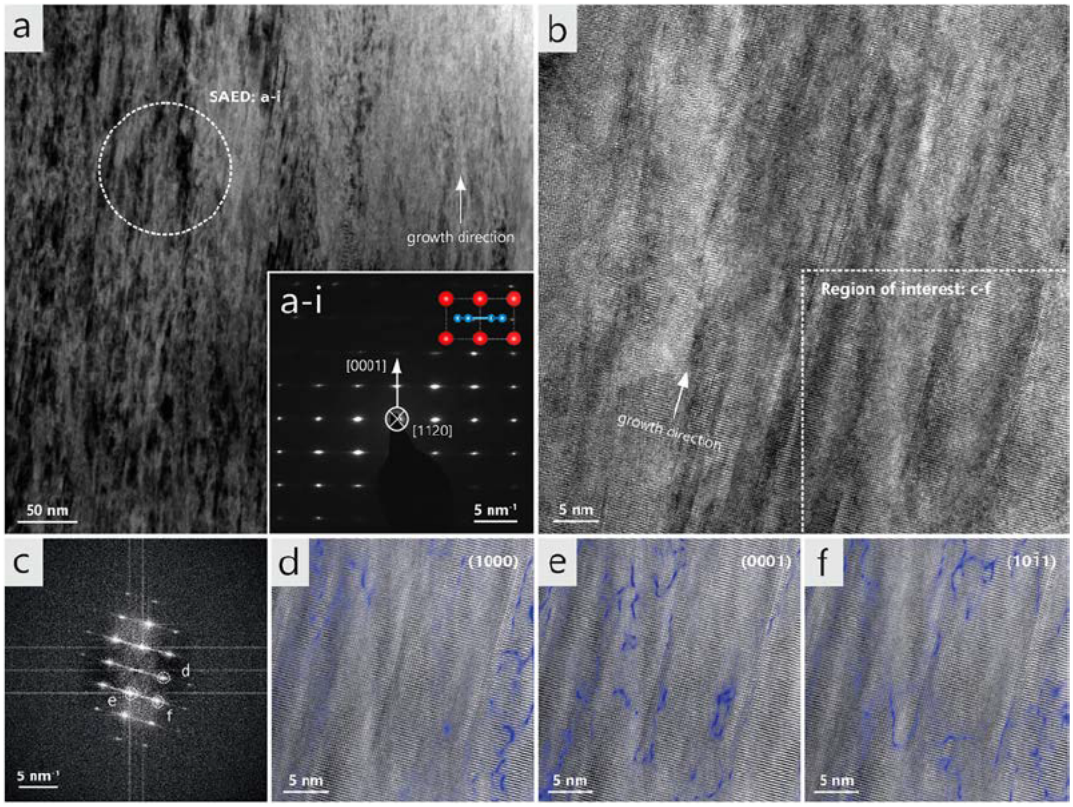

Figure 2. TEM analysis of the $WB_{1.45}$ coating. Section a presents a cross-sectional BF image of the $WB_{1.45}$ lamella, pointing out the area for the recorded SAED (white dashed circle) displayed in the inset a–i. An FFT cut out of the HR-TEM in b (region of interest) is depicted in section c, furthermore marking the masking regions for the IFFT as white dashed circles. Section d-f show defect/strain rich domains corresponding to the indicated directions (based on IFFT).

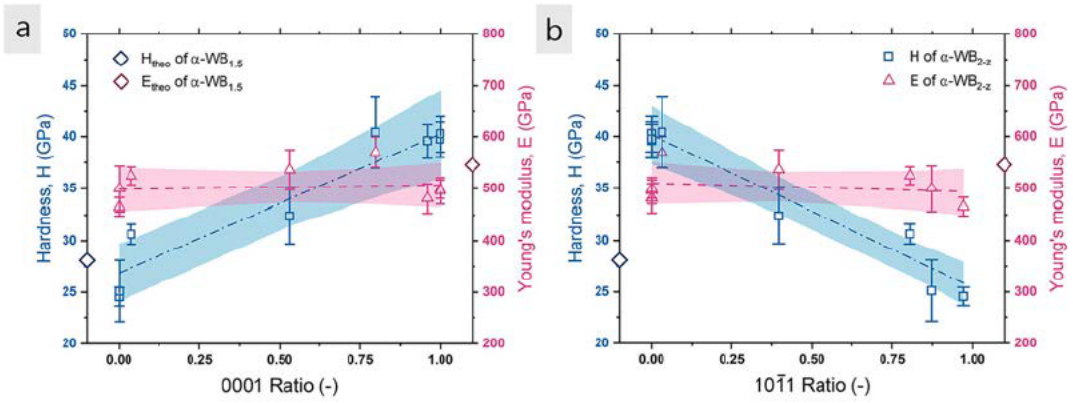

Figure 3. Hardness H (blue open squares) and Young's modulus E (red open triangles) of various α-WB_{2-z} thin films deposited. The dataset presents the mechanical properties as a function of the 0001 (a) and 10$\bar{1}$1 lattice plane (b) orientation factor, determined from XRD data (see Supplementary Material). The dashed lines give a linear fit from H (blue dashed line) and E (red dashed line). The blue and red shaded areas represent a 95% confidence limit.

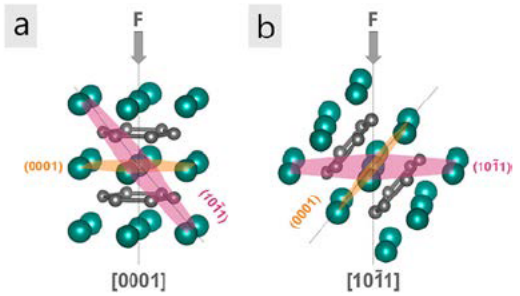

Figure 4. The hexagonal α-WB_2 structure is illustrated in 0001 (a) and 10$\bar{1}$1 (b) orientation. W and B atoms are depicted in green and grey, respectively. Indentation experiments leading to a normal force F (grey arrow) which is appearing perpendicular to the (0001) plane (a) (basal slip plane, orange area) or (10$\bar{1}$1) plane (b) (pyramidal slip plane, red area).

calculated GSFE values are correlating with interplanar spacing, meaning the closer the planes are spaced, the larger the GSFE value becomes. Due to structural correlations of α-ZrB_2 and α-WB_{2-z}, we can assume a similar behaviour for both hexagonal material systems. Thus, a hardness increase for [0001] crystals can be explained by a larger GSFE value of the pyramidal slip system (10$\bar{1}$1 slip plane)—compared to the basal slip system—which experiences the maximum shear stress τ_{max} when a force (during indentation) is applied in [0001] direction (see Figure 4(a)). However, for a 10$\bar{1}$1 crystal, the basal slip system (0001 slip plane) is preferentially activated due to τ_{max} appearing at a 45° angle to the force vector F (Schmid's law), directing in [10$\bar{1}$1] in this scenario (see Figure 4(b)).

In contrast to the hardness results, indentation experiments revealed relatively constant Young's moduli in the range of ~500 GPa, depicted in Figure 3(a,b). The data set emphasizes that the 0001 and 10$\bar{1}$1 crystal orientations have only a minor influence on E (depicted by the linear fit; red dashed line). For comparison, the DFT calculations exhibit a Young's modulus of 408 GPa for perfect α-WB_2 structured cells. Only after introducing B vacancies, the theoretical Young's modulus increases to $E_{theo} = 546$ GPa for α-$WB_{1.5}$ approaching the experimentally observed data. Moreover, by evaluating the spatial dependency of the Young's modulus of perfect α-WB_2 and defected α-$WB_{1.5}$ a clear decrease of the anisotropy for the α-$WB_{1.5}$ could be observed (see Figure S4 and S5 in the Appendix). The anisotropy reduces from 1.804 for α-WB_2 to 1.151 for α-$WB_{1.5}$ further underlining the presence of a highly defected structure within our WB_{2-z} thin films.

In addition to the anisotropy of the hardness, we also evaluated the fracture toughness of selected coatings to gain a deeper insight into a possible orientation-related fracture behaviour. Micromechanical cantilever bending experiments of selected α-WB_{2-z} coatings, revealed K_{IC} values ranging from 2.89 ± 0.26 MPa$\sqrt{m}$ ($WB_{1.45}$, 0001-ratio: 0.80), 3.23 ± 0.19 MPa$\sqrt{m}$ ($WB_{1.87}$, 0001-ratio: 0.99), to 3.65 ± 0.26 MPa$\sqrt{m}$ ($WB_{1.55}$, 0001-ratio: 0.04), revealing no perceptible influence of the film orientation (for further details see Table S4 in the Supplementary Material). The results indicate that the fracture toughness of our thin film materials is not affected by dislocation movement, hence other mechanisms govern the observed variation in K_{IC} values. Such mechanisms can be for example: the cohesive grain boundary strength (influenced by the growth conditions or the introduction of column boundary affine elements), introduction of third order residual stresses by i.e. precipitation toughening or unwanted impurities such as oxygen, or effects of the microstructure on the fracture behaviour.

Conclusion

In summary, the AlB_2 structure formation of $WB_{2\pm z}$ was investigated by DFT. The calculations indicate the stabilization of hexagonal α-WB_{2-z} by B vacancies, compared to a thermodynamic minimum of perfect, stoichiometric ω-WB_2. This theoretical result is experimentally underlined by: matching lattice parameters, mechanical properties, and chemical compositions of physical vapour deposited α-WB_{2-z} thin films. Moreover, nanoindentation of the synthesized coatings revealed anisotropy in the elastoplastic behaviour. Super-hardness was determined for 0001 oriented films, linearly decreasing by more than 15 GPa with an increasing 10$\bar{1}$1 orientation. Varieties in GSFE of basal and pyramidal slip systems in hexagonal crystals may constitute anisotropy in hardness. In contrast, no impact of the crystal orientation on K_{IC} could be detected.

Acknowledgement

We also thank for the financial support of Plansee SE, Plansee Composite Materials GmbH, and Oerlikon Balzers, Oerlikon Surface Solutions AG. In addition, we want to thank the X-ray centre (XRC) of TU Wien for beam time as well as the electron microscopy centre—USTEM TU Wien—for using the SEM and TEM facilities. The authors acknowledge TU Wien Bibliothek for financial support through its Open Access Funding Programme. The computational results presented have been achieved using the Vienna Scientific Cluster (VSC). We further acknowledge the granted use of the Nanofocus Endstation of the Beamline P03 of PETRA III at DESY, a member of the Helmholtz Association (HGF).

Disclosure statement

No potential conflict of interest was reported by the author(s).

Funding

The financial support by the Austrian Federal Ministry for Digital and Economic Affairs, the 10.13039/100007224 National Foundation for Research, Technology and Development and the Christian Doppler Research Association is gratefully acknowledged (Christian Doppler Laboratory 'Surface Engineering of high-performance Components').

ORCID

C. Fuger http://orcid.org/0000-0003-2685-4808
R. Hahn http://orcid.org/0000-0002-7322-8108
L. Zauner http://orcid.org/0000-0002-8373-6552
T. Wojcik http://orcid.org/0000-0001-5091-5215
M. Weiss http://orcid.org/0000-0002-4312-9256
A. Limbeck http://orcid.org/0000-0001-5042-2445
H. Riedl http://orcid.org/0000-0002-8108-1185

References

[1] Mitterer C. Borides in thin film technology. J Solid State Chem. 1997;133:279–291.
[2] Euchner H, Mayrhofer PH. Designing thin film materials — ternary borides from first principles. Thin Solid Films. 2015;583:46–49.
[3] Nagamatsu J, Nakagawa N, Muranaka T, et al. Superconductivity at 39 K in magnesium diboride. Nature. 2001;410:63–64.
[4] Magnuson M, Hultman L, Högberg H. Review of transition-metal diboride thin films. Vacuum. 2022;196:110567.
[5] Moraes V, Riedl H, Fuger C, et al. Ab initio inspired design of ternary boride thin films. Sci Rep. 2018;8:9288.
[6] Ivanovskii AL. Mechanical and electronic properties of diborides of transition 3d–5d metals from first principles: toward search of novel ultra-incompressible and superhard materials. Prog Mater Sci. 2012;57:184–228.
[7] Kiessling R. The binary system chromium-boron. Acta Chem Scand. 1949;3:949.
[8] Dorri MM, et al. Synthesis and characterization of CrB2 thin films grown by DC magnetron sputtering. Scr Mater. 2021;200:113915.
[9] Frotscher M, Klein W, Bauer J, et al. M2b5 or M2B4? A reinvestigation of the Mo/B and W/B system. Zeitschrift für Anorganische und Allgemeine Chemie. 2007;633:2626–2630.
[10] Fuger C, Moraes V, Hahn R, et al. Influence of Tantalum on phase stability and mechanical properties of WB2. MRS Commun. 2019;9:375–380.
[11] Euchner H, Mayrhofer PH, Riedl H, et al. Solid solution hardening of vacancy stabilized Ti W1−B2. Acta Mater. 2015;101:55–61.
[12] Liu YM, Jiang CL, Pei ZL, et al. Microstructure and properties of AlB2-type WB2 thin films deposited by direct-current magnetron sputtering. Surf Coat Technol. 2014;245:108–116.
[13] Palisaitis J, Dahlqvist M, Hall AJ, et al. Where is the unpaired transition metal in substoichiometric diboride line compounds? Acta Mater. 2021;204:116510.
[14] Orozco-Caballero A, Li F, Esqué-de los Ojos D, et al. On the ductility of alpha titanium: The effect of temperature and deformation mode. Acta Mater. 2018;149:1–10.
[15] Prasad KE, Ramesh KT. Hardness and mechanical anisotropy of hexagonal SiC single crystal polytypes. J Alloys Compd. 2019;770:158–165.
[16] Jian S-R. Berkovich indentation-induced deformation behaviors of GaN thin films observed using cathodoluminescence and cross-sectional transmission electron microscopy. Appl Surf Sci. 2008;254:6749–6753.
[17] Huang J, Xu K, Fan YM, et al. Nanoscale anisotropic plastic deformation in single crystal GaN. Nanoscale Res Lett. 2012;7:1–4.
[18] Kishida K, Shinkai Y, Inui H. Room temperature deformation of 6H–SiC single crystals investigated by micropillar compression. Acta Mater. 2020;187:19–28.
[19] Niihara K. Slip systems and plastic deformation of silicon carbide single crystals at high temperatures. J Less Common Metals. 1979;65:155–166.
[20] Hahn R, Moraes V, Limbeck A, et al. Electron-configuration stabilized (W,Al)B2 solid solutions. Acta Mater. 2019;174:398–405.
[21] Moraes V, Fuger C, Paneta V, et al. Substoichiometry and tantalum dependent thermal stability of α-structured W-Ta-B thin films. Scr Mater. 2018;155:5–10.
[22] Fuger C, Schwartz B, Wojcik T, et al. Influence of Ta on the oxidation resistance of WB2−z coatings. J Alloys Compd. 2021;864:158121.
[23] Kresse G, Joubert D. From ultrasoft pseudopotentials to the projector augmented-wave method. Phys Rev B. 1999;59:1758–1775.
[24] Kresse G, Furthmüller J. Efficient iterative schemes for *ab initio* total-energy calculations using a plane-wave basis set. Phys Rev B. 1996;54:11169–11186.
[25] Perdew JP, Burke K, Ernzerhof M. Generalized gradient approximation made simple. Phys Rev Lett. 1996;77:3865–3868.
[26] Yu R, Zhu J, Ye HQ. Calculations of single-crystal elastic constants made simple. Comput Phys Commun. 2010;181:671–675.
[27] Fischer-Cripps AC. Critical review of analysis and interpretation of nanoindentation test data. Surf Coat Technol. 2006;200:4153–4165.
[28] Cakara A, Bonta M, Riedl H, et al. Development of a multi-variate calibration approach for quantitative analysis of oxidation resistant Mo–Si–B coatings using laser ablation inductively coupled plasma mass spectrometry. Spectrochim Acta Part B. 2016;120:57–62.
[29] Riedl H, Vieweg A, Limbeck A, et al. Thermal stability and mechanical properties of boron enhanced Mo–Si coatings. Surf Coat Technol. 2015;280:282–290.
[30] Bonta M, Frank J, Taibl S, et al. Online-LASIL: laser ablation of solid samples in liquid with online-coupled ICP-OES detection for direct determination of the stoichiometry of complex metal oxide thin layers. Anal Chim Acta. 2018;1000:93–99.
[31] Aschauer E, Riedl H, Koller CM, et al. Adhesive wear formation on PVD coated tools applied in hot forming of Al-Si coated steel sheets. Wear. 2019;430-431:309–316.
[32] Bartosik M, Hahn R, Zhang ZL, et al. Fracture toughness of Ti-Si-N thin films. Int J Refract Met Hard Mater. 2018;72:78–82.
[33] Matoy K, Schönherr H, Detzel T, et al. A comparative micro-cantilever study of the mechanical behavior of silicon based passivation films. Thin Solid Films. 2009;518:247–256.

[34] Woods HP, Wawner FE, Fox BG. Tungsten diboride: preparation and structure. Science. 1966;151:75.
[35] Hayami W, Momozawa A, Otani S. Effect of defects in the formation of AlB_2 -type WB_2 and MoB_2. Inorg Chem. 2013;52:7573–7577.
[36] Tian Y, Xu B, Zhao Z. Microscopic theory of hardness and design of novel superhard crystals. Int J Refract Met Hard Mater. 2012;33:93–106.
[37] Momma K, Izumi F. VESTA 3 for three-dimensional visualization of crystal, volumetric and morphology data. J Appl Crystallogr. 2011;44:1272–1276.
[38] Kilaas R. Optimal and near-optimal filters in high-resolution electron microscopy. J Microsc. 1998;190:45–51.
[39] Hunter B, Yu X-X, De Leon N, et al. Investigations into the slip behavior of zirconium diboride. J Mater Res. 2016;31:2749–2756.

Publication II

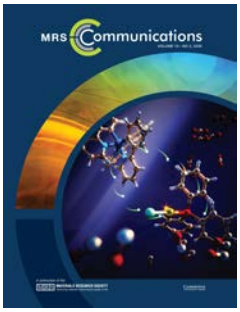

Influence of Tantalum on phase stability and mechanical properties of WB_2

C. Fuger, V. Moraes, R. Hahn, H. Bolvardi, P. Polcik, H. Riedl, and P.H. Mayrhofer

MRS Communications (2019), 9, 375–380
doi: 10.1557/mrc.2019.5

citations (Google Scholar, April 19, 2022): 21

Publication III

Influence of Ta on the oxidation resistance of WB_{2-z} coatings

C. Fuger, B. Schwartz, T. Wojcik, V. Moraes, M. Weiss, A. Limbeck, C.A. Macauley, O. Hunold, P. Polcik, D. Primetzhofer, P. Felfer, P.H. Mayrhofer, and H. Riedl

Journal of Alloys and Compounds (2021), 864, 158121
doi: 10.1016/j.jallcom.2020.158121

citations (Google Scholar, April 19, 2022): 10

Journal of Alloys and Compounds 864 (2021) 158121

Contents lists available at ScienceDirect

Journal of Alloys and Compounds

journal homepage: www.elsevier.com/locate/jalcom

Influence of Ta on the oxidation resistance of WB_{2-z} coatings

C. Fuger[a,*], B. Schwartz[a], T. Wojcik[a,b], V. Moraes[b], M. Weiss[c], A. Limbeck[c], C.A. Macauley[d,e], O. Hunold[f], P. Polcik[g], D. Primetzhofer[h], P. Felfer[d], P.H. Mayrhofer[b], H. Riedl[a,b]

[a] Christian Doppler Laboratory for Surface Engineering of high-performance Components, TU Wien, Austria
[b] Institute of Materials Science and Technology, TU Wien, A-1060 Wien, Austria
[c] Institute of Chemical Technologies and Analytics, TU Wien, Vienna, Austria
[d] Department of Materials Science, Friedrich-Alexander-Universität Erlangen-Nürnberg, Germany
[e] Interdisciplinary Center for Nanostructured Films (IZNF), 91058 Erlangen, Germany
[f] Oerlikon Balzers, Oerlikon Surface Solutions AG, 9496 Balzers, Liechtenstein
[g] Plansee Composite Materials GmbH, D-86983 Lechbruck am See, Germany
[h] Department of Physics and Astronomy, Uppsala University, SE-75120 Uppsala, Sweden

ARTICLE INFO

Article history:
Received 18 September 2020
Received in revised form 22 November 2020
Accepted 24 November 2020
Available online 26 November 2020

Keywords:
Oxidation resistance
Transition metal diborides
Scale growth
Diborides

ABSTRACT

Ternary $W_{1-x}Ta_xB_{2-z}$ is a promising protective coating material possessing enhanced ductile character and phase stability compared to closely related binaries. Here, the oxidation resistance of $W_{1-x}Ta_xB_{2-z}$ thin films was experimentally investigated at temperatures up to 700 °C. Ta alloying in sputter deposited WB_{2-z} coatings led to decelerated oxide scale growth and a changed growth mode from paralinear to a more linear (but retarded) behavior with increasing Ta content. The corresponding rate constants decrease from $k_p^* = 6.3 \cdot 10^{-4}$ µm²/s for WB_{2-z}, to $k_p^* = 1.1 \cdot 10^{-4}$ µm²/s for $W_{0.66}Ta_{0.34}B_{2-z}$ as well as $k_l = 2.6 \cdot 10^{-5}$ µm/s for TaB_{2-z}, underlined by decreasing scale thicknesses ranging from 1170 nm (WB_{2-z}), over 610 nm ($W_{0.66}Ta_{0.34}B_{2-z}$) to 320 nm (TaB_{2-z}) after 10 min at 700 °C. Dense and adherent scales exh bit an increased tantalum content (columnar oxides), which suppresses the volatile character of tungsten-rich as well as boron oxides, hence being a key-factor for enhanced oxidation resistance. Thus, adding Ta (in the range of x = 0.2–0.3) to α-structured WB_{2-z} does not only positively influence the ductile character and thermal stability but also drastically increases the oxidation resistance.

1. Introduction

Various industrial applications, e.g. in aerospace industry, aviation, or energy production, demand complex applied materials requirements to increase lifetime and thus, enhance environmental sustainability. Since bulk materials occasionally cannot fulfill all these demands, surface engineering using physical vapor deposition (PVD) deposited thin films is a well-established method enhancing specific properties. Based on the most common applications, transition metal ceramics, particularly transition metal nitrides such as TiN, CrN, or $Ti_{1-x}Al_xN$ have been explored in depth over decades [1–3]. However, the material class of borides is a valuable alternative in new applications. Especially, transition metal borides (TMBs) exhibit a tremendous potential to be applied in various fields ranging from wear and corrosion resistant coatings, to superconductive thin films, or as superhard and extremely stable protective layers in diverse engineering applications [4–6]. One very interesting representative of the TMBs is tungsten diboride, which exhibits specific mechanical properties with respect to the generally limited fracture tolerance of such ceramic compounds [7–9]. Previous studies on diborides revealed that transition metal diborides tend to crystalize in two different hexagonal structures, α- (AlB_2, space group 191, P6/mmm) and ω-prototype (W_2B_{5-x}, space group 194, $P6_3/mmc$), respectively [10,11]. By synthesizing WB_{2-z} coatings using PVD techniques, the films crystallize in the metastable α-phase rather than in the thermodynamically preferred ω-structure. As structural defects play a crucial role in the stabilization of α-structured WB_{2-z}, the impact on the mechanical properties, especially fracture resistance, is still not fully described. However, in theoretical as well as experimental investigations (by free-standing cantilever tests), α-WB_{2-z} exhibits a highly ductile behavior with K_{IC} values of around 3.7 ± 0.3 MPa√m. In comparison, ZrB_{2-z} and $Zr_{1-x}Ta_xB_{2-z}$ films obtain values around from 3.5 to 5.5 MPa√m during cube corner indentation, which typically overestimates fracture characteristics (compared to cantilever bending) by at least

* Corresponding author.
E-mail address: christoph.fuger@tuwien.ac.at (C. Fuger).

https://doi.org/10.1016/j.jallcom.2020.158121
0925-8388/

2.0 MPa√m [12–14]. However, one weak point of α-structured WB_{2-z} is the thermal stability, as the decomposition to its stable ω-modification sets in relatively early – at around 800 °C. Furthermore, in addition to the limited phase stability in inert atmospheres, the formation of volatile tungsten oxides occurs at even lower temperatures and thus strongly limits the wide usage of α-structured WB_{2-z} [15–17]. With respect to phase transition between α and ω, the addition of Ta has been proven to shift the starting point for decomposition to increased temperatures. The resulting ternary $W_{1-x}Ta_xB_{2-z}$ with x ~ 0.25 leads to an enhancement of the decomposition temperature (in inert atmosphere) by 600 °C to a maximum of T_{dec} = 1400 °C [18]. Small additions of Ta also slightly enhance the fracture toughness to 3.8 ± 0.5 MPa√m at x ~ 0.15, while obtaining hardness values above 40 GPa [12,18]. All these points suggest $W_{1-x}Ta_xB_{2-z}$ as a promising protective coating system. However, a clear study of the influence of Ta on the oxidation resistance is still missing to complete the profile of properties.

Therefore, based on the above-mentioned results, the focus of this study is to investigate in detail the influence of Ta on the oxidation resistance of sputter deposited $W_{1-x}Ta_xB_{2-z}$ thin films.

2. Experimental

All WB_{2-z}, $W_{1-x}Ta_xB_{2-z}$, and TaB_{2-z} coatings were deposited by DC magnetron sputtering using an in-house developed deposition system with two confocal arranged cathodes, for details see [19]. The ultra-high vacuum coating facility was equipped with two 6-inch – TaB_2 and W_2B_5 – powder-metallurgically produced targets obtaining a purity of at least 99.6% (Plansee Composite Materials GmbH). Prior to the depositions, the silicon (20 × 7 × 0.33 mm^3, 100-oriented) and single crystalline sapphire (10 × 10 × 0.5 mm^3, 012-oriented) substrates were ultrasonically pre-cleaned in acetone and ethanol for 5 min each. Subsequently, they were mounted on a rotating substrate holder, and heated up in the chamber (base pressure below $4 \cdot 10^{-4}$ Pa) to the deposition temperature, T_{dep}, of 500 °C (corresponding to 300 ± 15 °C on the substrate surface) for at least 20 min. Furthermore, the substrates were etched in argon atmosphere (p_{etch} = 6 Pa) for 10 min applying a substrate potential of −500 V. The deposition process itself was carried out in pure argon atmosphere at a deposition pressure of 0.4 Pa. Both targets were powered by a Solvix HIP^3 generator – used in DC mode – controlling the applied target current, I_{target}, of maximum 4.2 A in total for both cathodes. To vary the chemical composition of the deposited films (dividing the full compositional range in steps of about x ~ 0.20) the applied current was changed successively for both target materials. The deposition time was varied between 60 and 85 min due to a decreased sputter rate for TaB_2 with respect to W_2B_5. To gain homogeneous compositions over all substrates, the substrate holder was rotated with a frequency, f_{rot}, of 0.25 Hz. The film growth was also supported by applying a bias potential of −50 V.

All oxidation tests were carried out in a standard chamber furnace in ambient air. To gain relatively flat and defined oxide scales, all oxidation tests have been performed on sapphire substrates. The kinetic behavior of the oxide scale formation was analyzed through varying the exposure time (t_{ox} = 1, 10, 100, and 1000 min) and temperature (T_{ox} = 500, 600, and 700 °C), respectively. The temperatures and time periods were selected based on oxidation pretests. In detail, all compositions have been fully oxidized after 1000 min at 700 °C and therefore the oxidation temperature was not further increased. After quantifying the oxide scale thicknesses by means of scanning electron microscopy (SEM) investigations (FEI Quanta 200 FEG-SEM) within fracture cross-sections, the oxidation rate constants were calculated by linear regression of squared oxide thickness values as a function of oxidation time.

As a proper chemical quantification of light elements in combination with heavy ones e.g. $W_{1-x}Ta_xB_{2-z}$, presents a certain challenge [18], different chemical analysis methods were utilized to obtain best results. The elemental composition of all as deposited thin films on Si substrates was analyzed by liquid inductively coupled plasma optical emission spectroscopy (ICP-OES). Liquid ICP-OES measurements were carried out on an iCAP 6500 RAD (Thermo Fisher Scientific, USA), with an ASX-520 autosampler (CETAC Technologies, USA) using a HF resistant sample introduction kit, consisting of a Miramist nebulizer (Burger Research, USA), a PTFE spray chamber and a ceramic injector tube. All $W_{1-x}Ta_xB_{2-z}$ coatings were acid digested with the method presented and validated in [20]. Samples were broken into pieces of about 3 × 3 mm^2 and the thin film with the substrate was dissolved in a mixture of 1 mL HNO_3 and 0.25 mL HF. After a reaction time of 15 min at a temperature of 60 °C, the thin films including the substrates were completely dissolved. Derived sample digests were diluted to a final volume of 20 mL with a mixture of 3% HNO_3 and 0.3% HF. Quantification was done via external calibration using matrix adjusted standards - for further details see also [20–22].

For a 3D elemental distribution, a selected coating in the as deposited state was analyzed by atom probe tomography (APT). The APT analysis was carried out on a CAMECA LEAP 4000X HR in pulsed laser mode. This instrument is equipped with a 355 nm UV laser with a spot size of ~2 µm and a reflectron lens resulting in a detection efficiency of ~37%. The experiments were done with a laser pulse energy of 50 pJ at a target evaporation rate of 1%. The as-deposited samples were extracted using a keyhole technique [23], which places the analysis axis in the growth direction of the film. Moreover, the composition of selected as deposited samples as well as compositional depth profiles of the oxide layers were obtained by time of flight elastic recoil detection analysis (TOF-ERDA) using a 36 MeV I^{8+} ion beam and detecting recoils in a detection angle of 45° with respect to the primary beam. Details on the employed detection system can be found in Ström et al. [24]. The expected systematic uncertainties for light elements such as B are found on a level of ± 1 at% for relative measurements free from standards, mainly due to uncertainties in the specific energy loss of the recoiling particles. For absolute measurements (free from standards), systematic uncertainties for light elements (e.g. B or C) are expected to be on a level of 5–10% of the detected concentration. A detailed description of sources and consequences of systematic uncertainties are discussed in more detail by Arvizu et al. [25] and Zhang et al. [26]. Depth profiles were established using the CONTES software package [27].

The coating morphology – before and after oxidation – was analyzed in cross sectional view by a FEI Quanta 250 FEG-SEM, equipped with a field emission gun (acceleration voltage used, 10 kV). In addition, the chemical composition of the formed scales and unaffected coatings was analyzed by energy dispersive X-Ray spectroscopy (EDAX EDS detector, 15 kV acceleration voltage). Selected samples were also surveyed in cross sectional view by transmission electron microscopy (TEM FEI TECNAI, G20, acceleration voltage of 200 kV). Detailed structural information of the formed oxide scales was gained by selected area electron diffraction (SAED) analysis. The sample preparation was done by focused ion beam (FIB, Quanta 200 3D Dual Beam), applying standard lift out techniques [28].

3. Results and discussion

3.1. Chemical composition and phase constitution as deposited

After sputter depositing the films, the chemical compositions of all coatings have been analyzed by ICP-OES. Fig. 1 shows the boron content (in at%) of all deposited coatings as a function of the Ta fraction at the metal sublattice, x. The blue, half-filled triangles are indicating the chemical compositions of the films synthesized

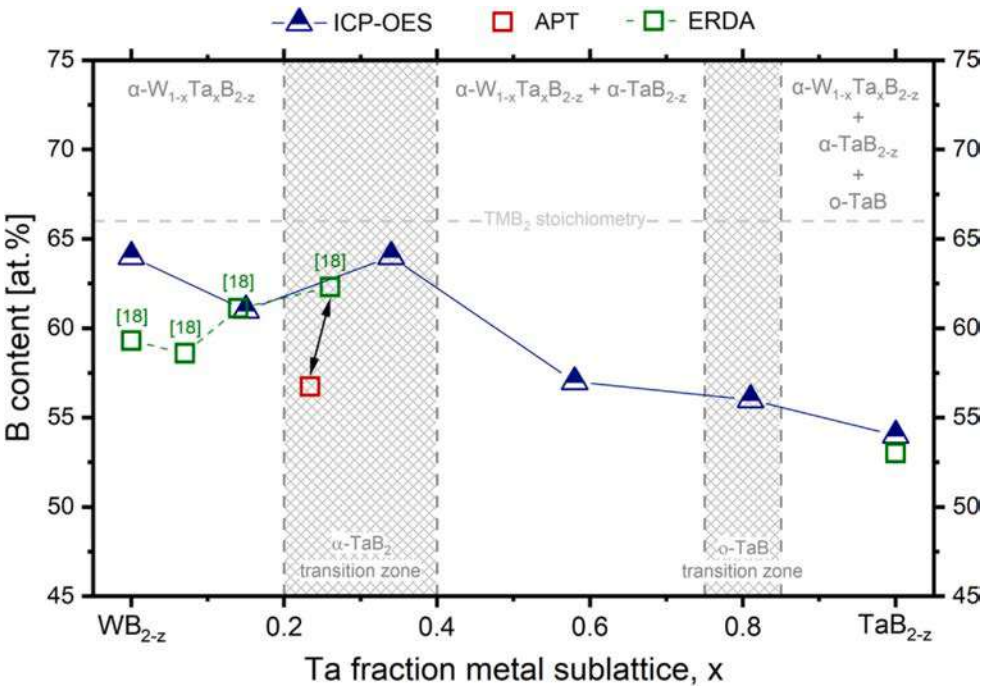

Fig. 1. Chemical composition obtained by ICP-OES of all coatings deposited within this study (blue data points). The green data points indicate the chemical composition evaluated by TOF-ERDA of $W_{1-x}Ta_xB_{2-z}$ thin films taken from [18] – except TaB_{2-z} which was analyzed within this study. During APT the overall elemental concentration of the inspected tip was evaluated and is indicated in red. (For interpretation of the references to colour in this figure legend, the reader is referred to the web version of this article.)

within this study, while the green open squares are highlighting the elemental fraction of $W_{1-x}Ta_xB_{2-z}$ coatings (obtained by TOF-ERDA) prepared in a previous study [18]. For a further comparison between different analysis techniques as well as quality and reproducibility of the depositions, the average W, Ta (in terms of metal sublattice occupation, x) and B concentration of a surveyed atom probe tip is also given in Fig. 1, see red open square (selected coating originates from study [18] – analyzed volume is depicted in Fig. 2). Both studies (blue and green data set refer to this study and Ref. [18]) exhibit the similar tendency of decreasing boron content with increasing amount of tantalum, highlighting the strong affinity to form either sub-stoichiometric structures with boron and/or Schottky defects as well as multi-phased coatings. Nevertheless, the decreasing B contents with increasing Ta are a strong indication, that the phase formation of α-structured $W_{1-x}Ta_xB_{2-z}$ films at high Ta fractions is limited and directed towards dual phase structures (α-$W_{1-x}Ta_xB_{2-z}$ + α-TaB_{2-z} or an orthorhombic o-TaB phase) – as also suggested in [12]. By considering all chemical and structural data (X-Ray diffraction [XRD] pattern for the full compositional range are presented in the Appendix), we can assume that there is a more or less ideal solid solution of α-$W_{1-x}Ta_xB_{2-z}$ up to about x = 0.20 (on the metal sublattice) and dual phased morphologies containing α-$W_{1-x}Ta_xB_{2-z}$ as well as α-TaB_{2-z} rich domains at Ta concentrations x > 0.40. Furthermore, at Ta x > 0.85 an additional o-TaB phase is occurring. The gray shaded areas between x = 0.20–0.40 as well as 0.75–0.85 exhibit the transition zones of upcoming TaB_2/TaB rich domains and the change between α-dominated structures and the additional appearance of a o-TaB phase, respectively.

To reveal a more detailed picture about the 3D atomic composition in the so-called α-TaB_2 transition zone (x ≥ 0.26, Ta submetal occupation), a detailed ATP analysis of the $W_{0.74}Ta_{0.26}B_{1.89}$ (given composition obtained by TOF-ERDA) coating was conducted (see Fig. 2a). The inhomogeneous distribution of tantalum in the growth direction, is shown clearly in the one-dimensional concentration profile (see Fig. 2b). Both, Ta and W show an inversely oscillating

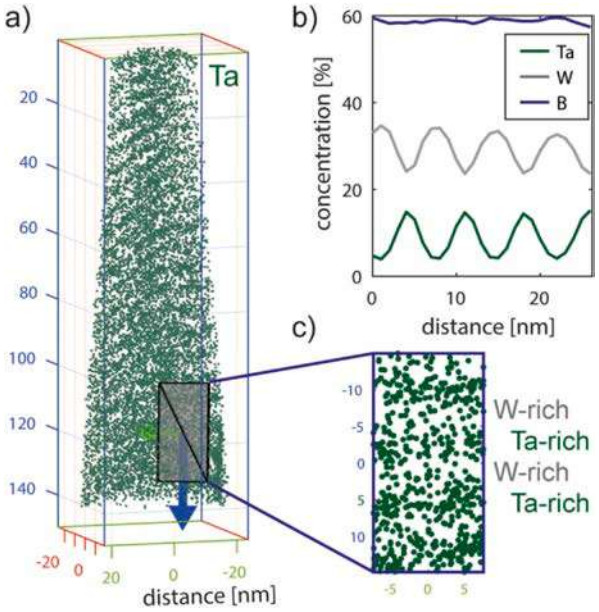

Fig. 2. Elemental distribution of Ta obtained by atom probe tomography of $W_{0.74}Ta_{0.26}B_{2-z}$ coating (a), showing a horizontally layered structure also confirmed by the one-dimensional concentration profile, depicted in (b). The layered structure is characterized by an alternating W/Ta content, highlighted by the image detail (c).

concentration going from ~5 at% to ~15 at% for Ta (x = 0.12–0.37 Ta occupation on the metal sublattice) and from ~35 at% to ~25 at% for W (x = 0.88–0.63 W sublattice occupation). This behavior could be due to, (i) a limited solubility of Ta in the α-$W_{1-x}Ta_xB_{2-z}$ structure, indicating the occurrence of a Ta rich phase and/or (ii) a synthesis related effect through the experimental setup of co-sputtering a

WB_{2-z} and TaB_{2-z} targets, respectively. By taking into account the rotational frequency of the substrate holder (0.25 Hz) and the deposition rate of both binary systems (~70 nm/min for WB_{2-z} compared to ~ 50 nm/min for TaB_{2-z}) result in an overall deposition rate of ~ 5 nm/s, which fits to the periodicity in Fig. 2b. Assuming that the substrate holder is not fully covered from both, the WB_{2-z} and TaB_{2-z} sputter plumes, there are areas with increased WB_{2-z}/TaB_{2-z} concentration, dependent on the progress of rotation. Therefore, the layered structure, depicted in Fig. 2, is suggested to be an unintended variation caused by the co-sputtering process [29]. Nevertheless, a limited solubility of Ta in the α-$W_{1-x}Ta_xB_{2-z}$ structure cannot be ruled out, as the W-depleted sections reveal x ~ 0.37 Ta on the metal sublattice (overall ~15 at% Ta). A more detailed view of the alternating W/Ta rich sections is also given in the cutout, depicted in Fig. 2c. Due to reasons of clarity, W atoms are not visualized in Fig. 2. These detailed analyses are also in good agreement with the diffraction results, which suggests that samples in the α-TaB_2 transition zone ($x \geq 0.26$) form imperfect as-deposited solid solutions when deposited using co-sputtering. Nevertheless, the occurrence of multi-phased coatings containing α-$W_{1-x}Ta_xB_{2-z}$, α-TaB_{2-z}, as well as o-TaB is mostly related to a lack of boron and the high tendency to form stoichiometric o-TaB. (please place Figure 2 here)

Nevertheless, a well-known deviation regarding the boron content of APT, TOF-ERDA and ICP-OES evaluated samples is also visible within this study – especially, depicted by the green (TOF-ERDA) and red square (APT), indicating a thin film from the same deposition run. To obtain comparable values, impurities like H, C, O, N and Ga have been subtracted from the total concentration of the APT tip, as all these elements together have been less than 2 at%. Here, we need to mention that the analyzed volume during APT is way smaller compared to the other analysis techniques. Nonetheless, the data sets from all utilized analysis techniques clearly reveal that the detection of an absolute boron concentration is difficult and only comparable when originating from the same technique/set-up as highlighted by [30,31]. However, the amount of W and Ta atoms shows almost perfect coincidence between APT and TOF-ERDA. To simplify notations, we therefore used TMB_{2-z} within the manuscript (always normalized to the metal sublattice).

3.2. Oxide scale formation

As a constant film thickness is crucial for a clear comparison during oxidation tests, the deposition times were adapted (from 60 to 85 min with increasing Ta) to grow films between 3.5 and 4.0 µm for all compositions. Cross sectional micrographs obtained with SEM, revealed very dense and smooth morphologies for all coatings in the as deposited state (on Si substrate) – see Fig. 3a-i for WB_{2-z}, 3b-i for $W_{0.42}Ta_{0.58}B_{2-z}$, and 3c-I for TaB_{2-z}, respectively. In contrast to our previous study, showing a more pronounced columnar growth morphology, the coatings exhibited a rather fine-grained to amorphous, nearly featureless structure. This is mainly attributed to the decreased deposition temperature used, T_{dep} = 500 °C compared to T_{dep} = 700 °C in [12].

In addition to the as deposited state, the corresponding cross-sectional micrographs after 100 min at 600 °C (3a-ii, 3b-ii, and 3c-ii) as well as 100 min at 700 °C (3a-iii, 3b-iii, and 3c-iii) oxidation are also presented. The coatings show stable oxide growth after 100 min at 600 °C and a decreased scale thickness with increasing Ta content (see Fig. 3-ii). However, after 100 min at T_{ox} = 700 °C all coatings reveal extensive oxide scales suggesting imminent break-through oxidation, which is also underlined by the presence of lateral cracks (see Fig. 3c-iii). Beyond t_{ox} = 100 min at T_{ox} = 700 °C all coatings start to spall off, and therefore no 1000-min oxidation tests at that temperature have been conducted. However, all scale thicknesses as well as scale morphologies were visually and analytically inspected by cross sectional SEM investigations.

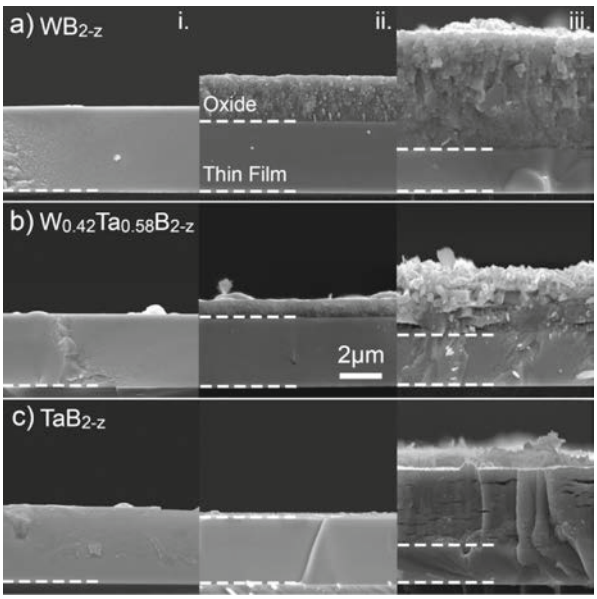

Fig. 3. Cross sectional micrographs of (a) WB_{2-z}, (b) $W_{0.42}Ta_{0.58}B_{2-z}$ and (c) TaB_{2-z}. Sections (a) – (c) show selected coatings in (i) as deposited state, (ii) after 100 min of oxidation at 600 °C and (iii) after 100 min of oxidation at 700 °C. The dashed lines are highlighting the interface between substrate and thin film as well as between thin film and oxide scale (from bottom to top).

The oxide scale thicknesses in relation to the oxidation times are summarized exemplarily for all compositions oxidized at T_{ox} = 600 °C – see Fig. 4a. In general, the results clearly reveal decreasing oxide thickness with increasing Ta content – i.e. by comparing WB_{2-z} to TaB_{2-z}. The scale thickness significantly decreases from 8.0 µm for WB_{2-z} compared to 1.6 µm for TaB_{2-z} after t_{ox} = 1000 min. Furthermore, the growth mode changes from a more paralinear behavior for W-rich coatings to a more linear mode with increasing Ta content. This is in good agreement with the pure metals, as described by Kubaschewski and Hopkins [32]. Nevertheless, the more linear growth mode for the Ta-rich coatings seems to be retarded – which could to be related to the morphology and density of the formed oxide – compared to the paralinear behavior for WB_{2-z} rich coatings. Unfortunately, there is no datapoint for the $W_{0.19}Ta_{0.81}B_{2-z}$ coating (purple diamond) after 1000 min at T_{ox} = 600 °C of oxidation because of spallation (see purple diamonds in Fig. 4a).

3.3. Oxidation kinetics

To gain further information about the oxidation kinetics, the rate constants k_p^* (for paralinear scale growth dominated by bulk and grain boundary diffusion – also called "Regime 2″) and k_l (for linear rate law dominated by surface reaction of oxygen – so called "Regime 1″) were calculated according to the procedure described in [33]. The calculations yield to an oxidation rate constant of $k_p^* = 6.3 \cdot 10^{-4}$ µm²/s (oxidation is following a paralinear growth mode) for WB_{2-z} (full squares) which is decreasing to $k_l = 2.6 \cdot 10^{-5}$ µm/s (linear oxidation growth mode, but one order of magnitude lower) for TaB_{2-z} (full stars). Coatings with a Ta content of x = 0.34–0.58 show a similar oxidation behavior, resulting in k_p^* values of around $1.1 \cdot 10^{-4}$ µm²/s. Based on this dataset, the oxidation kinetics of $W_{0.19}Ta_{0.81}B_{2-z}$ is suggested to be similar. The subsections (b–d) of Fig. 4 depict the oxidation behavior of pure WB_{2-z}, $W_{0.42}Ta_{0.58}B_{2-z}$ and pure TaB_{2-z}, respectively, at T_{ox} of 500, 600, and 700 °C. The oxide scales increase drastically for T_{ox} = 700 °C already

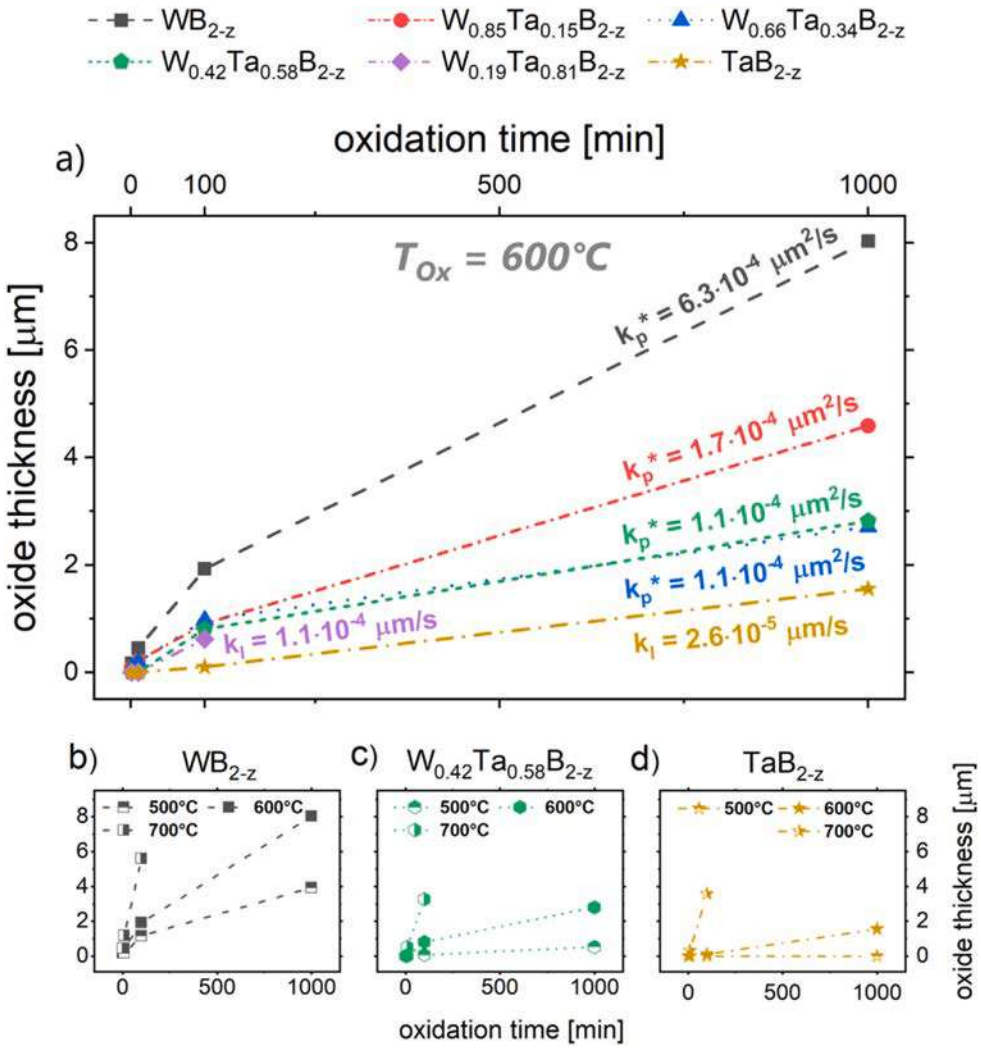

Fig. 4. Oxide thickness as a function of oxidation time for (a) 600 °C, of all coatings deposited. The oxidation rate constants k_p (parabolic or paralinear growth mode) and k_l (linear growth mode) are depicted in section (a) indicated by individual symbols representing different coating compositions (see legend). Furthermore, the oxidation behavior of (b) WB_{2-z}, (c) $W_{0.42}Ta_{0.58}B_{2-z}$ and (d) TaB_{2-z} for 500, 600, and 700 °C oxidation temperature is represented. (For interpretation of the references to colour in this figure legend, the reader is referred to the web version of this article.)

after t_{ox} = 100 min, leading to lateral cracks (see Fig. 3c-iii) and moreover, to non-adherent scales. The abovementioned gradients in chemical composition due to co-sputtering may lead to this behavior, but also stress relief due to oxide scale formation in general can be a possible scenario. However, increased Ta contents clearly retard the oxide scale formation.

3.4. Oxide scale morphology

For a more detailed view on the oxide scale morphology and structure, TEM investigations of WB_{2-z}, $W_{0.66}Ta_{0.34}B_{2-z}$, and TaB_{2-z} after oxidizing at 700 °C for 10 min have been conducted. The results for α-WB_{2-z}, α-$W_{0.66}Ta_{0.34}B_{2-z}$, as well as multi-phased α-TaB_{2-z} + o-TaB are presented in Figs. 5–7, respectively. Fig. 5a depicts a cross sectional bright-field (BF) image of the unaffected coating and scale on top (from left to right hand side). Here, the highly fine-grained growth morphology of the unaffected WB_{2-z} coating is conceivable as no features are visible. In contrast, the thermally grown scale exhibits a granular-like, dense structure that is coarser towards the outermost regions. The Pt layer on top was deposited during FIB preparation of the TEM lamella. High resolution images – see Fig. 5b and c – show a fine-grained and dense oxide morphology near the coating-oxide interface (see Fig. 5b), whereas at the outermost region relatively large (about ~ 100 nm) crystallites are formed (see Fig. 5c). This morphological change of the oxide with increasing thickness is possibly related to the changing growth mode of the forming WO_3 crystals, whereby the outermost regions undergo the longest oxidation time and consequently ongoing diffusion (having also the strongest oxygen supply). However, this area is also slightly porous at some positions. SAED also emphasizes the formation of a WO_3 crystals, see indexed pattern in Fig. 5d.

Fig. 6a shows a Scanning TEM – high angle annular dark-field (STEM-HAADF) image of the oxidized $W_{0.66}Ta_{0.34}B_{2-z}$ thin film. The formed oxide scale exhibits fine crystallites embedded in an amorphous matrix, also showing lateral cracks near the coating-oxide interface (see BF image in Fig. 6b). Here, the crack formation is related to the growth of WO_{3-x} and Ta_2O_{5-x}, which possess different thermal expansion coefficients (WO_3 ~ $12 \cdot 10^{-6}$ C^{-1}, Ta_2O_5 ~ $4 \cdot 10^{-6}$ C^{-1} [34,35]) also with respect to the unaffected $W_{0.66}Ta_{0.34}B_{2-z}$ coating material. The difference in CTE needs also to be seen with respect to the unintended

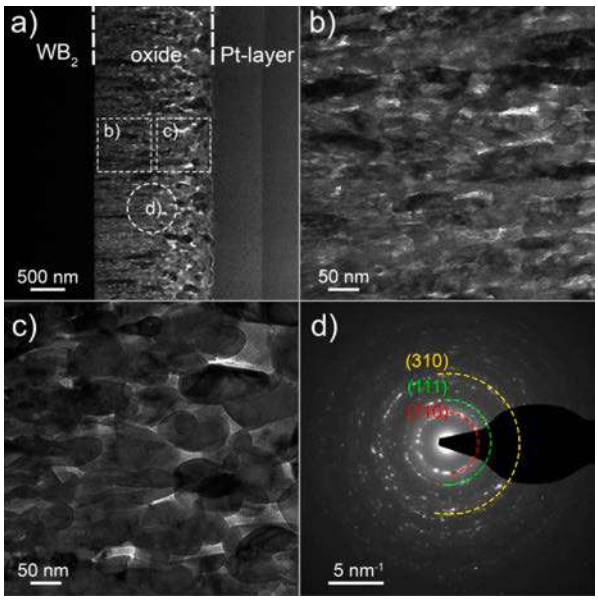

Fig. 5. Detailed TEM investigations of an oxidized WB_{2-z} coating after oxidation at 700 °C for a duration of 10 min. Section (a) shows a bright-field (BF) TEM cross section of the oxidized coating, pointing out the areas for the HR images displayed in (b) and (c) and the recorded SAED shown in (d). The indicated ring patterns correspond to a WO_3 crystal.

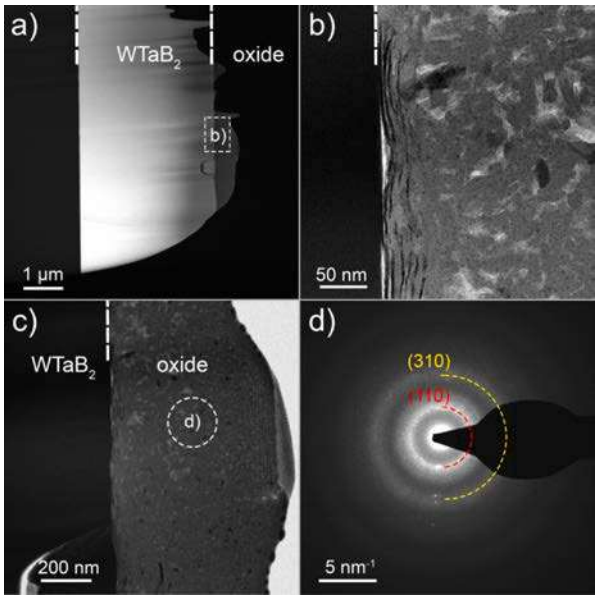

Fig. 6. Detailed TEM investigations of an oxidized $W_{0.66}Ta_{0.34}B_{2-z}$ coating after oxidation at 700 °C for a duration of 10 min. Section (a) shows a STEM-HAADF cross section of the oxidized coating, pointing out the area for the BF image displayed in (b). Another BF cross section is depicted in (c) indicating the recorded SAED shown in (d).

variation of the chemical composition originating from the co-sputtering process – see APT investigations in Fig. 2 – and hence suggesting for a partly layered oxide scale and related crack formation. Compared to the oxide grown on pure WB_{2-z}, the crystallite size of the oxide that originates from $W_{0.66}Ta_{0.34}B_{2-z}$ stays rather constant over the entire scale (BF micro-graph, Fig. 6c). The amorphous oxide scale is also highlighted by the SAED pattern, depicted in Fig. 6d. However, WO_3 based crystallites can be indicated considering the very broad ring-shaped patterns as depicted in Fig. 6d. (Please place Figure 6 here)

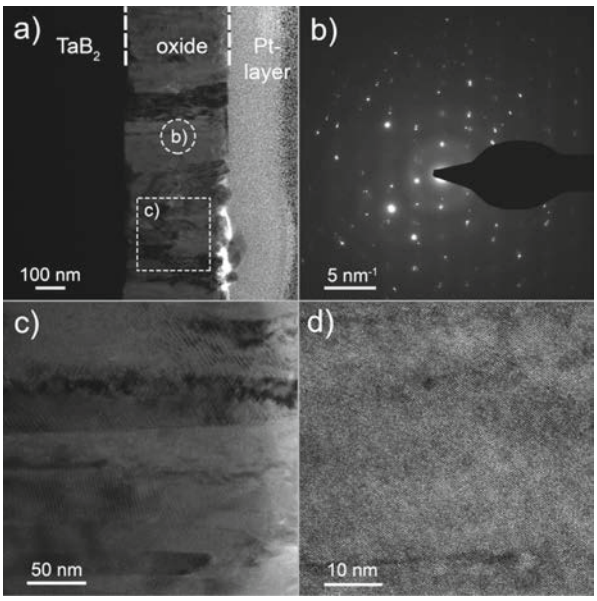

Fig. 7. TEM micrographs of an oxidized TaB_{2-z} coating after oxidation at 700 °C for a duration of 10 min. Section (a) shows a BF TEM cross section of the oxidized coating, pointing out the areas for the recorded SAED displayed in (b) and the detailed BF image of the oxide scale shown in (c). An even more detailed view (high magnified-TEM) on the oxide is depicted in (d).

Fig. 7a displays a BF cross section of the oxidized TaB_{2-z} coating, pointing out the areas for recorded SAED (Fig. 7b) and higher resolution BF image (Fig. 7c) of the formed oxide scale. Here, the very dense, columnar growth morphology with grain sizes up to 100 nm is very remarkable. Unfortunately, it was not possible to allocate the SAED pattern, which can be seen in Fig. 7b, to one distinct crystal structure. As the oxide layer on top of the TaB_2 film is composed of various grains revealing different crystal orientations and potentially different crystal structures, a very diffuse diffraction pattern appears. Nevertheless, Ta_2O_5 (in both versions orthorhombic [SG 25, Pmm2] as well as trigonal [SG 146, R3]) and $TaBO_4$ (orthorhombic [SG 141, $I4_1/amd$]) crystal structures revealed the best and most reliable matches in terms of the depicted SAED pattern. (Please place Figure 7 here)

3.5. Oxide scale constitution

To get a deeper insight into the oxide scale constitution, EDS investigations of oxidized WB_{2-z}, $W_{0.66}Ta_{0.34}B_{2-z}$, and TaB_{2-z} coatings were performed during TEM – again after oxidizing at 700 °C for 10 min. In Fig. 8 the chemical composition is plotted as a function of the distance, which is highlighted in the STEM cross sections next to the EDS plots. A clear distinction between the oxide scale and the unaffected diboride coatings is possible for all three compositions. The EDS line scan in Fig. 8a reveals a W to O ratio of around 1–3, which indicates the occurrence of a WO_3 based scale – confirming the SAED results in Fig. 5d. However, also small amounts of boron can be detected, but being not dominant for the scale constitution and related to residuals during a volatile boron-oxide formation. Increasing the Ta content within the film also lead to a change in the scale constitution, as suggested by the line scan presented in Fig. 8b. The chemical composition depicted in Fig. 8b suggests for a highly oxygen rich scale, but still containing a certain amount of B. This is in good relation with the structural analysis of the scale presented in

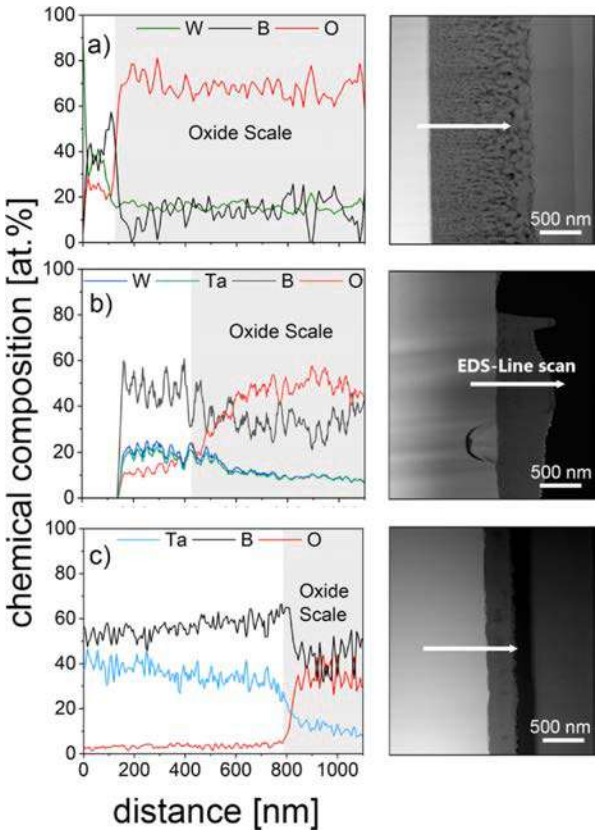

Fig. 8. EDS line scan of WB_{2-z} (a), $W_{0.66}Ta_{0.34}B_{2-z}$ (b) and TaB_{2-z} (c) thin films after oxidation with 700 °C for 10 min. The corresponding STEM micrographs on the right-hand side, indicate location and distance (white arrow – the tail refers to zero distance) of the performed EDS measurements. The uncertainty of quantifying light elements (like B and O) in EDS measurements can be in the range of 5–10%.

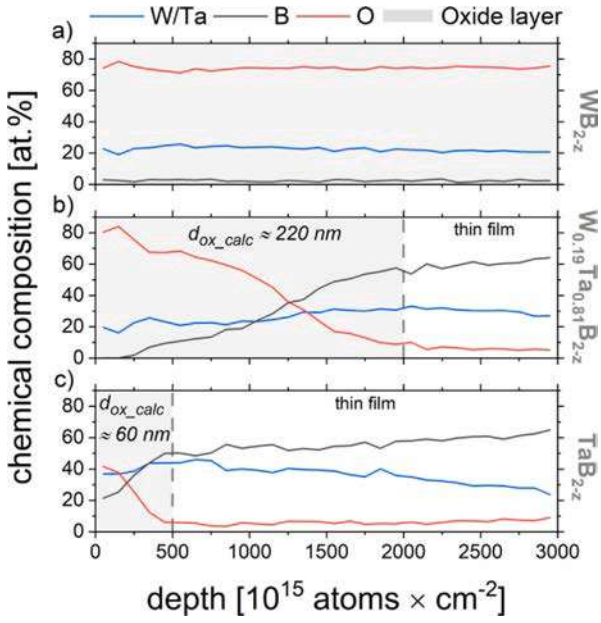

Fig. 9. Chemical composition of the oxide layers of WB_{2-z} (a), $W_{0.19}Ta_{0.81}B_{2-z}$ (b), and TaB_{2-z} (c) thin films after oxidation at 600 °C for 100 min, investigated by TOF-ERDA depth profiling. The gray area indicates the calculated oxide thickness by assuming a WO_3 structured oxide for WB_2, and mixed oxide phases for $W_{0.19}Ta_{0.81}B_{2-z}$ as well as TaB_{2-z}.

Fig. 6d indicating an amorphous state of the formed oxide scale, as boron oxide rich scales tend to be amorphous. Nevertheless, the metal (W,Ta) to O ratio is in the range of 1:4 emphasizing a change in the scale constitution. Additionally, the chemical composition of the oxidized TaB_{2-z} coating (see Fig. 8c) underlines this trend, that the presence of Ta lead to a decelerated (volatile) boron oxide formation. The chemical analysis suggests for mixed oxide structures such as Ta_2O_5 and $TaBO_4$ – being in correspondence with the structural analysis in Fig. 7b.

As it is very difficult to gain reliable values for boron (and partly oxygen) contents with EDS, the chemical composition of the formed oxide scales, after 100 h at 600 °C, was also investigated by TOF-ERDA. Due to resolution limits regarding the distinction of heavy W and Ta atoms, the elemental amount of tungsten and tantalum is summarized in a single dataset (blue lines). Fig. 9a reveals a boron depleted oxide layer (at least ~200 nm from the top of the oxide) on top of the WB_2 coating, indicating a clear volatile character of boron oxides during oxidation tests. However, the gradually increasing B contents for the Ta rich coatings as $W_{0.19}Ta_{0.81}B_{2-z}$ or pure TaB_{2-z} suggest a change from the volatile behavior to a more partly-viscous (glassy) character of the boron oxide through Ta. A similar tendency was also observed in the EDS line scans conducted during TEM analysis – see Fig. 8. TOF-ERDA provides information about the number of recoiled atoms per area, which were hit by impinging heavy ions, represented by the depth value plotted on the abscissa in Fig. 9. Therefore, the theoretical layer thickness can be calculated by means of the density and the molar weight of the containing elements. For the measured oxides on TaB_{2-z} coatings, the interface between oxide layer and coating was suggested to be located at around 500×10^{15} atoms/cm^2, where no more oxygen could be detected (see Fig. 9c). The atomic density of the oxide (assuming a mean value of 8.4 g cm^{-3} considering orthorhombic and trigonal Ta_2O_5 as well as orthorhombic $TaBO_4$) leads to a calculated layer thickness (d_{ox_calc}) of ~60 nm. Of course, the calculations do not consider boron oxide-based structures which are present to small quantities (as seen in the EDS linescans and ERDA profiles). As SEM investigations revealed an oxide thickness of ~100 nm after oxidation at 600 °C and 100 min, a slightly under-dense (~60% density) oxide layer or a gradually variety/mixed oxide (leading to deviating densities) on TaB_{2-z} films is presumed. In Fig. 9b the calculated oxide thickness for $W_{0.19}Ta_{0.81}B_{2-z}$ was ~220 nm leading to a density of ~40% - relative to a measured oxide thickness of around 600 nm. Here we applied a weighted atomic density for the oxide, in correspondence to the line scan presented in Fig. 8b, of about 8.2 g cm^{-3}. Unfortunately, the penetration depth of ERDA was too low for detecting the oxide/coating interface of WB_{2-z} (see Fig. 9a). Hence, no thickness and oxide density could be calculated for pure WB_{2-z}. Nevertheless, an even lower oxide density compared to Ta-alloyed coatings is suggested by analyzing the TEM images represented in the foregoing Figures. These results lead to the assumption that the addition of Ta not only decreases the oxide scale growth kinetics but also increases the scale density.

4. Conclusion

To investigate the oxidation resistance of $W_{1-x}Ta_xB_{2-z}$ coatings, compositions in the full range from WB_{2-z}, $W_{0.85}Ta_{0.15}B_{2-z}$, $W_{0.66}Ta_{0.34}B_{2-z}$, $W_{0.42}Ta_{0.58}B_{2-z}$, $W_{0.19}Ta_{0.81}B_{2-z}$, to TaB_{2-z} were deposited by DC magnetron co-sputtering utilizing W_2B_5 and TaB_2 targets, respectively. ICP-OES as well as TOF-ERDA exhibit similar tendency of decreasing B contents with increasing amounts of tantalum, indicating that the phase formation of α-structured

$W_{1-x}Ta_xB_{2-z}$ films at high Ta fractions is limited and directed towards dual phase structures (α-TaB_{2-z} and o-TaB). As highlighted by atom probe tomography, a layered structure composed of Ta-rich and W-rich zones is occurring at the nanoscale (in the range of 5–10 nm) – but it is assumed to be an artifact of co-sputtering.

After oxidation tests in ambient air at 500, 600, 700 °C for 1, 10, 100 and 1000 min, respectively, the formed oxide layers were analyzed by SEM, TEM, and TOF-ERDA. The investigations showed a decrease in oxide layer thickness with increasing Ta content for all temperature settings. At T_{ox} = 600 °C and t_{ox} = 100 min the oxide scale thickness decreases steadily from 2.2 µm to 0.1 µm from WB_{2-z} to TaB_{2-z}. A detailed evaluation of the oxidation kinetics revealed a paralinear scale growth for W-rich coatings becoming more linear but retarded with increasing Ta. The corresponding rate constants decelerate from $k_p^* = 6.3 \cdot 10^{-4}$ µm²/s for.

WB_{2-z} to $k_l = 2.6 \cdot 10^{-5}$ µm/s (linear oxidation growth mode) for TaB_{2-z}. After 100 min at T_{ox} = 700 °C all coatings exhibit extensive scaling suggesting imminent break-through oxidation, also underlined by the presence of lateral cracks. SAED investigations exhibited a WO_3 based oxide layer for WB_{2-z} and mixed oxide scales (e.g. Ta_2O_5 as well as $TaBO_4$) for TaB_{2-z} films, also underlined by TEM-EDS line scans. Furthermore, TOF-ERDA measurements showed an increased amount of boron within the oxide scales for coatings with rising Ta content, suggesting for a decelerated formation of a volatile boron oxides.

In summary, the addition of Ta to WB_{2-z} based coatings retards the oxide scale kinetics through the formation of denser, less volatile, and adherent scales, thus being a key factor for the enhanced oxidation resistance. An optimum composition of $W_{1-x}Ta_xB_{2-z}$ based coatings would be in the range of x = 0.2–0.3, combining enhanced fracture toughness (≥3.0 MPa√m) as well as super hardness (≥40 GPa) next to a decent oxidation resistance.

CRediT authorship contribution statement

C. Fuger: Conceptualization, Software, Investigation, Writing - original draft. **B. Schwartz:** Investigation. **T. Wojcik:** Investigation. **V. Moraes:** Investigation. **M. Weiss:** Investigation, Writing - review & editing. **A. Limbeck:** Investigation. **C.A. Macauley:** Investigation, Writing - review & editing. **O. Hunold:** Writing - review & editing. **P. Polcik:** Writing - review & editing. **D. Primetzhofer:** Investigation, Writing - review & editing. **P. Felfer:** Investigation, Writing - review & editing. **P.H. Mayrhofer:** Writing - review & editing. **H. Riedl:** Supervision, Conceptualization, Writing - review & editing, Project administration.

Declaration of Competing Interest

The authors declare that they have no known competing financial interests or personal relationships that could have appeared to influence the work reported in this paper.

Acknowledgements

The authors greatly acknowledge the financial support of Plansee Composite Materials GmbH, Oerlikon Balzers Surface Solutions AG and the Christian Doppler Gesellschaft within the framework of the Christian Doppler Laboratory for Surface Engineering of high-performance Components. SEM and TEM investigations were carried out using facilities of the USTEM center of TU Wien, Austria. CM and PF acknowledge financial support by the Bavarian Ministry of Economic Affairs and Media, Energy and Technology for the joint projects in the framework of the Helmholtz Institute Erlangen-Nürnberg for Renewable Energy (IEK-11) of Forschungszentrum Jülich. CAM and PF would also like to acknowledge funding by the Deutsche Forschungsgemeinschaft (DFG) via the Cluster of Excellence 'Engineering of Advanced Materials' (project EXC 315). Support by VR-RFI (contracts #821-012-5144 and #2017-00646_9) and the Swedish Foundation for Strategic Research (SSF, contract RIF14-0053) supporting accelerator operation is gratefully acknowledged.

Appendix

See Appendix Fig. A1.

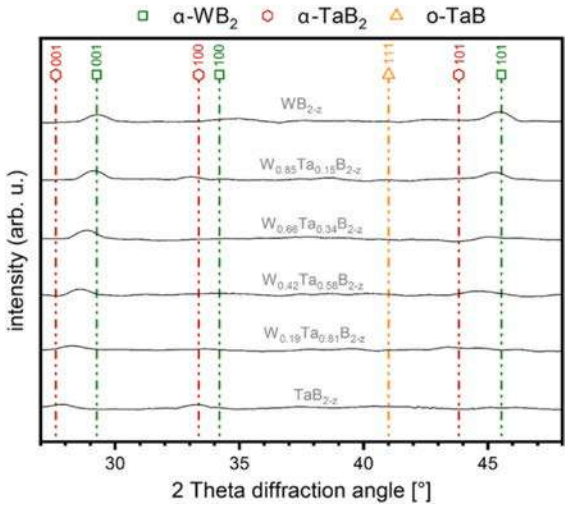

Fig. A 1. Structural evolution of $W_{1-x}Ta_xB_{2-z}$ thin films obtained by XRD analysis, realized by a Philips XPERT diffractometer in Bragg-Brentano configuration equipped with a Cu-Kα (λ = 1.54 Å) radiation source. The green, red and yellow dashed vertical lines are indicating the α-WB_2, α-TaB_2 and o-TaB phase, respectively [12].

References

[1] I. Petrov, L. Hultman, U. Helmersson, J.-E. Sundgren, J.E. Greene, Microstructure modification of TiN by ion bombardment during reactive sputter deposition, Thin Solid Films 169 (1989) 299–314, https://doi.org/10.1016/0040-6090(89)90713-X.
[2] O. Knotek, F. Löffler, H.J. Scholl, C. Barimani, The multisource arc process for depositing ternary Cr- and Ti-based coatings, Surf. Coatings Technol. 68–69 (1994) 309–313, https://doi.org/10.1016/0257-8972(94)90178-3.
[3] W. Münz, Titanium aluminum nitride films: a new alternative to TiN coatings, J. Vac. Sci. Technol. A 4 (1986) 2717–2725, https://doi.org/10.1116/1.573713.
[4] C. Mitterer, Borides in thin film technology, J. Solid State Chem. 133 (1997) 279–291, https://doi.org/10.1006/JSSC.1997.7456.
[5] H. Euchner, P.H. Mayrhofer, Designing thin film materials-ternary borides from first principles, Thin Solid Films 583 (2015) 46–49, https://doi.org/10.1016/j.tsf.2015.03.035.
[6] J. Nagamatsu, N. Nakagawa, T. Muranaka, Y. Zenitani, J. Akimitsu, Superconductivity at 39 K in magnesium diboride, Nature 410 (2001) 63–64, https://doi.org/10.1038/35065039.
[7] K. Balasubramanian, S.V. Khare, D. Gall, Valence electron concentration as an indicator for mechanical properties in rocksalt structure nitrides, carbides and carbonitrides, Acta Mater. 152 (2018) 175–185, https://doi.org/10.1016/J.ACTAMAT.2018.04.033.
[8] T. Chihi, M. Reffas, M. Fatmi, A. Bouhemadou, B. Ghebouli, M.A. Ghebouli, Brittle to ductile transition dependence upon the transition pressure of MB_2 (M=Ti, Zr, Hf, V, Nb, Ta, Cr, Mo, W) compounds, Chin. J. Phys. 53 (2015) 100801–100802, https://doi.org/10.6122/CJP.20150703.
[9] J. Karch, R. Birringer, H. Gleiter, Ceramics ductile at low temperature (1987) 6–8.
[10] A.L. Ivanovskii, Mechanical and electronic properties of diborides of transition 3d–5d metals from first principles: toward search of novel ultra-incompressible and superhard materials, Prog. Mater. Sci. 57 (2012) 184–228, https://doi.org/10.1016/J.PMATSCI.2011.05.004.
[11] V. Moraes, H. Riedl, C. Fuger, P. Polcik, H. Bolvardi, D. Holec, P.H. Mayrhofer, Ab initio inspired design of ternary boride thin films, Sci. Rep. 8 (2018) 9288, https://doi.org/10.1038/s41598-018-27426-w.
[12] C. Fuger, V. Moraes, R. Hahn, H. Bolvardi, P. Polcik, H. Riedl, P.H. Mayrhofer, Influence of tantalum on phase stability and mechanical properties of WB2, MRS Commun. 9 (2019) 375–380, https://doi.org/10.1557/mrc.2019.5.
[13] B. Bakhit, D.L.J. Engberg, J. Lu, J. Rosen, H. Högberg, L. Hultman, I. Petrov, J.E. Greene, G. Greczynski, Strategy for simultaneously increasing both hardness and toughness in ZrB_2 -rich $Zr_{1-x}Ta_xB_y$ thin films, J. Vac. Sci. Technol. A 37 (2019) 031506, , https://doi.org/10.1116/1.5093170.
[14] T. Glechner, R. Hahn, T. Wojcik, D. Holec, S. Kolozsvári, H. Zaid, S. Kodambaka, P.H. Mayrhofer, H. Riedl, Assessment of ductile character in superhard Ta-C-N thin films, Acta Mater. 179 (2019) 17–25, https://doi.org/10.1016/J.ACTAMAT.2019.08.015.
[15] Y.M. Liu, R.Q. Han, F. Liu, Z.L. Pei, C. Sun, Sputtering gas pressure and target power dependence on the microstructure and properties of DC-magnetron sputtered AlB2-type WB2 films, J. Alloys Compd. 703 (2017) 188–197, https://doi.org/10.1016/J.JALLCOM.2017.01.337.
[16] Y. Liu, W. Shi, L. Tian, T. Li, C. Wang, F. Liu, Z. Pei, D. Fan, Influence of modulation period on structure and mechanical properties of WB2/CrN films deposited by direct-current magnetron sputtering, J. Alloys Compd. 788 (2019) 729–738, https://doi.org/10.1016/J.JALLCOM.2019.02.188.
[17] L.E. Pangilinan, C.L. Turner, G. Akopov, M. Anderson, R. Mohammadi, R.B. Kaner, Superhard tungsten diboride-based solid solutions, Inorg. Chem. 57 (2018) 15305–15313, https://doi.org/10.1021/acs.inorgchem.8b02620.
[18] V. Moraes, C. Fuger, V. Paneta, D. Primetzhofer, P. Polcik, H. Bolvardi, M. Arndt, H. Riedl, P.H. Mayrhofer, Substoichiometry and tantalum dependent thermal stability of α-structured W-Ta-B thin films, Sci. Mater. 155 (2018) 5–10, https://doi.org/10.1016/J.SCRIPTAMAT.2018.06.005.
[19] L. Zauner, P. Ertelthaler, T. Wojcik, H. Bolvardi, S. Kolozsvári, P.H. Mayrhofer, H. Riedl, Reactive HiPIMS deposition of Ti-Al-N: Influence of the deposition parameters on the cubic to hexagonal phase transition, Surf. Coatings Technol. 382 (2020) 125007, , https://doi.org/10.1016/J.SURFCOAT.2019.125007.
[20] A. Cakara, M. Bonta, H. Riedl, P.H. Mayrhofer, A. Limbeck, Development of a multi-variate calibration approach for quantitative analysis of oxidation resistant Mo–Si–B coatings using laser ablation inductively coupled plasma mass spectrometry, Spectrochim. Acta Part B At. Spectrosc. 120 (2016) 57–62, https://doi.org/10.1016/J.SAB.2016.04.004.
[21] H. Riedl, A. Vieweg, A. Limbeck, J. Kalaš, M. Arndt, P. Polcik, H. Euchner, M. Bartosik, P.H. Mayrhofer, Thermal stability and mechanical properties of boron enhanced Mo–Si coatings, Surf. Coatings Technol. 280 (2015) 282–290, https://doi.org/10.1016/J.SURFCOAT.2015.09.015.
[22] M. Bonta, J. Frank, S. Taibl, J. Fleig, A. Limbeck, Online-LASIL: laser ablation of solid samples in liquid with online-coupled ICP-OES detection for direct determination of the stoichiometry of complex metal oxide thin layers, Anal. Chim. Acta 1000 (2018) 93–99, https://doi.org/10.1016/J.ACA.2017.10.025.
[23] E. Aschauer, S. Sackl, T. Schachinger, T. Wojcik, H. Bolvardi, M. Arndt, P. Polcik, H. Riedl, P.H. Mayrhofer, Nano-structural investigation of Ti-Al-N/Mo-Si-B multilayer coatings: a comparative study by APT and HR-TEM, Vacuum 157 (2018) 173–179, https://doi.org/10.1016/J.VACUUM.2018.08.037.
[24] P. Ström, P. Petersson, M. Rubel, G. Possnert, A combined segmented anode gas ionization chamber and time-of-flight detector for heavy ion elastic recoil detection analysis, Rev. Sci. Instrum. 87 (2016) 103303, , https://doi.org/10.1063/1.4963709.
[25] M.A. Arvizu, R.-T. Wen, D. Primetzhofer, J.E. Klemberg-Sapieha, L. Martinu, G.A. Niklasson, C.G. Granqvist, Galvanostatic ion detrapping rejuvenates oxide thin films, ACS Appl. Mater. Interfaces 7 (2015) 26387–26390, https://doi.org/10.1021/acsami.5b09430.
[26] Y. Zhang, H.J. Whitlow, T. Winzell, I.F. Bubb, T. Sajavaara, K. Arstila, J. Keinonen, Detection efficiency of time-of-flight energy elastic recoil detection analysis systems, Nucl. Instrum. Methods Phys. Res. Sect. B Beam Interact. Mater. Atoms 149 (1999) 477–489, https://doi.org/10.1016/S0168-583X(98)00963-X.
[27] M.S. Janson, CONTES instruction manual (2004).
[28] E. Aschauer, H. Riedl, C.M. Koller, H. Bolvardi, M. Arndt, P. Polcik, P.H. Mayrhofer, Adhesive wear formation on PVD coated tools applied in hot forming of Al-Si coated steel sheets, Wear 430–431 (2019) 309–316, https://doi.org/10.1016/J.WEAR.2019.05.019.
[29] M. Thuvander, G. Östberg, M. Ahlgren, L.K.L. Falk, Atom probe tomography of a Ti–Si–Al–C–N coating grown on a cemented carbide substrate, Ultramicroscopy 159 (2015) 308–313, https://doi.org/10.1016/j.ultramic.2015.04.008.
[30] M. Hans, J.M. Schneider, On the chemical composition of TiAlN thin films - comparison of ion beam analysis and laser-assisted atom probe tomography with varying laser pulse energy, Thin Solid Films 688 (2019) 137251, , https://doi.org/10.1016/j.tsf.2019.04.026.
[31] H. Riedl, C.M. Koller, F. Munnik, H. Hutter, F. Mendez Martin, R. Rachbauer, S. Kolozsvári, M. Bartosik, P.H. Mayrhofer, Influence of oxygen impurities on growth morphology, structure and mechanical properties of Ti–Al–N thin films, Thin Solid Films 603 (2016) 39–49, https://doi.org/10.1016/j.tsf.2016.01.039.
[32] O. Kubaschewski, B.E. Hopkins, Oxidation mechanisms of niobium, tantalum, molybdenum and tungsten, J. Less Common Met. 2 (1960) 172–180, https://doi.org/10.1016/0022-5088(60)90012-6.
[33] R. Hollerweger, H. Riedl, J. Paulitsch, M. Arndt, R. Rachbauer, P. Polcik, S. Primig, P.H. Mayrhofer, Origin of high temperature oxidation resistance of Ti–Al–Ta–N coatings, Surf. Coatings Technol. 257 (2014) 78–86, https://doi.org/10.1016/J.SURFCOAT.2014.02.067.
[34] T. Tokunaga, T. Kawamoto, K. Tanaka, N. Nakamura, Y. Hayashi, K. Sasaki, K. Kuroda, T. Yamamoto, Growth and structure analysis of tungsten oxide nanorods using environmental TEM, Nanoscale Res. Lett. 7 (2012) 85, https://doi.org/10.1186/1556-276X-7-85.
[35] M. Moldovan, C.M. Weyant, D.L. Johnson, K.T. Faber, Tantalum oxide coatings as candidate environmental barriers, J. Therm. Spray Technol. 13 (2004) 51–56, https://doi.org/10.1007/s11666-004-0049-z.

Publication IV

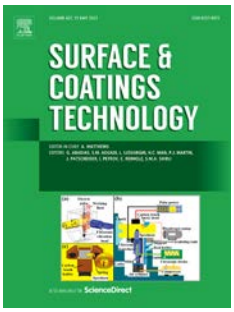

Revisiting the origins of super-hardness in TiB_{2+z} thin films – Impact of growth conditions and anisotropy

C. Fuger, R. Hahn, A. Hirle, P. Kutrowatz, M. Weiss, A. Limbeck, O. Hunold, P. Polcik, and H. Riedl

under review at Surface and Coatings Technology since 15.04.2022

Surface & Coatings Technology

Revisiting the origins of super-hardness in TiB2+z thin films – Impact of growth conditions and anisotropy

--Manuscript Draft--

Manuscript Number:	SURFCOAT-D-22-01271
Article Type:	Full Length Article
Keywords:	TiB2; Stoichiometry; Anisotropy; Super-hardness; Fracture toughness
Corresponding Author:	Christoph Fuger Vienna, AUSTRIA
First Author:	Christoph Fuger
Order of Authors:	Christoph Fuger
	R. Hahn
	A. Hirle
	P. Kutrowatz
	M. Weiss
	A. Limbeck
	O. Hunold
	P. Polcik
	H. Riedl
Abstract:	Hexagonal transition metal diborides embody promising material systems for the purpose of protective thin films. Here, we focus on DC magnetron sputtered TiB2+z coating materials, comprehensively revisiting the impact of the stoichiometry on the structure-mechanical properties, from nearly stoichiometric TiB2.07 (B: 67 at. %) up to super-stoichiometric TiB4.42 (B: 82 at. %). Structural analysis confirmed the apparent correlation between the deposition pressure and the preferred 0001 texture, which is essential to gain super-hardness (> 40 GPa). In contrast, H decreases for more than 10 GPa for 10-11 and 1000 oriented thin films, underlining the pronounced anisotropy of TiB2+z. No predominant effect of a B rich tissue phase is observed during the broad stoichiometry variation. A surplus of excess B decreases the coherently diffracting domain sizes, indicating smaller grain sizes, leading to a drop in H of ~5 GPa (B/Ti ratios > 2.5). Micro-cantilever bending experiments proved a declining KIC from 3.02 ± 0.13 MPa√m for TiB2.43 to 2.51 ± 0.14 MPa√m for TiB4.42 to be grain size dependent.
Suggested Reviewers:	Ivan Petrov, Prof. Dr. petrov@illinois.edu
	Christian Mitterer, Prof. Dr. Christian.Mitterer@unileoben.ac.at
	Petr Vasina, Prof. Dr. vasina@physics.muni.cz
	Hong Sun, Prof. Dr. hsun@sjtu.edu.cn
	Jimmy Thörnberg, Dr. jimmy.thornberg@liu.se

Publication V

Tissue phase affected fracture toughness of nano-columnar TiB_{2+z} thin films

C. Fuger, R. Hahn, A. Hirle, T. Wojcik, P. Kutrowatz, L. Zauner, F. Bohrn, M. Weiss, A. Limbeck, O. Hunold, P. Polcik, and H. Riedl

in final preparation for Nano Letters